Graduate School Form 30
Updated 1/15/2015

PURDUE UNIVERSITY
GRADUATE SCHOOL
Thesis/Dissertation Acceptance

This is to certify that the thesis/dissertation prepared

By WEN ZHU

Entitled
PROBING THE MECHANISM OF BACILLUS SUBTILIS OXALATE DECARBOXYLASE

For the degree of Doctor of Philosophy

Is approved by the final examining committee:

Nigel Richards
Co-chair

Lei Li
Co-chair

Kavita Shah

Andrew Mesecar

To the best of my knowledge and as understood by the student in the Thesis/Dissertation Agreement, Publication Delay, and Certification Disclaimer (Graduate School Form 32), this thesis/dissertation adheres to the provisions of Purdue University's "Policy of Integrity in Research" and the use of copyright material.

Approved by Major Professor(s): Nigel Richards / Lei Li

Approved by: Eric C. Long 12/1/2015
Head of the Departmental Graduate Program Date

PROBING THE MECHANISM OF *BACILLUS SUBTILIS* OXALATE DECARBOXYLASE

A Dissertation
Submitted to the Faculty
of
Purdue University
by
Wen Zhu

In Partial Fulfillment of the
Requirements for the Degree
of
Doctor of Philosophy

December 2015
Purdue University
West Lafayette, Indiana

To my parents.

ACKNOWLEDGMENTS

There are many people I would like to acknowledge for their support and help to make this thesis possible. I would like to express my appreciation to my advisor, Dr. Nigel G. J. Richards, who has been absolutely supportive for my study and research ever since I joined the group.

Thanks go to my past and present doctoral dissertation committee members, including Dr. Steven D. Bruner, Dr. David N. Silverman, Dr. George Christou and Dr. Rebecca A. Butcher from the University of Florida, Dr. Kavita Shah and Dr. Andrew Mesecar from Purdue University, and Dr. Lei Li from Indiana University-Purdue University Indianapolis.

I owe a great debt of gratitude to all the collaborators of this project. Dr. Wallace. W. Cleland and Dr. Laurie A. Renhardt in University of Wisconsin, Madison; Dr. R. David Britt and Dr. Jarett Wilcoxen in the University of California, Davis; Dr. Karen Allen and Linsey M. Easthon in Boston University; Dr. Chingkuang Tu, Dr. Alexander Angerhofer and Umar T. Twahir in the University of Florida. In addition, thanks go to Dr. Lars H. Boettger and Dr. Edward I. Solomon in Standford University; Dr. Brian G. Fox and Dr. Michael Mbughuni in the University of Wisconsin, Madison, for their support and inspiring discussion as well. I especially would like to thank Dr. Wallace W. Cleland for hospitality during my stay in Madison.

I am grateful to the colleagues in Richards research group, Dr. Malea Kneen, Dr. Yongmo Ahn, Dr. Whitney F. Kellett and Dr. Mario. E. G. Moral for the invaluable skills I learned at the beginning of my research and the useful discussion during my study. I also thank my friend Megan Rogers for proofreading my thesis.

Finally, I want to thank my parents, grandparents and my cousin Ke for their unconditional support and love.

TABLE OF CONTENTS

Page

LIST OF TABLES

LIST OF FIGURES

ABBREVIATIONS

ABTS	2,2-azinobis-(3-ethylbenzothiazoline-6-sulfonic acid
AENS	Alanine161-Glutamate162-Asparagine163-Serine164
B. subtilis, Bs	*Bacillus subtilis*
CD	Circular Dichroism
C. subvermispora, Cs	*Ceriporiopsis subvermispora*
DASN	Aspartate161-Alanine162-Serine163-Asparagine164
DDNS	Aspartate161-Aspartate162-Asparagine163-Serine164
DDSN	Aspartate161-Aspartate162-Serine163-Asparagine164
DESN	Aspartate161-Glutamate162-Serine163-Asparagine164
DFT	Density Functional Theory
DMPO	5,5-Dimethyl-1-pyrroline-N-oxide
DTPA	diethylene triamine pentaacetic acid
EPR	Electron Paramagnetic Resonances
E. coli	*Escherichia coli*
FDH	Formate Dehydrogenase
GC-MS	Gas Chromatography Mass Spectrometry
GLPs	Germin-like Proteins
HRP	Horseradish Peroxidase
H. vulgare, Hv	*Hordeum vulgare*
IE	Isotope Effect
IPTG	Isopropyl-β-D-1-thiogalactopyranoside
IRMS	Isotope Ratio Mass Spectrometry
KIEs	Kinetic Isotope Effects

MCD	Magnetic Cirular Dichroism
MD	Molecular Dynamics
MIMS	Membrane Inlet Mass Spectrometry
NAD^+	Nicotinamide Adenine Dinucleotide
NMR	Nuclear Magnetic Resonance
OXC	Oxalyl-CoA Decarboxylase
OxDC	Oxalate Decarboxylase
OxOx	Oxalate Oxidase
PBN	N-tertiary-butyl nitrone
PCR	Polymerase Chain Reaction
SANS	Serine161-Alanine162-Asparagine163-Serine164
SDNS	Serine161-Aspartate162-Asparagine163-Serine164
SDS-PAGE	Sodium Dodecyl Sulfate Polyacrylamide Gel Electrophoresis
TEMPO	2,2,6,6-tetramethylpiperidinyloxy, free radical
WT	Wild Type
zfs	zero-field splitting

ABSTRACT

Zhu, Wen PhD, Purdue University, December 2015. Probing the Mechanism of *Bacillus subtilis* Oxalate Decarboxylase. Major Professor: Nigel G. J Richards / Lei Li.

Oxalate decarboxylase (EC 4. 1. 1. 2 OxDC) from *Bacillus subtilis* is a manganese-dependent enzyme that catalyzes the cleavage of the chemically inactive C-C bond in oxalate to yield formate and carbon dioxide. A mechanism involving Mn(III) has been proposed for OxDC, however no clear spectroscopic evidence to support this mechanism has yet been obtained. In addition, a recent study has shown that N-terminal metal binding site loop variants of OxDC were able to catalyze the oxidation of oxalate to yield hydrogen peroxide and carbon dioxide, which makes OxDc function as another oxalate degradation protein in the cupin superfamily, oxalate oxidase (EC 1.2.3.4 OxOx). In this work, wild-type (WT) *Bacillus subtilis* OxDC and a series of variants with mutations on conserved residues were characterized to investigate the catalytic mechanism of OxDC. The application of membrane inlet mass spectrometry (MIMS), electronic paramagnetic resonance (EPR) spectroscopy and kinetic isotope effects (KIEs) provided information about the mechanism. The Mn(III) was identified and characterized under acidic conditions in the presence of dioxygen and oxalate. Mutations on the second shell residues in the N-terminal metal binding site affected the enzyme activity properties of the metal. In the N-terminal domain, the functional importance of the residues in the active site loop region, especially Glu162, was confirmed, and evidence for the previously proposed mechanism in which OxDC and the OxDC/OxOx chimeric variant share the initial steps has been found. In addition, the mono-dentate coordination of oxalate in the N-terminal metal binding site was confirmed by X-ray crystallography. A proteinase cleavable OxDC was constructed and characterized, revealing the interaction between the N-terminal and C-terminal domains.

1. INTRODUCTION

1.1 Oxalate and Oxalate Degrading Enzymes

Oxalate is consumed by humans in food and beverages. [1] The main sources of dietary oxalate are plants and plant products, principally seeds and leafy plants. [2] Oxalate is also produced endogenously in humans, arising from the breakdown of ascorbate and glyoxylate. [3] [4] It is removed from the body mainly by urinary excretion. [5] If accumulated in large amounts, oxalate can cause death in animals and humans. [6] In smaller quantities, it can cause a number of medical disorders [6] [7], including hyperoxaluria, [8] and renal failure [9]. Excessive urinary oxalate leads to deposition of calcium oxalate in the kidney, resulting in kidney stones. [10] According to data reported in 2012, 8.8 percent of the population in U.S. has had a kidney stone. [11] It is also a recurrent disease, and the reappearance of the stones is about 50% over 10 years in the absence of medical treatment and dietary restriction. [12]

Although humans do not encode any enzymes capable of degrading oxalate, oxalate degrading enzymes have been found in other plants [13], fungi, [14] [15] and bacteria [16].Three classes of enzymes have been identified that are able to degrade oxalate in nature: oxalate decarboxylase (OxDC) (EC 4.1.1.2), oxalate oxidase (OxOx) (EC 1.2.3.4) and oxalyl-CoA decarboxylase (OXC) (EC 4.1.1.8) (Fig. 1.1). [17] OXC requires thiamin pyrophosphate as a cofactor to yield a thioester to facilitate the C-C cleavage, [16] and will not be further discussed. OxDC and OxOx are both manganese-dependent enzymes that degrade oxalate in the presence of dioxygen to yield carbon dioxide and either formate or hydrogen peroxide, respectively. [17]

[redacted]

Figure 1.1. Chemical reactions catalyzed by the oxalate degrading enzymes.

The enzymatic degradation of oxalate is not only crucial for biological systems, it also has broad application in medicine and industry. [18] Studies in hyperoxaluria model mice have revealed that oral therapy using a cross-linked formulation of OxDC could reduce the amount of oxalate in urine, suggesting a potential approach for treatment of hyperoxaluria. [19] In the pulp and paper industry, degradation of excess oxalate in the bleaching filtrate is important for preventing the formation of calcium oxalate incrusts (scaling). [20] [21] Oxalate degrading enzymes also have applications as anti-fungal agents in agriculture. [22] [23] It has been found that the half-life for decarboxylation of oxalate at 25 °C without a catalyst is more than 3300 years due to the high free-energy barrier for cleavage of the C-C bond in oxalate. [24] [25] Investigating the mechanisms of these oxalate degrading enzymes provides new insights into the molecular processes and chemical strategies that Nature uses to catalyze cleavage of this chemically inert C-C bond.

1.1.1 Oxalate Decarboxylase

OxDC has been found in some wood-decaying fungi, such as white-rot fungus and brown-rot fungus. [14] [26] In fungi, the expression of OxDC can be non-induced [27], oxalate-induced [28] or acid-induced [29], depending on the species. The first, as well as the best characterized, bacterial OxDC was isolated from *Bacillus subtilis* 168. [30] *Bs*OxDC is encoded by *yvrk* (or *oxdC*). Expression of this gene under acidic stress is regulated by sigma factor, YvrI, and its co-regulators, YvrHa, and YvrL anti-sigma factor. [31] [32] The proposed physiological role of OxDC in *B. subtilis* is to control cellular pH since it is induced by acid but not by oxalate. [30]

1.1.2 Oxalate Oxidase

OxOx also uses oxalate as substrate and has a similar 3-D fold to OxDC. [33] However, OxOx oxidizes oxalate to carbon dioxide and hydrogen peroxide with the participation of dioxygen. [34] This enzyme has been identified and isolated in fungi [35] and higher plants. [36] OxOx isolated from fungi has been proposed to be involved in lignin-degradation. [35] In plants, as one of the germin-like proteins, the expression level of OxOx varies in different tissues, and it also varies in the different growth states. [37] Relatively large amounts of OxOx have been detected in young roots of some plants, such as barley [38], wheat [39], and maize [40], during their germination. OxOx is thought to be involved in defending the plant from fungal infection, [41] since the production of hydrogen peroxide is toxic to plant pathogens. [36] [42]

1.2 Previous Studies on OxDC

1.2.1 Structure of OxDC

*Bs*OxDC has been successfully overexpressed from the recombinant *yvrk* gene in *Eschericia coli.* [43] The heterologously expressed *Bs*OxDC is a hexamer, composed of a dimer of trimers [44](Fig. 1.2). The monomer of OxDC contains two cupin domains, which are structurally similar. In each monomer, metals in the N-terminal and C -terminal domains are coordinated by three histidine residues, a glutamate residue and water molecules (Fig. 1.3).

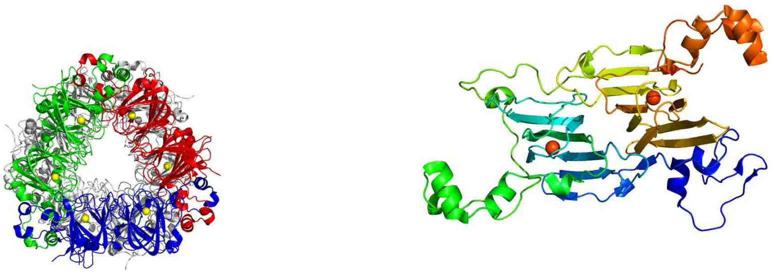

(a) OxDC hexamer (b) OxDC monomer

Figure 1.2. Crystal structure of *B. subtilis* OxDC (PDB 1UW8).

Although the residues coordinated directly with the metal are the same in the N-terminal and C-terminal sites, other residues in each binding site exhibit some variation (Fig. 1.3). For example, Trp132 in the second shell of the N-terminal site, which is able to form hydrogen bond with metal binding ligand Glu101, is replaced by a glutamine (Gln282) in the C-terminal site. A loop region that is able to adopt closed and open conformations appears to be present only in the N-terminal site. [45]

1.2.2 N-terminal Metal Binding Site is Catalytically Active

The prior studies suggest that the N-terminal metal binding site is the main active site for several reasons: 1) the open and closed conformations of the Ser161-Glu162-Asn163-Ser164 (SENS) loop near the N-terminal metal binding site creates a solvent accessible channel for substrate binding, [45] 2) formate binds to manganese in the N-terminal site in one of the crystal structures, [44] and 3) Glu162 on the N-terminal active site loop in the closed conformation is thought to function as a general acid/base in catalysis. [46] An atomistic molecular dynamics simulation (MD) simulated the

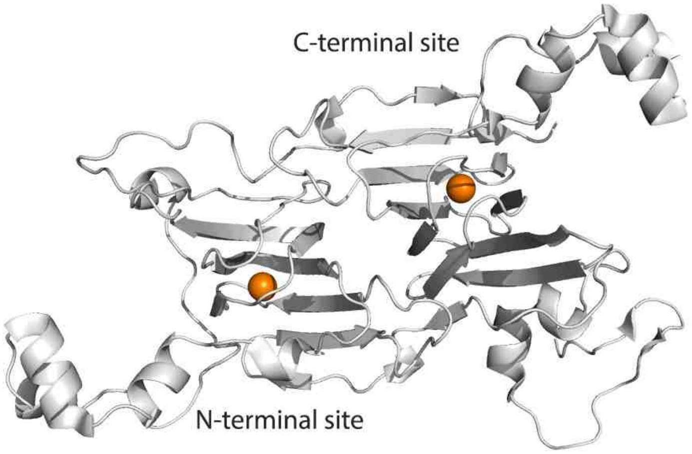

(a) OxDC Monomer

(b) OxDC N-terminal site

(c) OxDC C-terminal site

Figure 1.3. Conserved residues in N-terminal metal binding site and C-terminal metal binding site in OxDC. (PDB: 1UW8).

migration pathway of carbon dioxide, one of the decarboxylation products, from each of the two metal binding sites to the outside of the enzyme. [47] This simulation suggested that only the N-terminal metal binding site facilitates the release of carbon dioxide. Mutagenesis studies on the N-terminal site residues have also indicated that disruption of the conserved residues in the N-terminal site abolishes enzyme activity completely. [45] The catalytic mechanism proposed in the literature is therefore based on the N-terminal metal binding center. [46]

The functional role of the C-terminal metal binding site however is still unclear. Mutagenesis studies on the conserved C-terminal site residues suggests that impaired C-terminal metal binding site affects enzyme activity. [48] Currently, the C-terminal domain of OxDC is believed to have a structural function. [45] It is also possible that the C-terminal metal binding site is able to catalyze substrate decarboxylation, or participates in catalysis by interacting with the N-terminal site. [49]

1.2.3 Dioxygen is Necessary for Maintaining OxDC Activity

It has been found that OxDC is only active in the presence of dioxygen, although decarboxylation of oxalate is a disproportionation reaction. [43] The dioxygen-dependence study on *Aspergillus niger* OxDC showed that high partial pressures of dioxygen stimulate the rate of the decarboxylation of oxalate until reaching a point, beyond which, more dioxygen denatures the enzyme. The enzyme can only be denatured by O_2 in the presence of oxalate. [50] Removal of dioxygen from the reaction mixture decreases *Bs*OxDC activity by 6-fold, confirming that the presence of dioxygen is important for maintaining enzyme activity. [43] Failure to completely abolish OxDC activity under anaerobic conditions has been rationalized by the presence of a catalytic amount of tightly-bound dioxygen in the enzyme being able to partially facilitate the enzymatic reaction. [43]

It has been proposed that the role of dioxygen is to oxidize the catalytically important Mn(II) ion to Mn(III), which can then oxidize the bound substrate to form a intermediate. [51] A major problem with this idea, however, is the mismatched reduction potentials of dioxygen and Mn(III), [52] and a dearth of model Mn-containing inorganic complexes that can bind dioxygen. [53] An inhibition study using nitric oxide (NO) to mimic the binding of dioxygen to the active site of OxDC gave no significant effect on the electron paramagnetic resonance (EPR) spectrum of the manganese center, suggesting that dioxygen might not directly bind with manganese but rather in an oxygen binding pocket close to the metal. [54] Overall, the functional role of dioxygen in catalysis is poorly understood.

1.2.4 Manganese is Required for Catalysis

*Bs*OxDC is purified as a manganese-containing protein from its native source. [30] The heterologously expressed *Bs*OxDC is also a manganese-dependent protein. [55] The decarboxylase activity of OxDC is proportional to the manganese content, and other metals (e.g. cobalt, iron, and zinc) do not exhibit catalytic activity. [55] The geometry of bound Mn(II) is either penta-coordinate or octahedral depending on the experimental conditions used to obtain X-ray structure of WT OxDC. [44] [56]

Manganese has been found in many enzymes, such as the oxygen evolving complex of photosystem II [57], manganese superoxide dismutase [58], manganese-dependent catalase [59] and manganese-dependent peroxidase [60]. These manganese-dependent enzymes utilize higher oxidation states of manganese such as Mn(IV) and Mn(III) to catalyze reduction/oxidation reactions.

The reaction catalyzed by OxDC is a disproportionation reaction, however, lack of clear spectroscopic evidence for Mn(III) casts doubt on any proposed mechanism involving the formation of Mn(III).

1.2.5 N-terminal Loop is Crucial for OxDC Activity

Protein sequence alignments show that Glu162 in *Bs*OxDC is conserved across different species of bacterial OxDCs, although aspartate is also tolerated at this position in some species. In the closed loop conformation of WT OxDC, the oxygen on the carboxyl moiety of Glu162 is 2.8 Å away from the water that coordinates with Mn(II), and 4.6 Å away from the N-terminal manganese. [44] In the open loop conformation, Glu162 could form a hydrogen bond with the residue Asp297, which is located at the neighboring monomer in the hexameric structure. OxDC activity is almost abolished in the E162A and E162Q variant. [46]

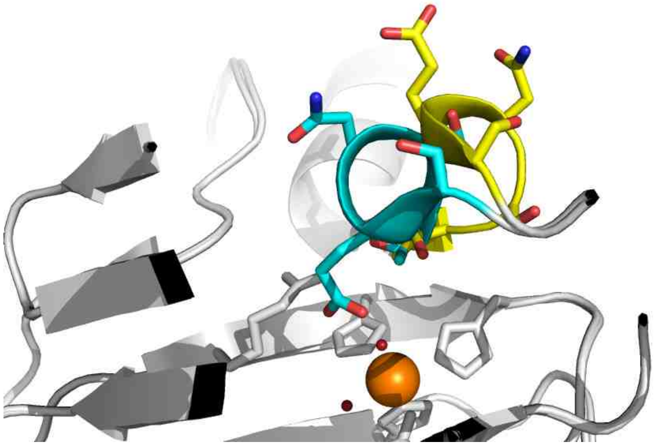

Figure 1.4. N-terminal loop region of OxDc have open (yellow) conformation and close (cyan) conformation.(PDB: 1UW8 and 1J58)

The N-terminal SENS loop in *Bs*OxDC is conserved in many putative OxDCs. This flexible loop was hypothesized to regulate substrate accessibility to the metal center from the outside of the enzyme (Fig. 1.4), and create an isolated environment for catalysis when it is closed. [46] More interestingly, when the residues in the OxDC SENS loop are mutated to the residues located on the corresponding region in OxOx, the enzyme becomes a OxDC/OxOx chimera that no longer exhibits OxDC activity, but becomes an oxidase. [56] Although WT OxDC exhibits 1% OxOx activity as a side reaction, [50] the switch of specific activity between the OxDC activity and the OxOx activity in the chimeric mutants was as high as 275,000-fold (the SENS161-4DSSN variant). [56] This finding was rationalized by assuming these two enzymes share the catalytic steps until decarboxylation, the presence of Glu162 in the loop region in OxDC then protonates the last common intermediate to give formate, while absence of Glu162 in the loop variants leads to production of hydrogen peroxide. [56]

1.2.6 Proposed Mechanism for OxDC

The pH profile of WT OxDC suggests that the mono-protonated oxalate is the true substrate of the enzyme. [61] Kinetic isotope effect (KIE) measurements indicated that an isotope sensitive step exists before the decarboxylation step, corresponding to the proposed proton-coupled electron transfer. [61] Moreover, calculation of the C-O bond order predicted an heterolytic cleavage of the C-C bond, suggesting the formation of a radical anion intermediate. This formyl radical intermediate has been observed by spin-trapping experiments using EPR spectroscopy. [62] Superoxide radical has also been detected under the catalytically optimum conditions for OxDC. [63] Combining this experimental evidence, a radical-based proton-coupled electron transfer mechanism can be proposed for OxDC (Fig. 1.5).

[redacted]

Figure 1.5. Proposed catalytic mechanism of OxDC.

However, several important pieces of evidence remain to be obtained. First, the existence of Mn(III) during the turnover has not been clear demonstrated. Second, it is unclear whether oxalate coordinates manganese in a monodentate or bidentate form. Third, the role of dioxygen in catalysis is ill-defined. The functional importance of conserved residues in the N-terminal site lalso needs to be further elucidated. In addition, this mechanism does not explain the importance of the C-terminal metal binding site for catalysis.

1.3 Previous Study on OxOx

1.3.1 OxOx in Higher Plants

The best characterized plant OxOx is present in barley (*Hordeum vulgare*) . [38] This Mn-containing protein is a mono cupin, which crystallizes as a homohexamer [64] (Fig. 1.6). *Hv*OxOx is an N-linked glycosylated protein. Attempts to overexpress several plant OxOx in *E.coli* gave insoluble or inactive protein, which was interpreted to be mis-folding of the protein in heterologous expression system. [65] Since a secretion signal peptide is present in putative plant OxOxs, [66] an incorrect folding location may underlie failure of *E. coli* expression systems. [65] The best-developed heterologous expression system for *Hv*OxOx uses *Pichia pastoris*, but the yield of active protein is very low, [34] and only 20% of the protein is correctly loaded with Mn.

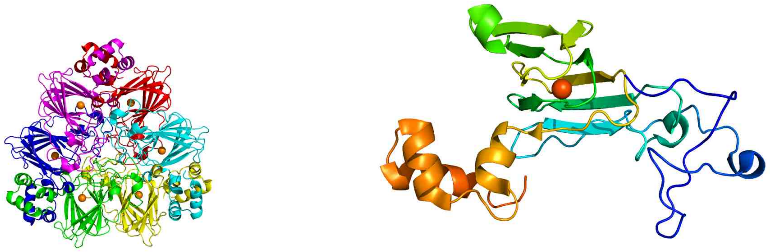

(a) *Hv*OxOx hexamer (b) *Hv*OxOx monomer

Figure 1.6. Crystal structure of *H. vulgare* OxOx (PDB 1FI2).

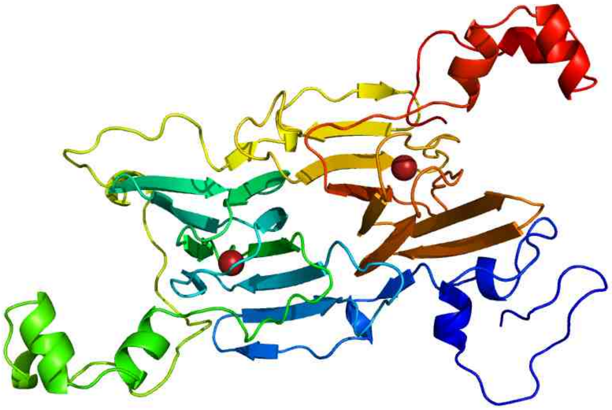

Figure 1.7. Homology model of *C. subvermispora*OxOx. Model was generated using Swiss-Model(http://swissmodel.expasy.org/).

1.3.2 OxOx in Fungus

OxOx has also been identified in *Ceriporiopsis subvermispora* [35]. *C. subvermispora* OxOx (*Cs*OxOx) is the first manganese-containing bicupin protein [67], and shares 49% sequence identity with *Bs*OxDC (Fig. 1.7). The heterologous expression and purification of recombinant *Cs*OxOx from *P. pastoris* produced oxalate containing 0.4 Mn per monomer. [68] *Cs*OxOx exhibited 0.6% OxDC activity, which was rationalized by the mis-protonation of the formyl radical intermediate. [69]

1.3.3 Proposed Mechanism for OxOx

In previous studies of *Hv*OxOx, the active form of manganese has been proposed to be Mn(III). [70] No activity was observed when manganese was fully reduced to Mn(II). [71] Mn(II) has been detected in both native and recombinant *Hv*OxOx using EPR spectroscopy. [72] [34] Addition of oxalate perturbs the EPR spectra of Mn(II) in OxOx significantly, indicating that oxalate may directly coordinate to the metal in the manganese binding site. [34] A weak 450 nm optical absorption was observed

[redacted]

Figure 1.8. Proposed catalytic mechanism of OxOx. Reprinted with permission from [70]. Copyright©2006 American Society for Biochemistry and Molecular Biology.

in OxOx, implying that small amount of Mn(III) might be present in OxOx. [34] These observation led to the mechanistic hypothesis that binding of oxalate changes the oxidation state of manganese to Mn(III), which facilitates the breaking of C-C bond. Substrate inhibition at steady state velocity was observed at high oxalate concentrations in rapid kinetics experiments. [71] This substrate-dependent inhibition was explained by tight-binding of the substrate and the incorrect form of the metal. Based on these observations, Whittaker et al. proposed a catalytic mechanism for OxOx [70] (Fig. 1.8). The catalytic cycle starts with the activation of Mn(II) to form Mn(III) due to the binding of oxalate, which then yields a oxalate radical. This step is followed by the reduction of manganese and the formation of a formyl radical anion intermediate and carbon dioxide. Then the manganese-bound superoxide radical is protonated by water to give hydrogen peroxide, and the enzyme finally cycles the metal back to Mn(II).

1.4 Sequence Alignment of OxDC and OxOx

A sequence alignment of the loop regions of several putative OxDCs together with OxOxs is showing in Fig. 1.9. A full sequence alignment shows in Appendix A.

```
Oxalate decarboxylase OxdC [Bacillus subtilis (strain 168)]       143  QAL---EEGAEFLLVFDDGSFSENSTFQLTDWLAHTPKE
Oxalate decarboxylase [Bacillus pumilus (strain SAFR-032)]        144  QAL---EPGAEFLLVFDDGSFSENSTFQVTDWLAHTPEE
Oxalate decarboxylase [Bacillus clausii (strain KSM-K16)]         153  QGL---DDGCEFLLVFDDGMFSDLSTLSLSDWMAHTPKD
Oxalate decarboxylase [Bacillus licheniformis]                    143  QAL---EDGCEFLLVFDDGSFSENSTFQVTDWLAHTPDE
Oxalate oxidase-C [Ceriporiopsis subvermispora (strain B)]        216  QGTdanNEGSEFLLIFPDGTFDSSNQFMITDWLAHTPKD
Oxalate oxidase-G [Ceriporiopsis subvermispora (strain B)]        220  QGTnasDEGSEFLLIFPDGTFDASNQFMITDWLAHTPKD
```

Figure 1.9. A sequence alignment of the loop regions of putative OxDCs together with OxOxs.

According to this sequence alignment, OxOx and OxDC share the same metal binding motifs. The loop sequence is conserved in OxDC, while the corresponding region in OxOx sequences exhibits some variation.

Although sequence alignments based on *Bs*OxDC and *Hv*OxOx reveal a large number of putative OxDC and OxOx in various species, very few of these proteins have been investigated, and the true enzymatic activity of these gene product have not been experimentally confirmed. Since OxDC and OxOx activity are easily switched by mutations at several residues, annotating the gene products simply based on their sequence similarity is unreliable. For instance, the loop region in the fungal OxOx may be different from the corresponding region in plant OxOx. This seems reasonable because the sources of these enzymes come from different kingdoms. This is also intriguing because it suggests that the sequence of the loop region in OxOx is not as strictly conserved as the N-terminal loop in OxDC. Therefore, it is possible that fungal OxOx and plant OxOx use different mechanisms to catalyze the oxidation of oxalate. It is also possible that the sequence of the loop region in OxOx is not crucial for enzyme activity. However, the fact that the *Cs*OxOx loop variants containing the residues in *Bs*OxDC showed neither OxDC activity nor OxOx activity [68] seems to argue against the latter hypothesis. The role of the loop region and the activity switch that has been observed in the OxDC loop variants needs further investigation in order to understand the mechanism of OxOx.

1.5 Project Objectives

The work in this thesis seeks to address the following questions: (1) does the oxidation state of manganese change during the catalysis of OxDC (Chapter 3), (2) what is the contribution of the loop residues in switching of catalysis from that of OxDC to OxOx in the chimeric mutation, and what information we can obtain from these variants to learn about the mechanism of OxDC (Chapter 4), (3) what is the role of the second shell residues and can we manipulate the enzyme activity by mutating these residues (Chapter 5), and (4) can a cleavable OxDC be created to probe the interaction between the N-terminal and the C-terminal domain in OxDC (Chapter 6)?

In order to answer the questions above, a series of single-site and multi-site mutations were designed. These mutations were mostly located around the manganese centers of the N-terminus and C-terminus and the N-terminal lid area. Characterization of these OxDC variants employed various techniques, including steady-state kinetics, membrane inlet mass spectroscopy, kinetic isotope effect determinations, electron paramagnetic resonance spectroscopy, and X-ray crystallography.

2. METHODOLOGY

2.1 Standard Kinetic Assays

2.1.1 Formate Dehydrogenase Assay

The standard steady-state kinetic parameters for OxDC activity were determined by a coupled assay using formate dehydrogenase (FDH) [73] [48] (Fig. 2.1). This end-point assay measures formate produced in the OxDC-catalyzed reaction by following the conversion of NAD^+ to NADH in the FDH coupled reaction. Briefly, NAD^+ added to the quenched reaction mixture is converted to NADH in the presence of FDH, and the characteristic absorption at 340 nm of NADH was detected using UV-Vis spectroscopy. The coupling reaction requires overnight incubation at 37 °C. In order to eliminate the problems arising from the stability of NAD^+ at 37°C, a standard curve was established using a series of known formate concentrations, which were incubated with FDH under the same conditions.

[redacted]

Figure 2.1. NADH production in the FDH assay.

2.1.2 ABTS-Peroxidase Assay

The OxOx activity was also measured using a coupled assay. [72] However, the hydrogen peroxide production was determined in a continuous assay whereby 2,2'-

azino-bis(3-ethylbenzothiazoline-6-sulphonic acid) (ABTS) was oxidized by hydrogen peroxide to yield the ABTS radical cation in presence of horseradish peroxidase (HRP). The concentration of the ABTS radical anion was determined by UV-Vis spectroscopy based on its characteristic absorption at 600 nm from the Lambert-Beer Law.

[redacted]

Figure 2.2. H_2O_2 detection using ABTS-Peroxidase assay.

This assay is more complicated and potentially more error-prone than a direct assay. It has also been reported that OxDC exhibits an oxalate-dependent dye reaction, which results in the oxidation of ABTS in the absence of Peroxidase. [72] Thus, in acidic conditions, oxalate is able to reduce the ABTS radical cation to ABTS. [74] To eliminate the influence of the side reactions, careful control experiments were carried out for each sample. Ideally, using a direct method for both enzyme activities instead of two coupled assays would give more accurate results when comparing the OxDC activity and OxOx activity of OxDC variants.

2.2 Membrane Inlet Mass Spectroscopy

MIMS is a technique that permits the detection of small neutral gases in solution. [75] It is a real-time measurement, and can be used to determine different gas species, such as CO_2, O_2 and N_2, in aqueous solution at the same time. MIMS therefore is an ideal method for enzymatic reactions that involve gas consumption and production.

2.2.1 Instrument Set-up

The equipment for MIMS is similar to GC-MS except the sample inlet contains a semipermeable membrane that allows only gas molecules to pass through the membrane for analysis (Fig.2.3). An inlet with the semi-permeable membrane at one end is inserted into the reaction chamber. The other end of the inlet is connected to a cold-trap, which removes any water vapor evaporated from the solution in the reaction chamber. A vacuum is applied to membrane inlet and the metal tubing connected to the mass spectrometer before the experiment. In the measurement, gas molecules dissolved in the reaction solution pass through the membrane, and are ionized to produce a population of positive ionic species. These species are detected and analyzed by mass spectrometry.

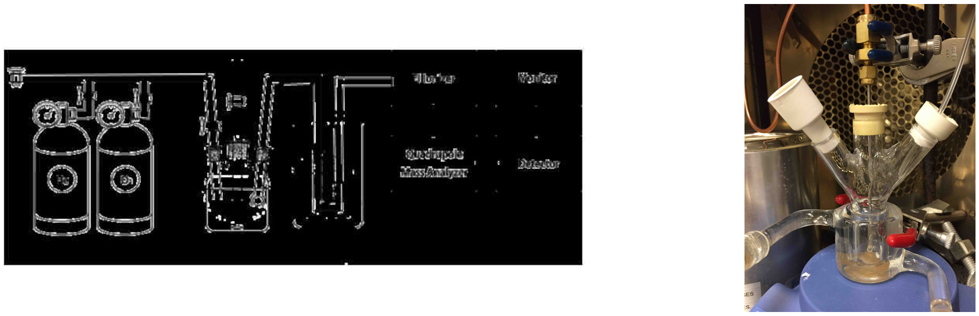

(a) Instrument set-up

(b) Reaction chamber of MIMS

Figure 2.3. Membrane inlet mass spectrometer set-up.

2.2.2 Using MIMS to Determine Kinetic Parameters

The application of MIMS in physiological samples and organic compounds has been well-described. [76] Moral et al. and Moomaw et al. have reported the determination of kinetic parameters for WT *Bs*OxDC and *Cs*OxOx by MIMS, respectively. [77] [78] The results obtained from the MIMS measurements were comparable with those obtained using the standard assays, confirming that MIMS can be used in the determination of decarboxylase and oxidase activities. The MIMS technique is able to simultaneously monitor the consumption of O_2 and production of CO_2 in reactions catalyzed by OxDC and OxOx. Importantly, this technique can be used in the study of enzymes that exhibit both OxDC and OxOx activity, such as some of the OxDC loop variants (see Chapter 4).

Initiation of the reaction by addition of enzyme leads to CO_2 production, which is shown by an increase in the signal m/z 44. The slope of the linear portion of the signal (within 30 s) provides the initial velocity of the enzyme reaction under the experimental conditions. The reaction conditions can be controlled by adjusting the aqueous and gas components in the reaction mixture. A deoxygenated environment was created by sparging with helium before the initiation of the reaction. In order to eliminate the effect of dissolved CO_2 in the buffer and protein solution, 1,2-^{13}C-oxalate was used as the substrate, so the resulting $^{13}CO_2$ gives an ion current for m/z 45 instead of m/z 44.

As MIMS records the ion current for the gas molecules, a standard curve was required to convert the ion current signal to concentration. CO_2 standards were prepared at a series of known concentrations of potassium carbonate in acetate buffer. At pH 2.0, the carbonate added to the acetate buffer becomes carbonic acid, thereby generating CO_2. [77] Therefore, the slope in calibration plots gives the relation between the molarity of the dissolved CO_2 in solution and the ion current recorded by MIMS.

A calibration for O_2 was performed by adjusting the proportion of O_2-saturated water in the 2 ml volume of the reaction mixture. The solubility of O_2 in water is 1321.5 μM at 25 °C. A series of O_2-saturated water samples of known volume were mixed with degassed reaction buffer in the reaction chamber, so that the concentration of O_2 in the chamber was equal to the concentration of O_2 contributed by the

O_2-saturated water. The slope in the calibration plots of O_2 signal *versus* O_2 concentration provided the conversion factor relating the ion current signal to molarity.

2.2.3 Using MIMS to Probe the Functional Role of Dioxygen

MIMS was used to probe the functional role of O_2 by measurements of steady-state kinetic parameters in the presence of different O_2 concentration in the reaction mixture.

Methylamine hexamethylene methylamine (MAHMA) NONOate was used to generate NO in acidic solution [79] (Fig. 2.4).

[redacted]

Figure 2.4. NO production under acidic condition.

OxDC is active at pH 4.2, [61] allowing the rapid conversion from MAHMA to NO. Using MIMS, the inhibitory effect of adding of MAHMA into the OxDC reaction mixture was determined by monitoring the production of CO_2, consumption of O_2, and the change of NO signal in real-time.

2.3 Kinetic Isotope Effects

Kinetic isotope effect (KIE) measurements have made a great contribution in the mechanistic study of many enzymes. [80] [81] In general, KIEs reflect the change of reaction rate caused by the substitution of one of the atoms in the substrate for one of its isotopes. [82] When a heavier isotope is substituted for a lighter one, the zero point energy of the bond containing connects to the substituted isotope is different in the substrate and transition state. Therefore, substitution of the heavier isotope will affect the reaction rate. KIEs are determined by how loose or weak the bond is in both the substrate and the transition state, which is useful in study of the transition state structure in the enzymatic reaction. [83]

Although the principle behind KIEs is fairly simple, it is not easy to apply it to specific cases in biochemical reactions, because many enzymatic reactions are complicated, and the value of KIEs could be very small and easily masked by experimental error.

OxDC catalyzes the cleavage of the chemical bond between two carboxylate groups. [17] This reaction could be affected by the substitution of atoms such as ^{13}C and ^{18}O. For OxDC, isotope effects (IEs) arising from C-C bond breaking by substitution of ^{13}C are primary isotope effects (PKIEs), which measure the IE for breaking/forming of the bond that directly connected to the isotope. IEs from the substitution of ^{18}O are secondary isotope effects (SKIEs).

Using KIEs as a tool to probe enzyme mechanisms involves four steps: 1) establish a proper measurement method, 2) establish a reaction model and derive equations for the IEs, 3) perform experiments to determine the isotope effects (IEs) and 4) analyze and interpret the data.

Three methods can be used to measure KIEs: direct comparison of initial rate, equilibrium perturbation and internal competition. [84] The internal competition method was employed in the study of WT OxDC KIEs. [61] This method gives the IEs on V_{max}/K_M) (V/K) based on the different distribution of the heavier atom and the lighter atom in the substrate and the product. Because the IEs measured by the internal competition method only affects the V/K, it only gives the information in steps up to, and including, the first irreversible step. This method is also the most sensitive one for determining of heavy atom KIEs, such as ^{13}C and ^{18}O, which are relatively small compared to deuterium IEs. [85] In addition, no need to use synthetic isotope-labeled substrates because commercially available oxalate contains sufficient heavy isotopes for both carbon and oxygen. This simplifies sample preparation for the experiment.

The internal competition method required direct measurement of the ratio of the lighter atom to the heavier atom in the substrate and product. This ratio was obtained accurately by the isotope ratio mass spectrometer (IRMS), which is specifically designed for measurement of gas molecules. One of the products of the OxDC reaction is CO_2, which was analyzed directly using IRMS to determine the ratios of ^{12}C to ^{13}C and ^{16}O to ^{18}O. Oxalate and formate, which can not be directly analyzed by IRMS were oxidized by iodine in dimethyl sulfoxide (DMSO) to yield carbon dioxide and the ratios of ^{12}C to ^{13}C, and ^{16}O to ^{18}O. This chemical conversion does not alter the ratios of carbon or oxygen isotopes in oxalate or formate.

The experimental design for determining the distribution of isotopes in the substrate and each product is shown in Fig 2.5.

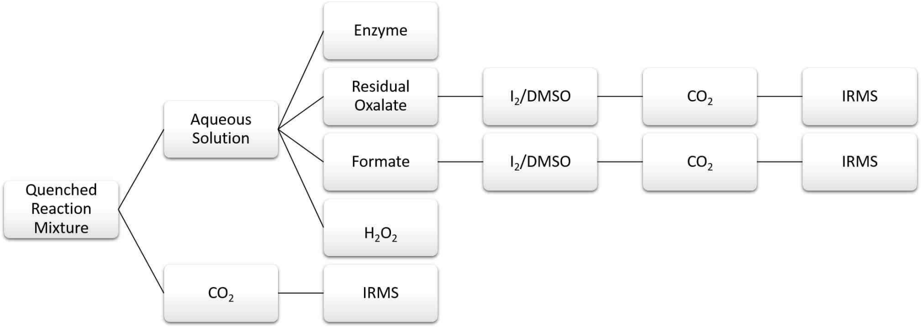

Figure 2.5. The expermental design for determine the KIEs of OxDC

Using this method, the isotope ratio in CO_2 ($R_{(CO_2)}$), oxalate (R_0), formate ($R_{formate}$) and the residual oxalate (R_s) in quenched reaction was determined. The fraction of reaction (f) was obtained by measuring residual oxalate and the product produced in the quenched reaction. The apparent IE was calculated using the following equation [86]:

$$\mathrm{IE_{app}} = \frac{ln(1-f)}{ln[(1-f)\dfrac{R_s}{R_0}]} = \frac{ln(1-f)}{ln[1-f\dfrac{R_{formate}+R_{\mathrm{CO_2}}}{R_0}]} \tag{2.1}$$

Under steady-state conditions, only V/K was affected by the competition between the isotope-containing oxalate and the regular oxalate during catalysis. The expression for interpretation of the V/K in the KIEs of OxDC was based on the concept of net rate constants, as proposed by W. W. Cleland in 1975. [86]

[redacted]

Figure 2.6. Model of a minimal enzyme kinetic mechanism.

The expression [61] of the V/K for the reaction mechanism above using the net rate constants is

$$V_{max}/K_M = [E_0]\frac{k_1k_3k_5}{k_2(k_4+k_5)+k_3k_5} \tag{2.2}$$

Applying this simplified model [61] to the OxDC catalyzed reaction gave a minimal mechanism up to and including the first irreversible step:

[redacted]

Figure 2.7. Model of minimal kinetic mechanism of OxDC.

This mechanism led to the following expression of IEs on V/K for the ratios of ^{12}C to ^{13}C and ^{16}O to ^{18}O assuming that the isotope-sensitive steps are k_3, k_4 and k_5:

$$(V/K)^x = \frac{{}^xK_{eq3}{}^xk_5 + {}^xk_3(\dfrac{k_5}{k_4}) + \dfrac{k_3k_5}{k_2k_4}}{1+(\dfrac{k_5}{k_4})(1+\dfrac{k_3}{k_2})} \tag{2.3}$$

where $(V_{max}/K_M)^x$ denotes the ratio of the IEs of ^{13}C and ^{18}O when $x = 13$ or 18, $^xK_{eq3}$ denotes the equilibrium constants when k_3 and k_4 are affected by the isotope substitution, which equals to the ratio of k_3k_4 for lighter atom and heavier atom.

KIEs were used to predict the bond order in the transition state, which is an important approach for elucidation of transition state structures that cannot be detected by spectroscopic methods. [83] The linear relation between the C-O bond order and the fractionation factors of ^{13}C and ^{18}O of oxalate relative to CO_2 has been calculated and reported in the literature. [61] Expressions [61] for the relationship between the C-O bond order and the fractionation factors of ^{13}C and ^{18}O were:

$$\mathrm{C{-}O\,bond\,order}_{^{13}\mathrm{C}} = \frac{f.f. - 0.8955}{0.0582} \tag{2.4}$$

$$\mathrm{C{-}O\,bond\,order}_{^{18}\mathrm{O}} = \frac{f.f. - 0.9047}{0.0418} \tag{2.5}$$

where the $f.f.$ denotes the fractionation factors that were calculated from K_{eq}.

2.4 Electron Paramagnetic Resonance Spectroscopy

2.4.1 Theory of the EPR Spectroscopy

EPR spectroscopy is a powerful tool for investigation of chemical species with unpaired electrons, such as radicals and transition metal complexes. [87] The principles of EPR are similar to those of nuclear magnetic resonance (NMR), except for electron spins rather than spins of nuclei. [88] Electrons have a magnetic dipole due to their spin. Each electron has two possible magnetic spin states, denoted by the spin quantum number, m_s=+1/2 or m_s=-1/2. When an electron is exposed to an external magnetic field B_0, the magnetic moment of the electron aligns itself either parallel or anti-parallel to the magnetic field (the Zeeman interaction). The anti-parallel state is of a higher energy and the difference in the energy levels between the two states is proportional to the magnetic field (Fig. 2.8). [89]

The transition of an electron between the two energy levels can be induced by radiation applied at the resonance frequency. The relationship between the radiation frequency, the transition energy and the external magnetic field is shown as below:

$$\Delta E = \hbar\nu = \mu_B g_e B_0 \tag{2.6}$$

where $\hbar$ is the plank constant, ν is the frequency of the radiation, g_e is the g-factor for a free electron, which is 2.00232, μ_B is the Bohr magneton and B_0 is the external magnetic field.

[redacted]

Figure 2.8. A simplified energy levels of the electron splitting of Mn in the presence of external magnetic field.

2.4.2 EPR Spectroscopy of Manganese

In most cases, the electronic environment is complicated by the presence of multiple electrons, especially for the transition metals with high spin state configurations. Factors that affect EPR spectra include the interaction between different electrons and the nuclei associated with those electrons. Unpaired electrons in the *d* orbital contribute to an asymmetrical distribution of electrons between the orbitals, which contributes to the magnetic moment resulting in a change in the *g*-value. Ligand around the metal in enzyme could affect the degeneracy and energy of the d-orbitals. This zero-field splitting (zfs) contributes to the characteristics of the EPR signal. Nuclei also create magnetic fields further complicate the EPR spectra, resulting in hyperfine splitting. In the case of Mn(II), there are five *d*-orbital electrons. The high spin state of the Mn(II) corresponds to a half-filled orbital that exhibits a symmetrical structure in free solution. The spin states of the Mn(II) include ±1/2, ±3/2, ±5/2, which results in five transitions between consecutive spin levels ($\Delta M_s = 1$) that can be detected by EPR. The nucleus of Mn with I=5/2 nuclear spin has a hyperfine interaction between the energy levels ($\Delta M_I = 0$), which contributes to the characteristic six-lined Mn EPR signal. When the coordination of the ligands is totally symmetric, such as the case in free solution, the zfs can be ignored and the g-value is close to g_e. The existence of any asymmetric or distorted coordination leads to a high zfs and more than one set of sextet signals is then detected.

2.4.3 Different Types of EPR

The EPR spectrum is obtained at a fixed microwave frequency with variation of the external magnetic field, B_0. This type of EPR is called continuous wave (CW) EPR. Depending on the applied frequency the external field, different types of EPR, including X-band (8-12 GHz), Q-band (30-50 GHz), W-band (75-110 GHz), *etc.*, have been developed. [88] CW EPR allows the observation of the fine structure of the metal and provides information about hyperfine-splitting, and can be employed to detect the oxidation state of the metal and coordination geometry. [90]

In standard measurement using X-band EPR, the modulating magnetic field is perpendicular to the applied field. This is called perpendicular mode EPR, which allows the detection of the transitions for systems with fractional spin, such Mn(II) (S = 5/2). The characteristic signal of Mn(II) in OxDC can be observed in perpendicular polarization EPR, and corresponds to the M_s = -1/2↔+1/2 hyperfine-split central field transition. Transitions at lower field indicate the existence of different coordination geometries for manganese.

Species with integer spin value, such as Mn(III) (S = 2), are not detectable using perpendicular EPR. Normally, the splitting energy for a integer system is greater than the radiation used in X-band perpendicular mode EPR, which leads to a signal too broad to be seen in the perpendicular mode, even at very high field. However, when an oscillating magnetic field is applied parallel to B_0, the transition between $M_s = \pm 2$ can be observed. Therefore, Mn(III) signals can be detected using parallel mode EPR. The six-lined splitting arises from the nuclear moment, I = 5/2, and is not affected by the oxidation state of the metal.

More detailed information about the hyperfine-structure of the metal can be obtained by the use of high-frequency EPR (HFEPR), allowing the determination of zfs parameters D and E in the system spin Hamiltonian describing the symmetry of the system.

2.4.4 Spin-trapping Experiment

The application of EPR spectroscopy in the studies of OxDC not only focused on the investigation of manganese properties, but also the identification of radicals produced during the catalytic turnovers. [91]

Due to the existence of the manganese EPR signal, the direct identification of the radical intermediate in OxDC-catalyzed reaction was difficult. Also, the radical intermediate was present only transiently, and was therefore undetectable by direct EPR spectroscopy on the enzyme. Converting radical intermediate into a more stable radical was used in the identification and interpretation of EPR spectra.

N-tert-butyl-α-phenylnitrone (PBN), [62] α-(4-Pyridyl N-oxide)-N-tert-butylnitrone (POBN) [56] and 5,5-dimethyl-1-pyrroline-N-oxide (DMPO) [92] are spin-trapping reagents, which have been used to determine the existence of formyl radicals and superoxide radicals during catalysis of WT OxDC and some variants (Fig. 2.9).

[redacted]

Figure 2.9. The spin-trap reagent could react with the proposed radical intermediate in the OxDC-catalyzed reaction.

Based on the characteristic splitting of the signal observed for the radical adducts, the species of the radicals formed during the catalysis were determined. In addition, the intensity difference observed in the spectra of the spin-trapped EPR of WT OxDC and the variants was proportional to the amount of the radical that was trapped by the reagent. Using a standard curve, the intensity of the EPR signal was converted to the concentration of the radical adduct. 2,2,6,6-tetramethyl-1-piperidinyloxy (TEMPO) radical was used in the quantification of spin-trapped radicals due to its excellent stability. Plotting the EPR signal intensity of TEMPO and its concentration provided a standard curve for estimating the concentrations of PBN-trapped radicals.

3. CHARACTERIZATION OF MANGANESE IN THE RECOMBINANT *B. SUBTILIS* OXDC

3.1 Introduction

The activity of OxDC depends on the incorporation of manganese in both metal binding sites of the protein and the presence of O_2 in the solution. [43] Although a previous EPR study on the *Bs*OxDC was able to confirm the existence of Mn(II) in the recombinant OxDC from the *E. coli* expression system, [91] a circular dichroism spectrum of WT OxDC suggested that there was a small amount of Mn(III) in the purified protein. [56] In addition, WT OxDC exhibited 16% activity under anaerobic conditions, with 95% of the OxDC activity was recovered when O_2 being re-introduced into solution. [43] The failure to completely inactivate the enzyme using anaerobic conditions was rationalized by postulating the presence of tightly-bound oxygen in the enzyme. As described in Chapter 1, the role of O_2 has been proposed as mediating oxidation the Mn(II) ion into a higher oxidation state, such as Mn(III). A major issue with this hypothesis, however, is the mismatched reduction potentials of O_2 and Mn(III), [52] and a dearth of model Mn-containing inorganic complexes capable of binding dioxygen. [53] In the absence of direct experimental evidence, the existence of a redox change in manganese during catalysis has been controversial. The goal of the work presented in this chapter is to investigate whether the oxidation state of manganese in WT OxDC changes during catalysis BY EPR spectroscopy.

3.2 Results and Discussion

3.2.1 Protein Expression, Purification and Kinetics Determination

A modified expression and purification protocol was used to obtain the recombinant protein in a yield of was 40 mg/L with metal content in the purified enzyme of 1.5 Mn/monomer. The content of iron, copper, magnesium and zinc was less than 0.01 atom/monomer (Table 3.1). Enzyme activity at pH 4.2 ($K_M = 2.0 \pm 0.4$ mM; k_{cat}/K_M/Mn: 10000 ± 1000 M^{-1} s^{-1}) was determined by measuring CO_2 production using membrane-inlet mass spectrometry. Briefly, WT OxDC was added into a reaction mixture containing $^{13}C_2$-oxalate to initiate reaction, and the current of the m/z 45 ion ($^{13}CO_2$) was monitored (Fig. 3.1). This ion current was then converted to concentration using a CO_2 standard curve. The reaction rate at different oxalate concentrations was fitted to the Michaelis-Menten equation (Fig. 3.2). The formation of formate was confirmed using the FDH-based assay. The V_{max} (29 ± 3 U/mg) was also determined under the conditions used in the EPR measurements. The buffer used for the EPR measurements differed from that used in the normal kinetic assays as described in the experimental section. The V_{max} of WT OxDC in this poly-buffer, as determined using the FDH assay, was 1.4-fold lower than the value obtained in the standard buffer used in the MIMS-based kinetic assay.

Table 3.1.
Metal content of WT OxDC used in the WT OxDC EPR studies.

	Mn	**Fe**	**Cu**	**Zn**	**Mg**
Amount (ppb)	6337	12.69	0.10	2.16	5.57
Metal/Monomer	1.5302	1.6×10^{-3}	2.3×10^{-5}	3.6×10^{-4}	2.9×10^{-3}

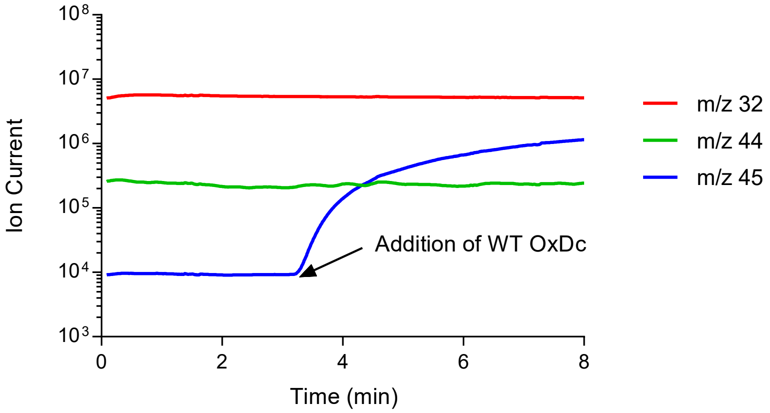

Figure 3.1. Example of MIMS data used to determine the steady-state kinetic parameters of OxDC.

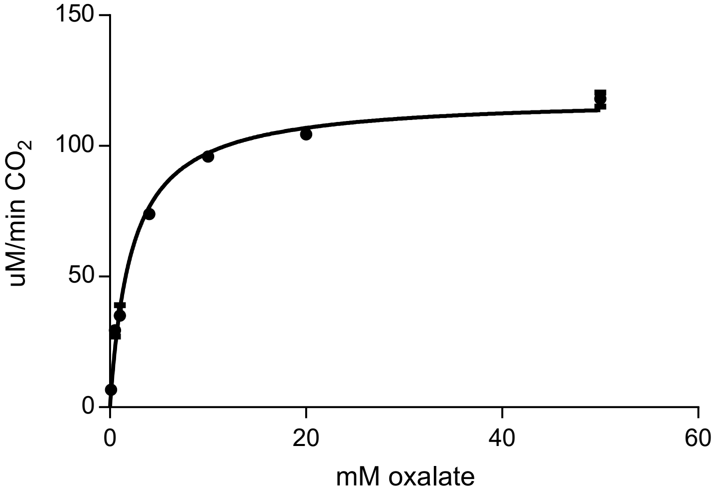

Figure 3.2. The Michaelis-Menten curve constructed from analysis of the MIMS data of WT OxDC.

3.2.2 X-band EPR Spectroscopy of WT OxDC

EPR spectroscopy was used to characterize the properties of the manganese centers in WT OxDC at three different pH values. These were chosen at the basis of the pH profile of OxDC reported in the literature; pH 4.2 is the optimal pH for WT OxDC, while at pH 5.7, the rate of the OxDC-catalyzed reaction is 2-fold lower. At pH 8.5, no activity is observed because only the mono-protonated form of oxalate is the true substrate Perpendicular and parallel mode EPR spectra of WT OxDC were taken at pH 8.5, pH 5.7 and pH 4.2 in the presence or absence of 100 mM oxalate. The protein concentrations in each sample are given in Table 3.2.

Table 3.2.
Final concentration of WT OxDC used in the EPR studies

pH	$[\mathrm{WT}]_{\mathrm{absenceofoxalate}}$	$[\mathrm{WT}]_{\mathrm{presenceofoxalate}}$
4.2	590 ± 90 μM	460 ± 90 μM
5.7	590 ± 90 μM	460 ± 90 μM
8.5	570 ± 70 μM	460 ± 90 μM

Spectra of WT OxDC in the Absence of Oxalate

As reported previously, [91] a characteristic sextet signal for the transition of Mn(II) at $g = 2.0$ in perpendicular mode EPR was observed at all three pH values (Fig. 3.3). The features centered at 150 mT ($g = 4.3$) can be attributed to the half-field transition, which is typically 100-fold lower than in intensity the $\Delta M_I = 1$ transition. [43] The signal at $g = 4.3$ observed at pH 8.5 is only about 2-fold lower than the signal at $g = 2$, which is much more intense than the typical half-field transition only. This suggests that some Mn(II) exists in more than one environment, which is usually associated with the penta-coordinated Mn(II) in tetrahedral or highly unordered octahedral coordination. The splitting in the sextet signal at $g = 4.3$ also supports the presence of differently coordinated Mn(II) ions in the protein at high pH. As the pH decreases, the signal at $g = 4.3$ is decreased about 6-fold, which may indicate transformation of the penta-coordinate Mn(II) to its hexa-coordinate form. HFEPR studies of OxDC [49] have suggested that the pH change affects the geometry of the ligands around the metal.

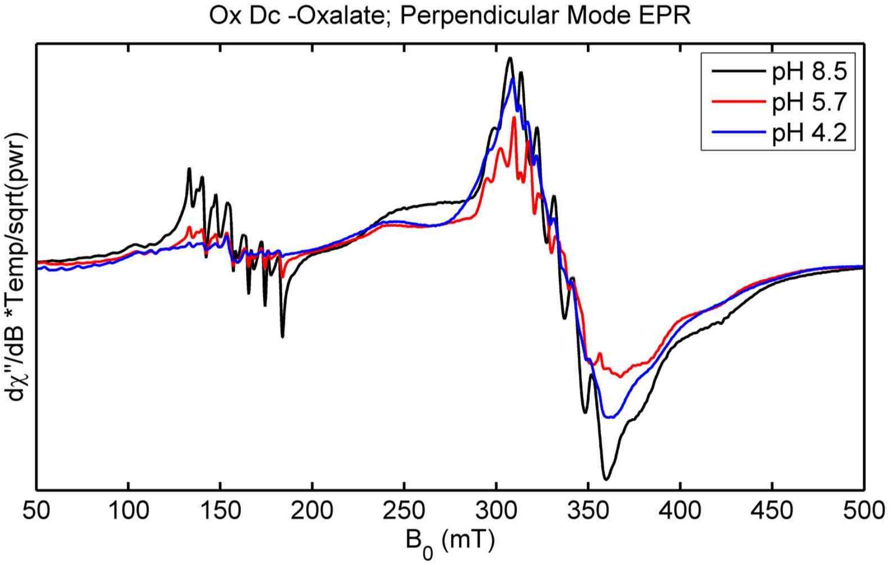

Figure 3.3. Perpendicular mode EPR spectra for WT OxDC in the absence of oxalate at pH 8.5 (black), pH 5.7 (red) and pH 4.2 (blue). Figure was prepared by Dr. J. Wilcoxen.

The parallel mode EPR spectrum of WT OxDC at pH 8.5 exhibited a distinctive sextet signal centered around 130 mT, corresponding to the $M_s = \pm 2$-transition of Mn(II) (Fig. 3.4). This signal also exhibits the same pH dependency as the signal in the perpendicular mode EPR. No Mn(III) signal was present under these conditions.

Spectra of WT OxDC in the Presence of Oxalate

The EPR spectra of the protein samples in the presence of oxalate was determined using both perpendicular mode and parallel mode EPR at different pH values. At pH 8.5, the EPR spectrum of WT OxDC in the presence of 100 mM oxalate under perpendicular mode did not differ significantly from that of the free enzyme (Fig.

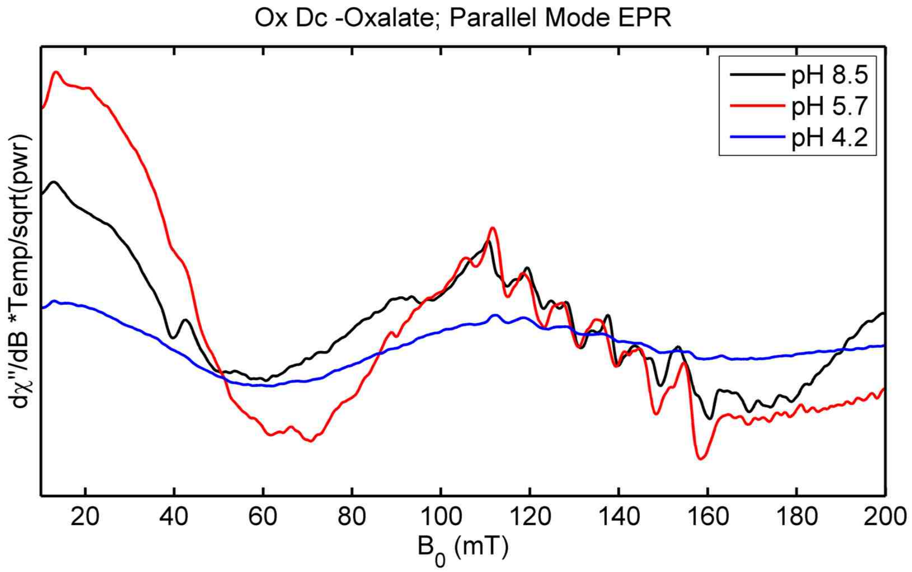

Figure 3.4. Parallel mode EPR spectra for WT OxDC in the absence of oxalate at pH 8.5 (black), pH 5.7 (red) and pH 4.2 (blue). Figure was prepared by Dr. J. Wilcoxen.

3.5). The presence of oxalate at pH 5.7 and pH 4.2, where WT OxDC exhibits catalytic activity, led to substantial changes in the perpendicular mode EPR spectra compared to the free enzyme. In addition to the small signal at $g = 4.3$, which had already been observed , a new feature appeared on the shoulder of the sextet signal at $g = 2.0$. The broad peaks around 234 mT, 305 mT and 380 mT likely arise from a change of environment in the two metal binding sites. [90] Moreover, these features only appeared under conditions in which OxDC is catalytically active, indicating that these changes might result from substrate binding.

At pH 8.5, the parallel mode EPR spectra of OxDC in the presence and absence of oxalate were similar (Fig. 3.6), as seen in the perpendicular mode EPR spectra at the same pH. However, at pH 5.7 and pH 4.2, the parallel mode EPR spectra of OxDC with oxalate exhibited significant differences from the spectra of the free enzyme. As well as the forbidden-transition signal that had been observed previously, [43] a new

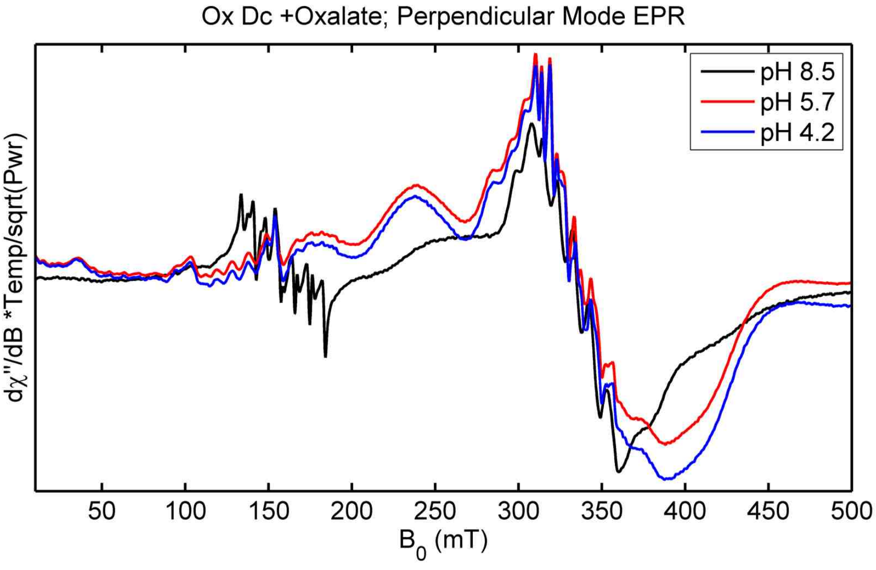

Figure 3.5. Perpendicular mode EPR spectra for WT OxDC in the presence of 100 mM oxalate at pH 8.5 (black), pH 5.7 (red) and pH 4.2 (blue). Figure was prepared by Dr. J. Wilcoxen.

sextet signal centered near 75 mT appeared in the parallel mode spectrum, which was hypothesized as arising from enzyme-bound Mn(III).

The spectrum of inorganic Mn(III)-pyrophosphate under parallel mode EPR was determined under the same conditions, and the characteristic sextet signal was again centered at the position as the signal was observed in the oxalate containing OxDC samples at pH 5.7 and pH 4.2 (Fig. 3.7). The concentration of the 200 μM Mn(III)-pyrophosphate was verified using UV-vis spectroscopy. To determine the concentration of OxDC, the peak-to -rough heights of the spectra containing Mn(III) signal in pH 4.2 solution were measured accounting for differences in each sample, and was calculated to be 95 μM Mn(III), or 40% of the catalytically active N-terminal Mn sites in OxDC.

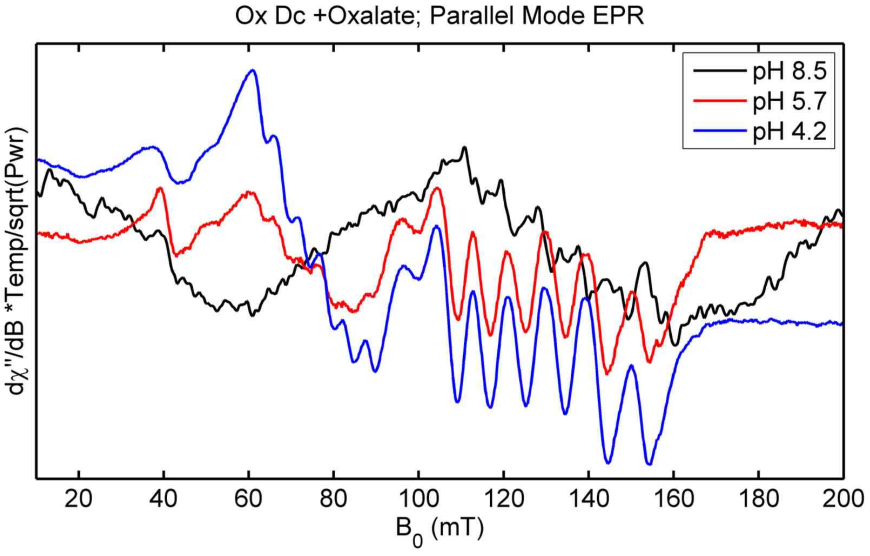

Figure 3.6. Parallel mode EPR spectra for WT OxDC in the presence of 100 mM oxalate at pH 8.5 (black), pH 5.7 (red) and pH 4.2 (blue). Figure was prepared by Dr. J. Wilcoxen.

Simulations of the EPR Spectra

Simulations were carried out using the EasySpin tool box (ver. 4.5.5) in Matlab (Mathworks Inc., Natick, MA) [93] to confirm the nature of the Mn species present in WT OxDC in the absence of oxalate. Parameters for the Mn(II) species reported previously [49] were used in the simulations of the parallel mode spectra, and the signal arising from the forbidden transition of the Mn(II) species in the parallel mode EPR spectra (Fig. 3.8) could be reproduced in the simulations (Fig. 3.9). Hyperfine features arising from the ^{55}Mn ($I = 5/2$) signals assigned to the enzyme-bound Mn(III)-oxalate complex and resting Mn(II) were well reproduced.

The parameters used in the simulation were based on those defined from the previous studies of the pH-dependence of high field perpendicular EPR (HFEPR) spectra for WT OxDC in the absence of oxalate over a range of 4.0-8.8. [49] There are two metal binding sites in OxDC, however, and the electronic environment of these two metals are slightly different due to the differences in second shell residues

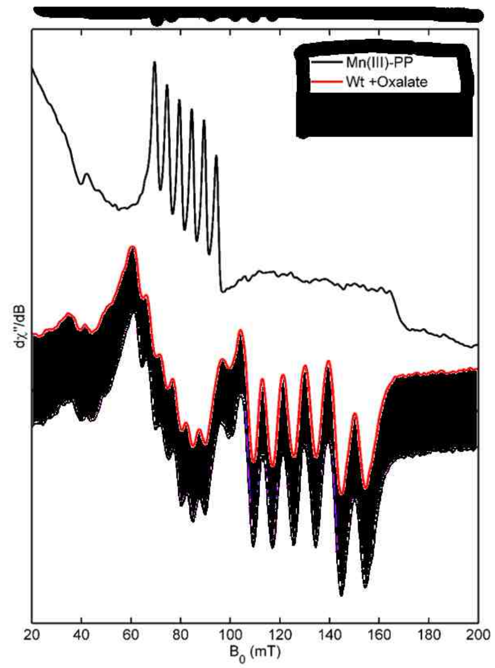

Figure 3.7. Parallel mode EPR spectra for manganese(III) pyrophosphate and WT OxDC in the presence of 100 mM oxalate at pH 5.7 (red) and pH 4.2 (blue). Figure was prepared by Dr. J. Wilcoxen.

around the metal. Changing the buffer pH affects the two sites in different ways based on these HFEPR measurement. In agreement with prior observations, the WT OxDC used in this study appear had a similar mix of species present in perpendicular mode EPR irrespective of whether oxalate was present. The geometry of the Mn(II) ion in the C-terminal domain likely alters with the pH of solution. The simulation was therefore carried out using this model, with the assumption that the C-terminal metal binding site has $pK_a = 4.2$. [49] Species M and L represent the two possible coordinations of the metal i the C-terminal metal binding site as proposed in the literature, and species A represents Mn(II) in the N-terminal metal binding site (Fig. 3.10). This simulation indicates that the forbidden-transition that was observed in

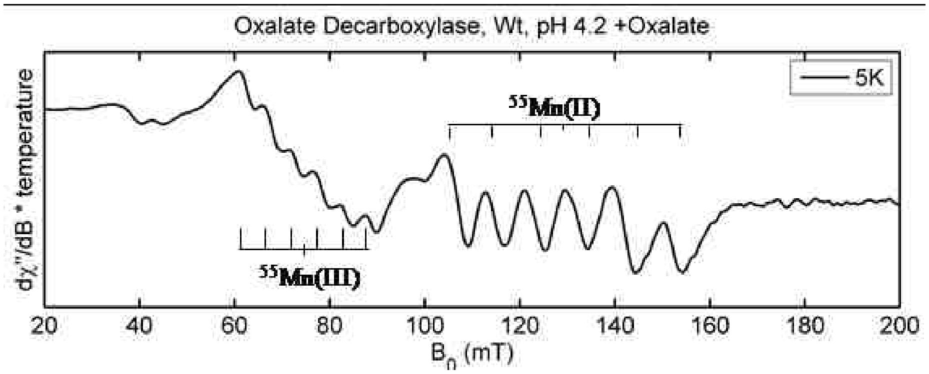

Figure 3.8. Spectrum of WT OxDC in the presence of oxalate at pH 4.2. "Goal Posts" indicate the Mn(II) and Mn(III) species present, distinguished by a ^{55}Mn hyperfine of 253 MHz for Mn(II) and 165 MHz for Mn(III). Figure was prepared by J. Wilcoxen.

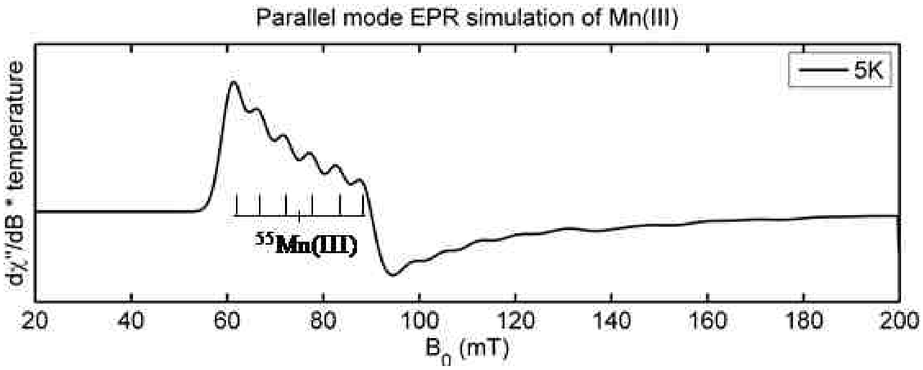

Figure 3.9. Spectral simulation of the spectrum shown with Mn(III) species indicated. Figure was prepared by J. Wilcoxen.

the parallel mode EPR spectrum arose from Mn(II) in the N-terminal domain (Fig. 3.11).

The sign of the zfs for the $S = 2$ species observed in parallel mode EPR was determined from the temperature dependence of the parallel mode EPR spectra of WT OxDC (Fig. 3.12). The Curie law behavior, represented by a decrease in the signal intensity with increasing temperature, gave a negative value for the zfs, with

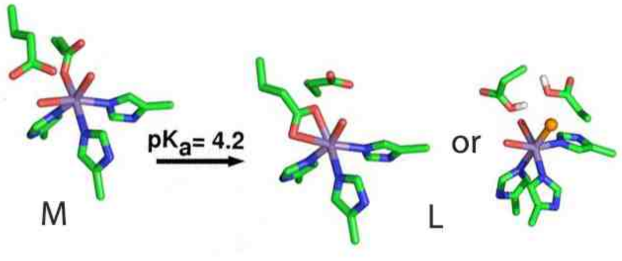

Figure 3.10. Proposed Mn(II) species present at pH 4.2. Adapted with permission from [49]. Copyright©2009 American Chemical Society.

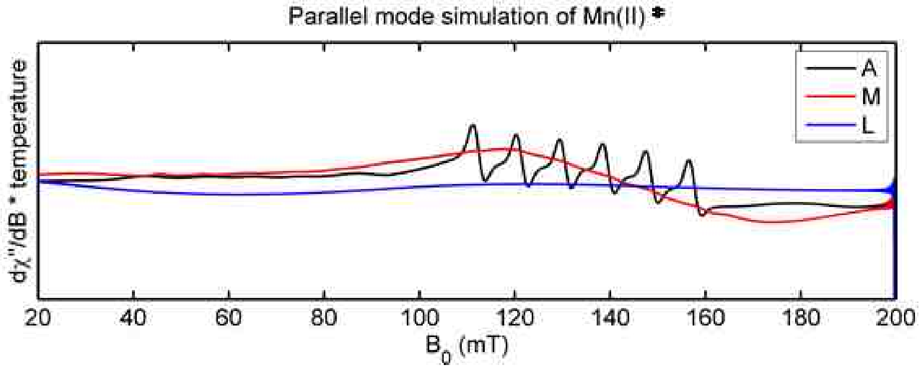

*Tabares et. al., *J. Phys. Chem* **2009**, 113, 9016-9025

Figure 3.11. Simulations of relevant Mn(II) species present at pH 4.2. Species A represent N-terminal site, low pH conformation, Species M and L represent equilibrium possible species at C-terminal site at low pH. Figure was prepared by Dr. J. Wilcoxen.

the following simulation parameters, D = -120 GHz and $|E|$ = 13.2 GHz, where D is the axial zfs parameter and E is the rhombic zfs parameter (Fig. 3.13).

The parameters used to simulate the Mn(III) species are similar to those used to model inorganic Mn(II) complexes containing a mix of oxygen and nitrogen ligands similar to those coordinating the two Mn ions in WT OxDC. [94] Importantly, the negative zfs value and magnitude of the hyperfine splitting indicates a $^5B_1$ symmetry ground state for either a six-coordinate, or five-coordinate square pyramidal Mn(III).

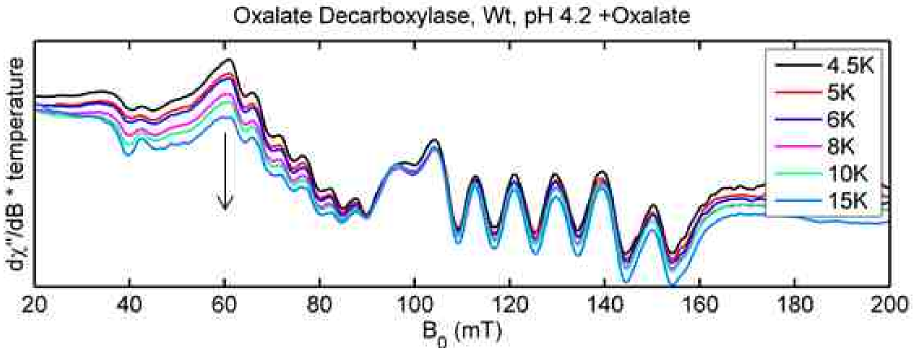

Figure 3.12. Temperature dependence of the EPR spectra of WT OxDC. Figure was prepared by Dr. J. Wilcoxen

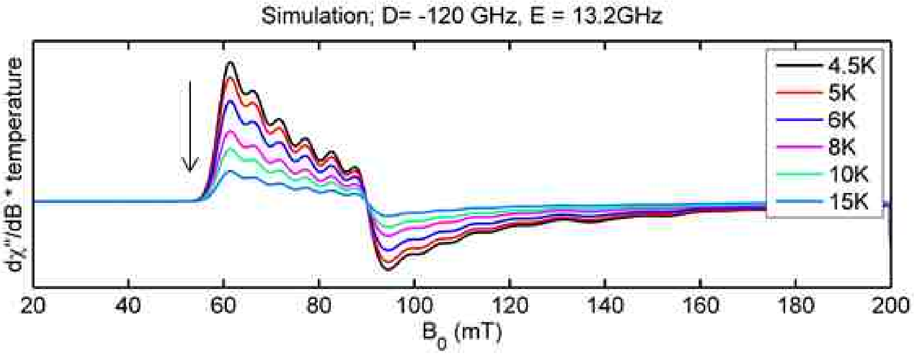

Figure 3.13. Simulation of the temperature dependence of a negative zfs of equal magnitude. Figure was prepared by Dr. J. Wilcoxen.

Given that there is no structural or spectroscopic evidence for the latter coordination, it seems likely that oxalate-binding results in the formation of a six coordinate Mn(III) species. This is the first unambiguous demonstration that the metal center is oxidized to Mn(III) in the presence of oxalate and O_2 under acidic conditions. In contrast to previous reports, the parallel mode EPR spectra of WT OxDC over the pH range 4.2-8.5 provide no evidence for the existence of Mn(III) in the recombinant enzyme as purified from *E. coli* in the absence of substrate.

EPR Spectra and the Reaction Coordination

In order to confirm that the Mn(III) species was found during catalytic turnover of OxDC, a spectrum of an OxDC/oxalate sample at pH 4.2, in which almost all the substrate had been consumed, was measured by parallel mode EPR (Fig. 3.14). The forbidden-transition of Mn(II) was observed together with a small Mn(III) sextet, which was decreased at least 20-fold compared to identical samples undergoing turnover. Any lingering Mn(III) is unlikely to arise from rebinding of formate in the presence of oxygen, given that the K_I for formate is larger than 200 mM (M. Moral unpublished data). Residual Mn(III) in the sample may also reflect a small amount of enzyme undergoing reaction during the measurement. The reduction in the Mn(III) signal with oxalate consumption supports the view that Mn(III) formation requires OxDC-mediated catalysis. When oxalate has been consumed, OxDC-bound Mn(III) is cycled back to Mn(II), perhaps with oxidation of a proximal tyrosine residue. [91]

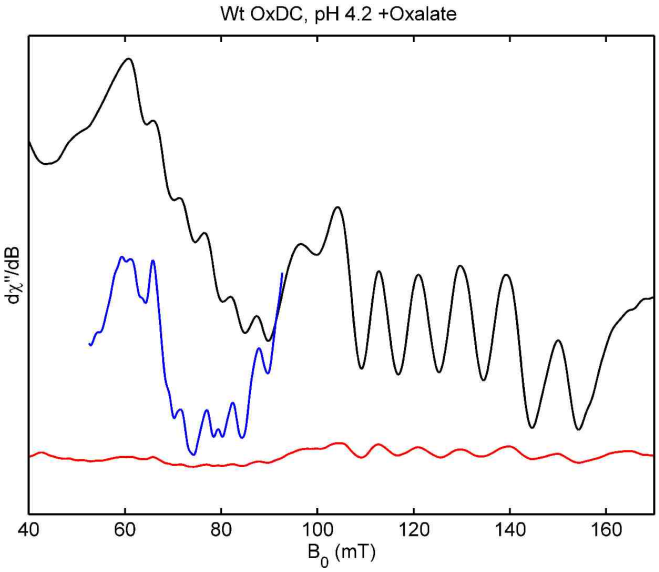

Figure 3.14. Parallel mode EPR spectrum of WT OxDC in the presence of 100mM oxalate at pH 4.2 frozen after 15 s (Black) and 5min (Red). The Red spectrum have been increased 20 fold to show Mn(III) in greater detail (Blue). Figure was prepared by Dr. J. Wilcoxen.

Parallel mode EPR spectra of samples subjected to rapid freeze quench (10 ms) (Fig 3.15), however, exhibited no observable Mn(III) signal, suggesting that Mn(III) forms during turnover, and after oxalate binding.

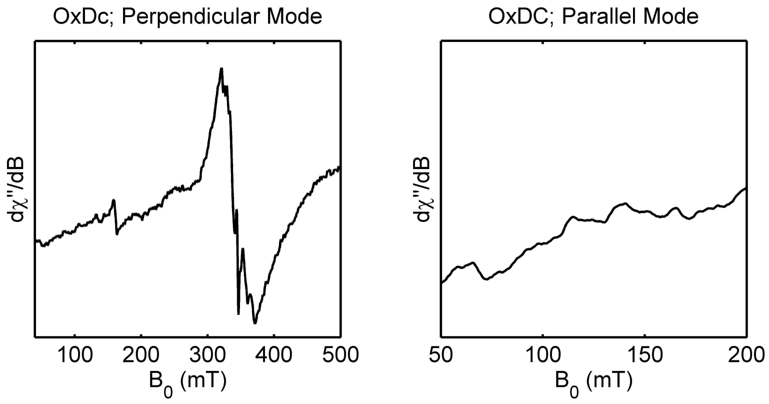

Figure 3.15. Perpendicular (left) and Parallel (right) mode EPR spectra of 500 μM WT OxDC and 100 mM oxalate after mixing, frozen after 10 ms. Figure was prepared by Dr. J. Wilcoxen.

These parallel mode EPR observations raise two questions concerning (i) which of the two bound Mn ions is oxidized, and (ii) the mechanism by which O_2 oxidizes Mn(II) to Mn(III). It is very likely that the Mn(III) signal is associated with the metal center in the N-terminal domain of the enzyme. It was demonstrated in an earlier pH-dependent HFEPR study of WT OxDC that the signal from the N-terminal metal binding site is more sensitive to changes in buffer pH, [49] presumably because it is more accessible to solvent. [46] This increased accessibility is likely due to a mobile loop in the N-terminal domain that can adopt open or closed conformations. [45] Of course, given the high concentration of oxalate needed to observe the Mn(III) signal, the possibility that substrate can access the C-terminal Mn-binding site under these conditions cannot be unequivocally ruled out. [61] [45]

Given the requirement of O_2 for the catalytic activity of OxDC, [43] [50] and a recent observation that superoxide radicals are formed when OxDC is undergoing turnover, [63] it seems reasonable to propose that O_2 mediates metal oxidation. In addition, a previous parallel mode EPR study on a synthetic monomeric Mn complex, which exhibited very similar spectroscopic properties to those observed in the OxDC system, suggested that formation of a hydroperoxo-Mn(III) [95] complex involved the initial formation of a superoxo-Mn(III) intermediate. [46] The fact that oxalate is required for the formation of Mn(III) is intriguing given that proteins are able to adjust the redox potential of Mn(II) so that it can be oxidized by O_2. [52] A similar proposal has been made for the Mn-dependent dioxygenase present in *Arthrobacter globiformis*, which binds a deprotonated catechol substrate prior to oxidation by O_2. [96] Given that work using nitric oxide (NO) as a O_2 mimic suggests NO does not bind to the Mn(II) centers of free WT OxDC, [54] it is possible that oxalate binding is required before O_2 is able to coordinate the active site metal and give rise to Mn(III). A Mn(III)-superoxide intermediate could then function as an electron sink to form the Mn-bound oxalate radical needed to lower the barrier to heterolytic cleavage of the C-C bond. [25] On the other hand, because the Fe-substituted variant of OxDC shows no catalytic activity, it seems unlikely that electron transfer operates by the same mechanism as proposed for the Mn-dependent aromatic ring-cleaving dioxygenases. [97] Indeed, evidence has been reported to suggest electron transfer from the substrate is gated by proton removal from oxalate. [51] Unlike many redox Mn enzymes that adapt multinuclear metal center and process redox catalysis, [98] the redox cycle in OxDC is the first example of hexa-coordinated monomanganese-dependent enzyme that is able to mediate the redox of Mn(II)/Mn(III) in a non-redox reaction by utilizing O_2 as a cofactor.

3.3 Conclusion

Based on the proposed mechanism of OxDC (Fig. 1.5), oxalate binding is required before O_2 is able to coordinate the active site metal and give rise to Mn(III). Although the enzyme is exposed to an aerobic environment, Mn(III) has not been found in the free enzyme. Binding of O_2 would give rise to superoxide bound Mn(III), which can function as an electron sink. After removal of an electron from Mn-bound substrate in a process is coupled by proton transfer, decarboxylation yields a formyl radical and finally accepts a proton and an electron to form formate. Dissociation of O_2 restores the enzyme to its resting state. Although there are still missing pieces in this mechanism puzzle that remain, such as spectroscopic evidence of for O_2 binding to the enzyme/oxalate complex, these studies provide the first evidence that substrate binding under optimum conditions for catalysis gives rise to higher Mn oxidation states. Moreover, the identification of conditions for observing OxDC-bound Mn(III) by parallel mode EPR should permit a systematic investigation of how protein residues facilitate the control of metal redox potential. Thus, OxDC, as a unique mononuclear Mn center protein using O_2 as catalyst, joins a growing list of enzymes capable of stabilizing and controlling the reactivity of Mn(III), a powerful oxidant in aqueous solution.

3.4 Experimental Section

Unless stated otherwise, all chemicals and reagents were purchased from Fisher (Pittsburgh, PA) or Sigma-Aldrich (St. Louis, MO). $^{13}C_2$-oxalic acid (99%) was purchased from Cambridge Isotope Laboratories (Andover, MA). Plasmid miniprep kits were purchased from Zymo Research (Irvine, CA). BT Chelex 100 resin was purchased from Bio-Rad (Hercules, CA). ICP-MS measurements of metal content were carried out at the Center for Applied Isotope Studies at the University of Georgia (Athens, GA). The plasmid containing the gene encoding N-terminal His_{x6}-tagged *Bs*OxDC was generously provided by Dr. Stephen Bornemann (John Innes Center, Norwich, UK).

3.4.1 Protein Expression and Purification

A plasmid vector, pET-32a, containing N-terminal His_6-tagged *B. subtilis* OxDC, was transformed into BL21(DE3) for overexpression using previously established methods. [99] The cell culture was heat-shocked at 42 °C for 18 min after OD_{600} had reached 0.5, following by addition of 5 mM $MnCl_2$ and 0.8 mM Isopropyl β-D-1-thiogalactopyranoside (IPTG) to induce overexpression of the protein. Cells were harvested by centrifugation and lysed by sonication in lysis buffer (50 mM Tris-HCl, pH 7.5, 500 mM NaCl, 10 μM $MnCl_2$, 10mM imidazole and 20% glycerol). Cell debris was removed by centrifugation and the soluble protein in the supernatant was purified through a Ni-NTA affinity column. The elution fractions were pooled and dialysis against storage buffer (50 mM Tris-HCl, pH 8.5, 500 mM NaCl and 20% glycerol) to remove the imidazole. Protein was concentrated to the desired concentration using Amicon Ultra-30K centrifugal filter units from Millipore (Billerica, MA) and treated with Bio-Rad Chelex-100 resin (Hercules, CA) to remove the free metal in the solution. Protein concentrations were determined using Bradford assay, using bovine serum albumin as the standard. The metal incorporation of the WT OxDC was quantified using the ICP-MS service at the Chemical Analysis Laboratory of University of Georgia (Athens, GA). The molecular weight of the protein was confirmed by sodium dodecyl sulfate-polyacrylamide gel electrophoresis (SDS-PAGE). The protein concentraion was determined using Bradford assay. [100]

3.4.2 MIMS Assay

The steady-state kinetic assay was initiated by addition of 0.07 μM enzyme into the reaction mixture (60 mM potassium acetate, pH 4.2, 0.2% Triton-X, 200 mM sodium chloride and 0-50mM ^{13}C-oxalate, pH 4.2). The signal m/z 45 was monitored by GC-MS (GE). The initial $^{13}CO_2$ production rate was calculated from the first 20 sec of the reaction, and the concentration of the $^{13}CO_2$ was obtained from the ion current by means of a CO_2 standard curve. The standard curve was achieved by adding aliquots of K_2CO_3 solution with known concentration into 200 mM acetate buffer, pH 2.0. The ion current at m/z 44 represents the concentration of CO_2 in the solution. The reaction chamber was washed with a solution of 2.5 M potassium hydroxide with

2.5 M ethylenediaminetetraacetic acid (EDTA) then rinsed with deionized water after each use. Measurements were made at specific substrate and enzyme concentrations in triplicate, and the data analyzed to obtain the values of V and V/K by standard computer-based methods.

3.4.3 FDH Assay

Reactions were initiated in the mixtures (50 mM acetate buffer, pH 4.2, 125 mM NaCl, 300 μM *o*-phenylenediamine (*o*-PDA) and 0-80 mM oxalate) by addition of enzyme at 25 °C. Reactions were quenched by addition of 100 mM sodium hydroxide after 1 min. The amount of formate produced was determined by a coupled assay, in which the production of formate was quantified by the conversion of NAD^+ to NADH by formate dehydrogenase in 50 mM phosphate buffer, pH 7.8 with 1.5 mM NAD^+ and 0.5 UFDH. The amount of NADH was measured at 340 nm using UV-Vis spectroscopy after 16 h incubation at 37°C. The V_{max} of the enzyme in the presence of 30% glycerol was determined under the same condition with the oxalate-containing EPR experiments using the FDH assay. The reaction was initiated by addition of 0.5 mM enzyme into oxalate containing buffer (100 mM oxalate, 100 mM sodium citrate, 50 mM Bis-Tris and 30% glycerol). The reaction mixture was mixed by pipetting up and down for 15 s, following by addition of sodium hydroxide to quench the reaction. The formate produced was quantified as described above.

3.4.4 EPR Experiments

Samples used for EPR analysis were incubated with Chelex resin for 2hrs on ice to remove free metal ions before being concentrated to approx. 590 mM using an Amicon Ultra-15 Centrifugal Filter Unit (30K) from Millipore (Billerica, MA). Protein concentrations were determined using the Bradford assay (Pierce, Rockford, IL). EPR measurements of the enzyme samples were performed in poly-buffer (100mM sodium citrate, 50 mM Bis-Tris and 25 mM Tris-HCl, containing 250 mM KCl and 30\{}%

glycerol) in samples adjusted to pH 8.5, pH 5.7 and pH 4.2. For oxalate-containing samples, 200 mM potassium oxalate was added at each solution pH, and the resulting solutions mixed in the EPR tube at room temperature to initiate the reaction. After 15 s, each sample was fast-frozen in an acetone/dry ice slush and stored in liq. N2. The final concentration of oxalate in each sample was 100 mM. The extended reaction sample was prepared as the 15 s reaction set except that the reaction was allowed to take place for 5 min. For the rapid-freeze quench study, the enzyme (500 ± 70 μM final concentration) and substrate (100 mM final concentration) were mixed in poly-buffer, pH 4.2, containing 50% glycerol for 10 ms before being rapidly frozen.

Samples for X-band (9.4 GHz) EPR spectroscopy were measured at the CalEPR center at the University of California, Davis. Continuous wave (CW) spectra were collected using a Brker Instruments EleXsys-II E500 CW EPR spectrometer (Brker, Billerica, MA) equipped with an Oxford Instruments ESR900 liquid helium cryostat and Oxford Instruments ITC503 temperature and gas-flow controller. Samples were measured under non-saturating slow-passage conditions using a Super-High Q resonator (ER 4122SHQE) or Dual Mode resonator (ER 4116DM), specific parameters for microwave frequencies, modulation amplitude and temperature are included in figure legends.

4. CHARACTERIZATION OF THE N-TERMINAL ACTIVE SITE LOOP VARIANTS OF OXDC

4.1 Introduction

The loop region of OxDC has been identified as being crucial for OxDC activity of the enzyme. Mutagenesis studies were therefore performed on this SENS loop in the N-terminal domain of the enzyme. (Table 4.1.)

Glu162 is highly conserved across different species, and mutations at this position lead to reduced activity. [45] Investigations based on the sequence alignment of OxDC and OxOx and site-directed mutagenesis studies indicated that converting the SENS loop residues of OxDC to the corresponding residues in OxOx yields a OxDC/OxOx chimera that exhibits low OxDC activity and increased OxOx activity. [56] Thus, when the N-terminal loop segment, SENS, in OxDC was replaced by DSSN or DASN, the decarboxylase activity of these variants was almost low and oxidase activity was increased relative to that of wild type OxDC. Interestingly, the SENST161-5DASNQ variant, given species OxDC was modified to mimic the corresponding loop in *Cs*OxOx, exhibited no significant increase in OxOx activity. [68] This suggests that the basis for this activity switch in the chimeric variants is not simply due to mimicking of the loop region. A deeper investigation of the loop variants was required to understand the functional role of these residues in the catalytic mechanism of OxDC.

Since many of the OxDC variants reported previously were prepared using different protocols, and a variety of assay conditions were used, any comparison of OxDC activity and OxOx activity between different variants was in valid. A more systematic

Table 4.1.
Summary of mutagenesis studies on the OxDC loop region.

OxDC variant	OxDC activity K_M (mM)	OxDC activity V_{max} (U/mg)	OxOx activity V_{max} (U/mg)	Reference
S161A	71	14	<0.01	[40]
E162A	-	0	0.04	[39]
E162Q	14	0.2	0.03	[39]
E162D	17	28	0.02	[40]
Δ162-163	2	0.2	0.08	[40]
Δ162-164	-	0	0.12	[40]
S164A	31	14	<0.01	[40]
SE161-2DA	9	0.4	0.4	[50]
SEN161-3DAS	n.d.	<0.01	1.1	[50]
ENS162-164ASN	2	0.5	1.3	[50]
S161D/NS163SN	97	37	0.1	[50]
SENS161-4DASN	n.d.	0.05	4.5	[50]
SENST161-DASNQ	n.d.	0.01	0.2	[50]
SENS161-4DSSN	n.d.	0.04	4.4	[50]

$^{\text{n.d.}}$ not determined

examination of the multi-site variants was therefore performed to define the functional role of each residue in the SENS loop. The DASN variant, which exhibits the highest OxOx activity and decreased OxDC activity, was chosen as a model, and several new single-site or multi-site mutations were expressed and purified.

The goal of the research discussed in this chapter is to understand the functional role of the loop residues in OxDC and their contribution to catalysis using MIMS, X-band EPR, spin-trap experiments, KIE measurements and X-ray crystallography.

4.2 Results and Discussion

4.2.1 Expression and Purification of the Loop Variants

A series of loop variants, SENS161-4DASN (DASN), S161D/NS163-4SN (DESN), SENS161-4DDSN (DDSN), SE161-2DD (DDNS), S161D (DENS), S161A (AENS) and deletion of E162 (ΔE162) were expressed and purified using standard protocols. The expression yield (>20 mg/L culture) were not affected by the site of mutations. The metal contents of these variants were all greater than 1.3 Mn per monomer, suggesting that these mutations have no effect on metal loading at both the N-terminal and C-terminal binding sites. The ΔE162 variant had the lowest metal content, at 1.3 atom manganese per monomer. Other single-site mutations at residue 162, such as E162A, E162Q, and E162D exhibited completely different effects on metal binding. [46] [48] Although Glu162 is not directly coordinated with the N-terminal manganese ion, the residues at this position did influence whether manganese was properly loaded to the metal binding site. [55] It is believed that the charge of residues in the site affects metal loading during protein folding.

4.2.2 Determine Steady-state Kinetic Parameters Using Standard Assays

Steady-state kinetic parameters were obtained using standard coupled assays measuring formate production for OxDC activity (Table 4.2.) and H_2O_2 production for

OxOx activity. (Table 4.3.) The OxDC and OxOx activities reported here were corrected for the metal content of each variant. A more valid activity switch shown in the table was calculated from the ratios of OxOx and OxDC activities (k_{cat}/K_M/Mn) between a loop variant and WT enzyme.

The DASN variant exhibited increased OxOx activity with low OxDC activity, which was consistent with the result of previous study. [56] Restoration of glutamate to postition 162, ie. DESN, resulted in recovery of OxDC activity. In order to compare the contribution of Glu162 to the specificity switch, loop variants were grouped into four sets based on the residues adjacent to residue 162. (Table 4.4) The DASN, DDSN, and DESN variants (Group I) have the same residues at positions 161, 163 and 164. Similarly, the variants DANS, DDNS, and DENS are grouped as Group II, while the SENS (WT OxDC), SANS, SDNS and ΔE162 variants are Group III. Group IV comprises the SENS, DENS, and the AENS variants, in which residue 161 is varied.

Substitution of Glu162

OxDC activity In Group I, in which the residue at position 162 is varied, the DASN variant had the lowest OxDC activity at less than 0.5% of that determined for the DESN and DDSN variants. The OxDC activity of the DDSN variant was approximately 2-fold less than that of the DESN variant. This can be rationalized by aspartate having the same carboxylate group as glutamate. Therefore, in the same background of oxidase loop residues (Asp161-Ser163-Asn164), decarboxylation. The same pattern was found in Group II, which contains the DDNS, DANS and DENS variants. The DANS variant had approximately 0.5% OxDC activity of the DENS variant. The OxDC activity of the DDNS variant was approximately 1.3-fold less than that of the DENS variant. In Group III, for which all the mutations have the same residue at positions 161, 163 and 164 as in WT OxDC, the SANS variant lost all OxDC activity, and the SDNS variant had approximately 40% specific activity.

Table 4.2.
Steady-state kinetic parameters of decarboxylase activity for WT and the loop variants determined by FDH assay.

	V_{max} (U/mg)	K_M (mM)	k_{cat} (s^{-1})	k_{cat}/K_M/Mn ($M^{-1}s^{-1}$)	Mncontent (Mn/monomer)
SENS (WT)	82 ± 3	8 ± 1	60 ± 2	5670 ± 840	1.4
DASN	0.6 ± 0.1	16 ± 7	0.4 ± 0.1	17 ± 8	1.6
DESN	54 ± 2	6 ± 0.8	40 ± 1	4370 ± 660	1.5
DDSN	13 ± 3	3 ± 0.7	10 ± 2	2400 ± 910	1.5
DDNS	61 ± 4	10 ± 2	45 ± 3	2940 ± 680	1.5
DENS	86 ± 3	10 ± 1	63 ± 3	3870 ± 460	1.6
AENS	83 ± 5	9 ± 1	61 ± 4	4820 ± 860	1.4
ΔE162	0.01 ± 0.007	1.6 ± 0.7	0.01 ± 0.005	5 ± 2	1.3
SANS[b]	0	[a]	[a]	[a]	1.4
SDNS[b]	40 ± 3	3.1 ± 0.7	29 ± 2[b]	9000	1.1
DANS[b]	0.36 ± 0.01	9.1 ± 1.1	0.26 ± 0.01	24 ± 3	1.2

[a] not applicable.

[b] adapted and re-analyzed from [39], [42] and [50].

Table 4.3.
Steady-state kinetic parameters of oxidase activity for WT and the loop variants determined by ABTS assay.

	V_{max} (U/mg)	K_M (mM)	k_{cat} (s^{-1})	k_{cat}/K_M/Mn ($M^{-1}s^{-1}$)	Specificityswitch
SENS (WT)	0.18 ± 0.03	5 ± 0.2	0.13 ± 0.02	19 ± 3	1
DASN	5.6 ± 0.5	3.0 ± 0.3	4.1 ± 0.4	850 ± 190	14913
DESN	0.14 ± 0.01	11 ± 2	0.10 ± 0.01	11 ± 1	1
DDSN	1.07 ± 0.04	17 ± 2	0.79 ± 0.03	32 ± 4	4
DDNS	0.67 ± 0.05	16 ± 2	0.49 ± 0.04	20 ± 3	2
DENS	0.07 ± 0.01	4 ± 0.4	0.05 ± 0.01	9 ± 2	1
AENS	0.02	[b]	[b]	[b]	[b]
ΔE162	0.06 ± 0.04	3 ± 1	0.05 ± 0.03	14 ± 9	835
SANS[c]	0.02	[b]	[b]	[b]	[b]
SDNS[c]	[b]	[b]	[b]	[b]	[b]
DANS[c]	0.36 ± 0.01	0.31 ± 0.04	0.26 ± 0.01	800 ± 100	9947

[a] specificity switch was defined as the ratios of OxOx to OxDC activities (k_{cat}/K_M) between a mutant and wild type.

[b] not applicable

[c] adapted and re-analyzed from [39],[42] and [50].

Table 4.4.
Groups of the loop variants of OxDC.

	Group I	Group II	Group III	Group IV
1	DASN	DANS	SENS	SENS
2	DDSN	DDNS	SANS	AENS
3	DESN	DENS	SDNS	DENS
4			ΔE162	

Overall, based on comparison of these three groups of variants, regardless of whether residues 161, 163 and 164 are those found in OxDC or the same as in OxOx, glutamate at position 162 is necessary for maintaining OxDC activity. Aspartate also has ability to maintain decarboxylase activity, and substitution of alanine at position 162 low OxDC activity in all three groups. An extreme case is represented in the deletion mutant in Group III, ΔE162, which exhibited very low OxDC activity. These findings confirm that residue 162 must be negatively charged to maintain OxDC activity and the length of the side chain also affects OxDC activity.

OxOx activity In Group I, when Glu162 was substituted by alanine, OxOx activity was increased. The OxOx activity of the DANS variant was the highest among all the variants in this study, being 77-fold higher than that of the DESN variant in Group I. Similarly, the DASN variant exhibited the highest OxOx activity among all three variants in Group III. Substitution of aspartate at the residue 162 also supported OxOx activity, although at a considerably lower extent than when alanine was present at this position. A 2.2-fold increase of OxOx activity in the DDNS/DENS pair in Group I and 3-fold in the DDSN/DESN pair in Group II was observed when the glutamate was replaced by aspartate. When Glu162 was deleted, OxOx activity did not increase in the absence of this residue. Together, these results confirm that Glu162 is crucial for maintaining decarboxylase activity, but it is not the only factor underlying increased OxOx activity in the chimeric loop variants.

Switching Residues 163 and 164

OxDC activity Comparing of the loop variants in Group I with those in Group II indicates that OxDC activity is slightly more favorable with the combination of Asn163 and Ser164 when residues 161 and 162 are the same as those in WT OxDC. However, when residue 162 is mutated to alanine or aspartate, this advantage disappeares. The difference between the DDSN and DDNS variants or the DASN and DANS variants is very small.

OxOx activity Although the OxOx activity of variants in Group I and Group II was essentially altered when residues 161 and 162 in Group I were the same as those in Group II, all variants in Group I have slightly higher OxOx activity. Such an insignificant difference suggests that the activity switch of the DASN variant is not due mainly to the altering residues 163 and 164.

Substitution of Ser161

OxDC activity It was previously reported that the AENS variant was essantially an inactive enzyme with almost no OxDC activity and only slightly increased OxOx activity. [46] The crystal structure of the AENS variant showed a different conformation of the loop to the "open" and "closed" conformation of the SENS loop previously seen in X-ray crystal structure [46]. The reduction in low OxDC activity caused this mutation was rationalized by the abnormal movement of the N-terminal loop. [46] However, a significant increase for K_M and the absence of metal content information raised the question of whether metal was incorporated properly in this variant, and this variant was re-investigated in our laboratory using standard protocols. The metal content and OxDC activity of the AENS variant expressed by us were identical to those of WT OxDC, and the DENS variant exhibited a greater effect on OxDC activity than the AESN variants. Since the DENS variant did not have increased OxOx activity, residue 161 appears to have only a minor effect on loop function in OxDC. The altered loop conformation in the crystal structure of AENS is very likely due to crystallization conditions. What is worth noting here is that all crystals of *Bs*OxDC have been were grown under basic conditions, between pH 7.5-pH 9.0. [44] [99] At this solution pH, the protonation state of the enzyme and substrate binding mode may be different to that at pH 4.2; the optimal conditions for enzyme activity. It is likely that the AESN variant catalyzes decarboxylation using the same catalytic mechanism as WT OxDC.

OxOx activity Substitution of alanine or aspartate at position 161 did not increase OxOx activity when residues 162, 163 and 164 were the same as in WT OxDC. The mutation at position 161 is therefore not responsible for increased OxOx activity in the chimeric DASN variant. This may also mean that the crystal structure of the AENS variant could be just a snapshot of the loop in basic conditions and true catalytic conformation.

Thus, the role of each residue in the N-terminal SENS loop, especially Glu162, can be summarized as follows. In all the variants with a carboxylate group in the side chain of residue 162, mutations of the three other loop residues had limited effect on both OxDC activity and OxOx activity. When the carboxylate group is at a different distance from the substrate, such as in the DDSN and DDNS variants, OxDC activity was decreased with no significant increase in OxOx activity. Removal of the carboxylate group at position 162, as in the case of the DASN and ΔE162 variants, significantly lowered OxDC activity, but did not necessarily increase OxOx activity in thr chimeric enzyme. This is understandable from an evolutionary standpoint. Assuming that OxDC and OxOx share a common ancestor, the catalytic specificity switch results not from mutation of single residue, but from cooperative changes in a series of amino acids. It would also br unfavorable for an organism if a single mutation led to change in reaction specificity of a given enzyme.

Why does this particular combination of four residues have the ability to switch the specific activity of enzyme, even though the contribution of individual residue to the switch is very limited? In order to address this question, the DASN variant was used as a model for further studies. Due to limitations of standard kinetic assays, MIMS was utilized for these experiment on the DASN variant.

4.2.3 MIMS Experiments

Kinetic Parameters Determination

MIMS was employed in comparing OxDC and OxOx activities because of its ability to measure CO_2 consumption and O_2 production simutaneously in real-time. (Table 4.5) In order to eliminate any influence of dissolved CO_2 in the enzyme solutions, which would affect accurate calculation of the CO_2 concentration, 1, 2-$^{13}C_2$-oxalic acid was used as the substrate. In the measurements, the signal at m/z 45 measured production of $^{13}CO_2$ from the enzymatic reaction, and the signal at m/z 32 was recorded to determine the O_2 consumption. Based on the stoichiometry of the OxOx-catalyzed reaction, the ratio of H_2O_2 production and O_2 consumption is 1, and the ratio of CO_2 production and O_2 consumption is 2. Because O_2 was only consumed in the oxidase reaction, kinetic parameters calculated from O_2 consumption indicate OxOx activity. (Fig. 4.1)

The V_{max} of the DASN variant was 4.6 ± 0.6 U/mg, which was calculated from O_2 consumption based on MIMS measurements. This value is comparable with that obtained from the peroxidase-ABTS assay (5.6 ± 0.5 U/mg). The production of formate in MIMS assay solution was measured as follows. reactions were quenched by addition of 30 μL 6 M KOH to adjust the pH of the reaction mixture to pH 12. At this pH, the decarboxylation does not occur. The quenched solution was lyophilized overnight and dissolved in phosphate buffer for use in a standard FDH assay (Fig. 4.1). The CO_2 produced by the DASN variant arises from both OxDC and OxOx activity. According to the stoichiometry of the two reactions, the calculated V_{max}

Table 4.5.
Kinetic parameters determined by MIMS and the comparison with the standard assays.

	MIMS	MIMS	MIMS	FDH	ABTS
	Enzyme activity	OxDC activity	OxOx activity	OxDC activity	OxOx activity
	based on total CO_2	based on CO_2 and O_2	based on O_2	based on formate	based on H_2O_2
K_M (mM)	1.5 ± 0.2	2.5 ± 0.6	0.7 ± 0.1	3 ± 1	3 ± 0.3
V_{max} (U/mg)	12.5 ± 0.3	3.2 ± 0.2	4.6 ± 0.6	1.3 ± 0.1	5.6 ± 0.5

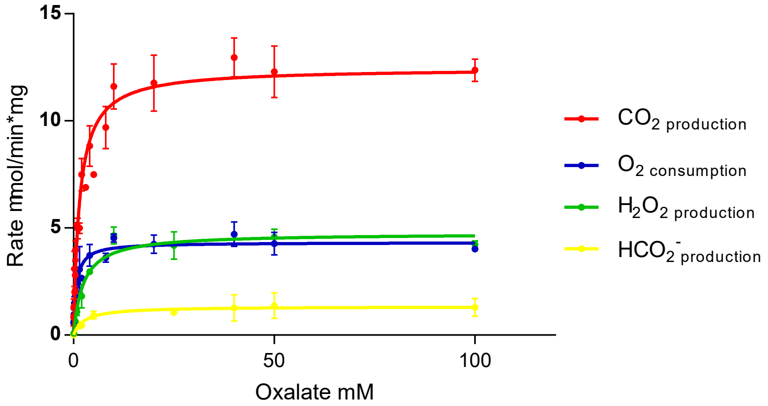

Figure 4.1. The Michaelis-Menten curve of the DASN variant measured by MIMS and the comparison with the standard assays.

of CO_2 based on the production of formate (1.3 ± 0.1 U/mg) and H_2O_2 (5.6 ± 0.5 U/mg) was 12.4 U/mg, which matched the production of CO_2 obtained by MIMS measurement (12.5 ± 0.3 U/mg). This confirmed that MIMS measured both OxDC and OxOx activities in the OxDC chimeric variants.

Ratio of Carbon Dioxide Production and Dioxygen Consumption at Different Oxalate Concentrations

Since MIMS provides an efficient way to determine simultaneously the OxDC and OxOx activities, direct comparison is more reliable than by performing separate measurements. The ratio of OxDC activity to OxOx activity was calculated from the stoichiometry of these two reactions and the ratio of the CO_2 production and the O_2 consumption. Interestingly, the ratio of OxDC activity and OxOx activity was not a constant for the DASN variant (Fig. 4.2). More specifically, with low concentration of oxalate, the ratio of CO_2 production and O_2 consumption was approximately 2. However, when substrate concentration increased, this ratio approached 3. Therefore, for the DASN variant, the ratio of OxDC activity and OxOx activity is dependent

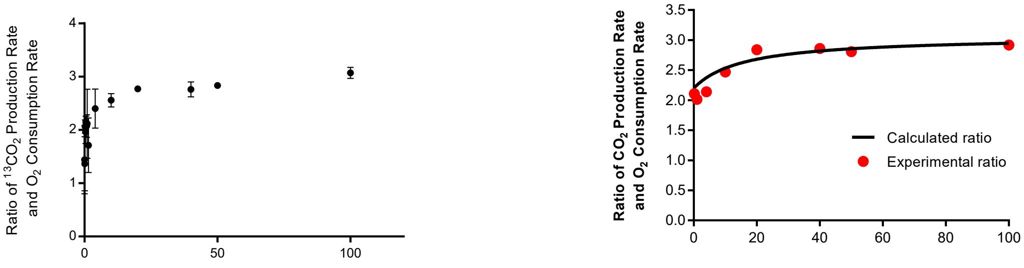

ratio.pdf

(a) Experimental ratio

(b) Calculate ratio

Figure 4.2. The ratio of CO_2 production rate and O_2 consumption rate at different concentrations of oxalate.

on the concentration of the substrate. Assuming that only one metal binding site in OxDC is active and the ratio of enzyme performing decarboxylase activity to oxidase activity is a constant, the calculated ratio based on the steady-state parameter obtained from the Table 4.2 and Table 4.3 for the DASN variant matches with the experimental data. This suggests that the previous assumptions represent the real scenario in this enzyme during the turnover. The calculated ratio of the amount of the enzyme performing decarboxylase reaction to the enzyme performing oxidase reaction is about 12 to 1. This suggest that the DASN variant is still a better decarboxylase than a oxidase. Therefore, the oxidase activity in the DASN variant could just be a side reaction caused by the impaired N-terminal loop in the enzyme.

Dioxygen Dependence of the DASN Variant

The solubility of O_2 at a given pressure and temperature is constant. Reaction mixtures with varied concentrations of O_2 were obtained by adjusting the ratio of O_2-saturated and helium-saturated buffers before initiation of reactions by the addition of the DASN variant. The m/z 45 signal showed the production of $^{13}CO_2$ from the

^{13}C labeled oxalate, and the m/z 32 signal gave the change in O_2 concentration during the reaction.

There was no significant increase of the m/z 45 signal when the DASN variant was added to helium-saturated buffer confirming that the DASN variant needs O_2 to maintain both OxDC and OxOx activities. Results that had been published [56] on the O_2-dependence of the DASN variant could be reproduced (Fig. 4.3).

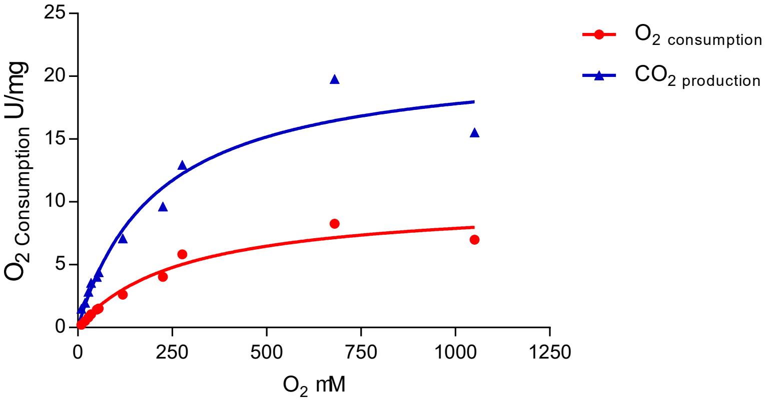

Figure 4.3. The production of CO_2 and the consumption of O_2 of the DASN variant are dependent on the O_2 concentration. The plots were fitted to Michaelis-Menten equation.

Briefly, the rate of O_2 consumption was measured in buffer containing 100 mM oxalate at different initial O_2 concentrations. K_M and V_{max} values determined by MIMS were 260 ± 20 mM and 9 ± 2 U/mg, respectively, which is comparable to the values ($K_M = 168 \pm 14$ μM, and $V_{max} = 5.25 \pm 0.15$ U/mg) determined using an oxygen electrode. [56] Because MIMS is able to measure the production of CO_2 and the consumption of O_2 simultaneously, it was possible to observe the increased rate of CO_2 production as the O_2 concentration in the reaction mixture was increased at a fixed oxalate concentration (Fig.4.4). However, at high O_2 concentrations, both O_2 consumption and CO_2 production were inhibited (Fig. 4.4).

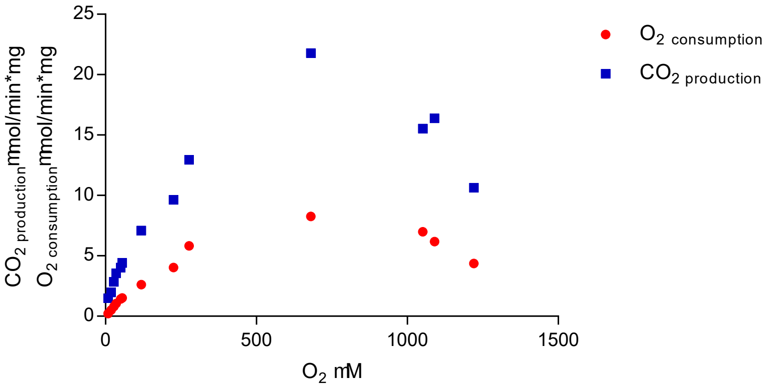

Figure 4.4. The O_2-dependence of the DASN variant.

Ratio of Carbon Dioxide Production and Dioxygen Consumption at different Dioxygen Concentrations

By comparing the ratio of CO_2 production rate and O_2 consumption rate at different concentrations of O_2, the ratio of the OxDC and OxOx activity was estimated (Fig. 4.5). This ratio was not a constant. In low O_2 conditions, the majority of CO_2 production arose from the decarboxylation reaction. As the O_2 concentration was increased, more CO_2 was produced from the oxidation of oxalate, and the ratio was approximately 3 when the O_2 concentration was above 40 μM.

In order to compare the relative OxDC and OxOx activities of the DASN variant, four points (Fig. 4.4)were taken and analyzed (Table 4.6). In the proposed OxDC mechanism, one O_2 molecule is able to facilitate the decarboxylation of oxalate. Thus, 10-fold higher O_2 concentrations compared to enzyme should be enough for the enzyme to catalyze the OxDC reaction. Given that low oxygen concentrations do not favor OxOx activity, assuming that OxDC activity is not significantly affected by altering O_2 concentrations in the low O_2 containing buffer at the fixed oxalate concentration is fixed, doubling the O_2 concentration gave to an approximately 2-fold

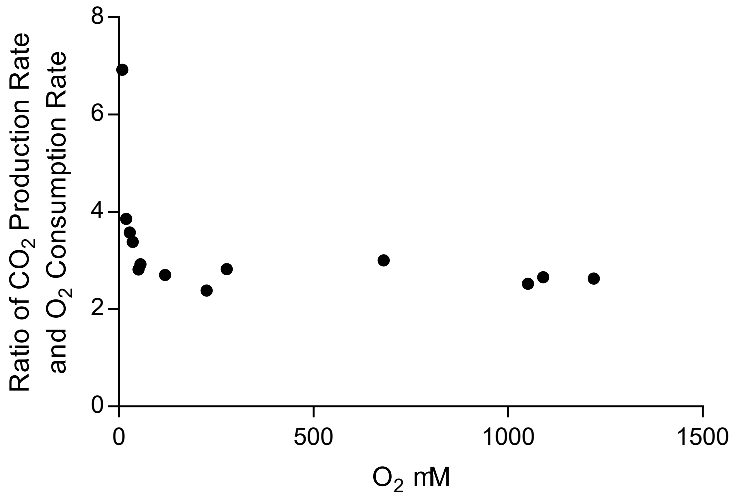

Figure 4.5. The ratio of CO_2 production rate and O_2 consumption rate at different concentrations of O_2.

Table 4.6.
Ratio of OxDC activity and OxOx activity in the DASN variant at different O_2 concentrations.

$[O_2]$ (μM)	Rate_{CO_2} : Rate_{O_2}	$\text{Activity}_{\text{OxDC}}$: $\text{Activity}_{\text{OxOx}}$
9	6:1	4:1
20	4:1	4:2
40	3:1	4:4
680	3:1	4:4

increase in OxOx activity at low O_2 concentration. This linear increase ceased when O_2 concentration was 40 μM.

Although O_2-induced inhibition at 1280 μM O_2 condition did not affect the ratio of OxDC and OxOx activities, the consumption rate of O_2 and the production rate of CO_2 were both lower than that seen at 680 μM O_2 concentration. This suggests that both the OxDC and OxOx activities were affected simultaneously by excess O_2 in the buffer. A simple explanation for this observation is that O_2 inhibits the enzyme by affecting the shared steps of OxDC and OxOx activities prior to the first decarboxylation, assuming that the two reactions are catalyzed at the same metal binding site. According to the hypothetical mechanism, [56] OxDC and OxOx share the initial steps with the branch point in this mechanism being formation of a formyl radical anion intermediate. Therefore, it is possible that O_2 interacts with the enzyme-substrate complex after oxalate is binding. If this is the case, the binding pocket for excess O_2 could be in the N-terminal or the C-terminal domain. However, based on the proposed mechanism, it is unlikely that excess O_2 interferes with the N-terminal metal when both O_2 and oxalate occupy two ligand positions at manganese. Thus, the C-terminal is proposed here as a potential binding pocket for additional oxygen. When the O_2 concentration was less than 685 μM, the ratio of OxDC activity and OxOx activity was not affected by O_2 concentration. At higher concentrations of O_2, the DASN variant is inhibited in a noncompetitive fashion.

O_2 inhibition of the DASN variant was not reported previously because MIMS is able to measure kinetic data at higher O_2 concentrations than the Clark dioxygen sensor. [56] Because the CO_2 measurements obtained by MIMS reflect the sum of OxDC activity and OxOx activity, and assuming that the O_2 concentration does not affect the ratio of OxDC to OxOx activity in the DASN variant (1:1 at higher oxalate concentrations), the calculated V_{max} for O_2 consumption is 9 U/mg. This is comparable with the value measured using the Clark oxygen sensor, [56] and the same as the value calculated from O_2 consumption. Therefore, any difference between the results of the previous study and the work demonstrated here is not due to instrument error or the method of measurement.

Dioxygen Inhibition

A series of O_2-dependence measurements was performed at varying oxalate concentrations to investigate O_2 inhibition of the DASN variant. Similar inhibitory effects were observed at different oxalate concentrations (Fig. 4.6). Fitting to equation (4.1) gave an approximate K_I value of 240 μM.

$$V = \frac{V_{max} * A}{K_M + A * (1 + \frac{A}{K_I})} \tag{4.1}$$

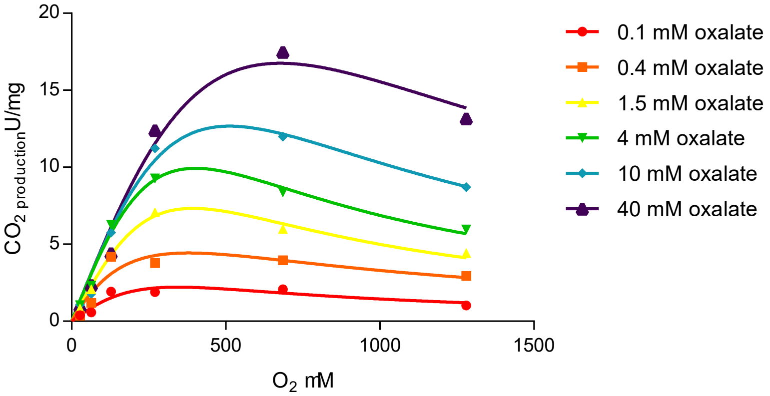

Figure 4.6. The Michaelis-Menten curve of the DASN variant based on the production of CO_2 in varying concentrations of oxalate.

Using a double reciprocal plots (Fig. 4.7) of O_2 inhibition versus oxalate allowed data set (Fig. 4.7) to be fitted linearly. Then calculated intercepts and slopes were then re-plotted against the reciprocal of the concentration of O_2 (Fig. 4.8). Substrate inhibition by O_2 versus oxalate affected on both the slope and intercept, indicating the inhibition by O_2 to be noncompetitive versus oxalate.

Steady-state kinetic parameters based on total CO_2 production were measured in reaction mixtures containing 27 μM, 64 μM, 128 μM, 270 μM, 685 μM and 1280 μM O_2. (Fig.9) The K_M value for oxalate increased at higher O_2 concentrations and

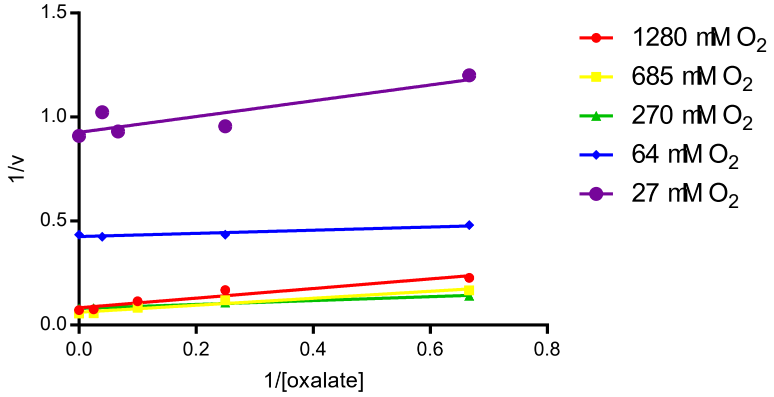

Figure 4.7. The double reciprocal plot of O_2 inhibition versus oxalate.

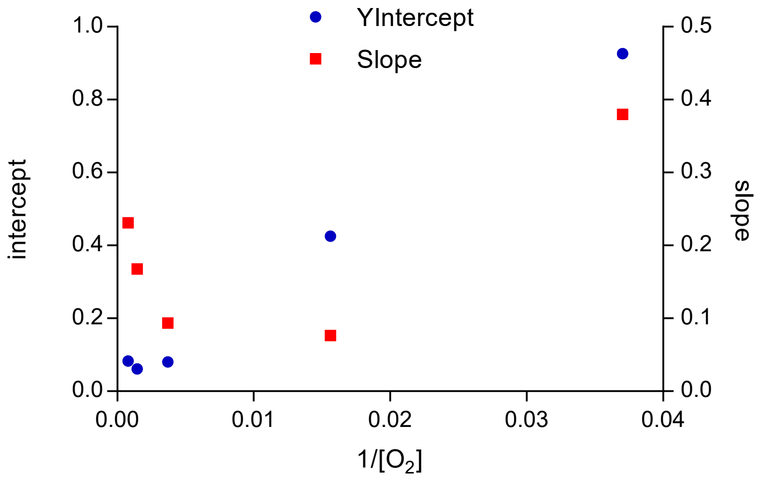

Figure 4.8. Re-plot of the slopes and intercepts of the double reciprocal plot with the reciprocal of the O_2 concentrations.

the V_{max} decreased when O_2 concentration reached 1280 μM. (Table 4.7) The highest k_{cat}/K_M/Mn for the DASN variant was observed in the presence of 27 μM O_2.

Another observation from the O_2-dependence study of the DASN variant was that the lifetime of the enzyme was affected by O_2 concentration (Fig. 4.10). Following initiation of the reaction by addition of the DASN variant into 40 mM oxalate, the

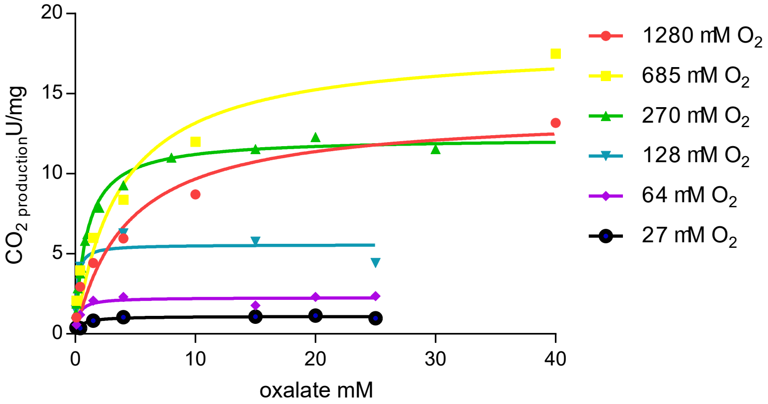

Figure 4.9. The Michaelis-Menten curve of the DASN variant based on the production of CO_2 in varying concentrations of O_2

Table 4.7.
The steady-state kinetic parameters based on the total CO_2 production were measured in the reaction mixture containing various concentrations of O_2

$[O_2]$ (μM)	1280	685	270	128	64	27
K_M (mM)	4.3 ± 1.6	3.7 ± 1.4	1.5 ± 0.2	0.2 ± 0.1	0.3 ± 0.1	0.5 ± 0.2
V_{max} (U/mg)	14 ± 2	18 ± 2	12.5 ± 0.3	5.6 ± 0.4	2.3 ± 0.1	1.1 ± 0.1

m/z 45 signal decreased at a later time in buffer containing 270 μM O_2 than it did for buffers containing 640 μM or 1280 μM O_2. In the reaction mixture containing 270 μM O_2 and 40 mM oxalate, the decrease in the m/z 45 signal appeared after 5 min and was due to oxalate consumption. Thus, an increase in the m/z 45 signal was seen after introducing additional substrate. On the other hand, the m/z 45 signal started to decrease after only 60 s and 30 s in the presence of 640 μM O_2 and 1280 μM O_2 with 40 mM oxalate, respectively. Adding more oxalate or removing O_2 (achieved by sweeping He over the top of the reaction mixture in the reaction chamber) did not change the decrease of the m/z 45 signal. The production of CO_2 was recovered when additional enzyme was added into the reaction mixture, however, indicating that decreased CO_2 production was not due to exhaustion of the substrate but to inactivation of the enzyme at the high O_2 concentration. A similar inhibition by O_2 was reported for the *Aspergillus niger* OxDC. [50]

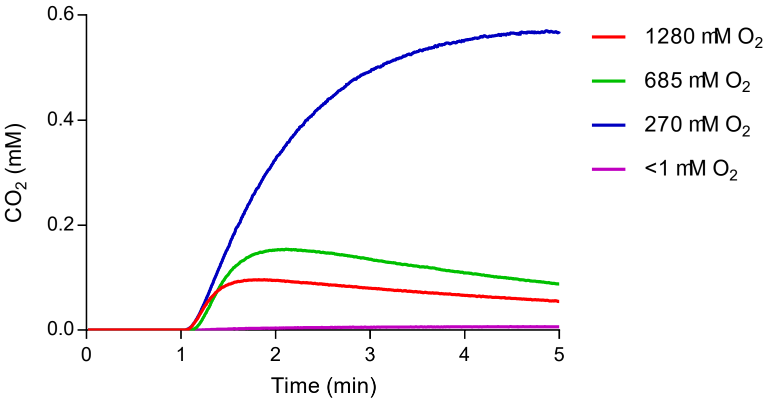

Figure 4.10. The lifetime of the DASN variant was affected by the O_2 concentration.

These studies suggest that O_2 affects enzyme activity by reducing the number of turnovers for each enzyme molecule. We proposed that O_2 inhibition over a long-term damages the enzyme by covalent bonding to a protein-based radical thereby inactivating the enzyme irreversibly.

Nitric Oxide Inhibition

Inspired by a previous NO inhibition study on WT OxDC, [54] MIMS was utilized to monitor changes in the m/z 45 ($^{13}CO_2$), m/z 32 (O_2) and m/z 30 (NO) signal after addition of MAHMA to the helium-saturated reaction buffer at pH 4.0 with the DASN variant. NO production was confirmed by observing an increase in the m/z

30 signal (Fig. 4.11). Addition of O_2-saturated water gave a decrease in the m/z 30 signal, confirming that O_2 rapidly reacts with NO generated under these conditions. Some NO was still present in solution, which could be used in NO inhibition studies of the DASN variant.

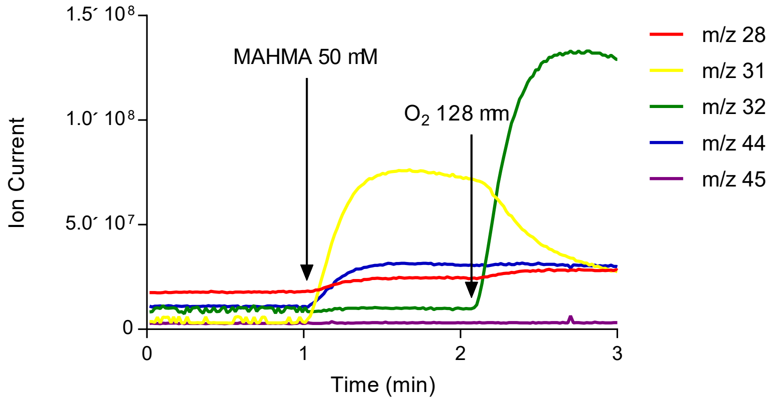

Figure 4.11. MAHMA can be used to produce NO in acidic condition.

The NO experiment on WT OxDC was performed at a low O_2 level to prevent reaction between NO and O_2. However, the situation is more complicated for studies with the DASN variant, because this variant needs to consume O_2 during catalysis. The NO experiment could not therefore be preformed under anaerobic conditions. O_2 can react with NO to spontaneously deplete O_2 and NO in solution before the addition of enzyme, and NO radicals generated from MAHMA react with the formyl radical anion intermediate in the active site or in aqueous solution. to produce HNO, which is detected by MIMS as a characteristic signal at m/z 31 (Fig. 4.12).

Different amounts of MAHMA were added to succinate buffer containing 4 mM oxalate prior to the addition of a fixed amount of O_2-saturated water and the DANS variant (Fig. 4.13). 4 mM oxalate was chosen for this measurement because the enzyme exhibits mainly OxOx activity at this concentration according to the rates of CO_2 production and O_2 consumption in the prior studies of O_2-dependence (Fig. 4.2). Although the concentration of O_2 might presumably affect the ratio of OxDC

[redacted]

Figure 4.12. Possible reactions in the reaction mixture of the DASN-catalyzed reaction in the presence of NO.

activity to OxOx activity at low O_2 levels, the oxalate concentration used in these experiments was high enough to avoid this problem, and so all CO_2 was considered to have arisen from OxOx activity.

Upon addition of MAHMA to the helium-saturated buffer, an increase in the m/z 30 signal indicated the production of NO. Following the addition of O_2-saturated water, the m/z 32 signal increased significantly, and the m/z 30 signal began to decrease. Equilibrium was reached 30 seconds after the addition of O_2. At the point which the DASN variant was added to the reaction mixture, NO and O_2 were still detectable, however, the m/z 45 signal increased when the enzyme was added into the reaction mixture. With CO_2 production, decreases in the O_2 signal were mainly due to depletion of O_2 by enzymatic catalysis because the amount of NO in solution was low.

Once all O_2 was consumed, the production of CO_2 ceased. Reintroduction of O_2 into reaction mixture resulted in recovery of CO_2 production at the same initial rate as that seen when enzyme was added to the solution at the first time. This rules out the possibility that any fall in CO_2 signal is due to depletion of oxalate.

The addition of enzyme was observed to lead to a faster decay of the m/z 30 signal. If NO only reacts with O_2 present in solution, a significant decrease of O_2 would result in an even slower decrease of the NO signal after addition of the DASN variant. Interestingly, NO concentration dropped faster when the enzyme was added

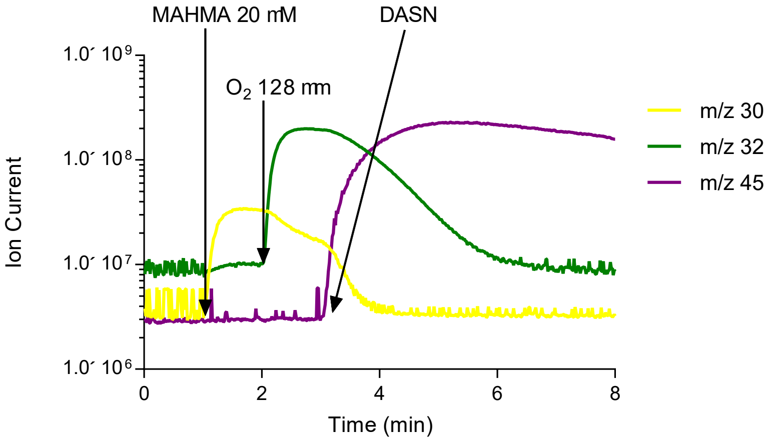

(a) 20 μM MAHMA

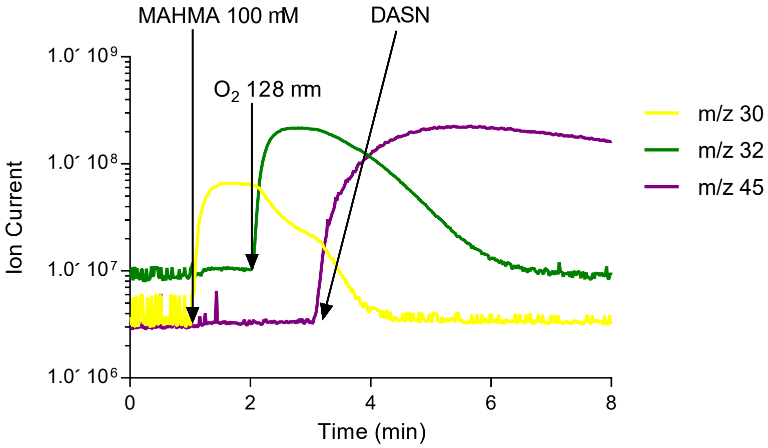

(b) 100 μM MAHM

Figure 4.13. Using MIMS to determine the ion current of $^{13}CO_2$, O_2 and NO in real-time.

in. Although it might be argued that this is due to dilution, the volume of enzyme solution added was only 0.25% of the total reaction volume. A control experiment in which the same amount of helium-saturated water was added into the NO containing solution demonstrated that the NO signal was not affected by the this dilution factor.

Therefore, the faster decrease of the NO signal suggests that NO does interact with the DASN variant in some fashion.

The enzyme also exhibited different initial velocities at different initial NO concentrations. This could have been due to the concentration of O_2 differing for each set of reactants when enzyme was introduced ,and the OxOx activity was therefore affected by O_2 concentration. Thus, the higher initial concentration of NO results that the less O_2 was present when catalysis by the DASN variant commenced. The coexistence of NO and O_2 in the first minute of reaction allowed calculation of the initial velocity of the reaction in the presence of NO, and control experiments were performed under the same conditions in the absence of NO. The reaction rate of the consumption of NO and O_2 was then calculated for the control sample, which was subtracted from further calculations. The production of CO_2 and consumption of O_2 arising from the DASN-catalyzed reaction could then be calculated with or without NO, and the effect of NO on the catalysis by the DASN variant determined. (Table 4.8)

Table 4.8.
The CO_2 production rate, the NO consumption rate and O_2 consumption rate after the addition of the DASN variant into the reaction mixture containing different initial concentrations of NO.

Initial [MAHMA] (μM)	CO_2 production (μM/min)	O_2 consumption (μM/min)	NO consumption (μM/min)
0	120	58	0
20	96	77	39
100	78	82	49

The CO_2 production rate decreased as NO concentration increased. The rate of the NO consumption did not change significantly with increased MAHMA concentrations. O_2 consumption increased with increased MAHMA concentration in the range of 0-

100 μM. For the measurement in the absence of NO, the calculated CO_2 production rate (116 μM/min) matched with the experimental data (120 μM), indicating that OxOx reaction dominates under these conditions. Assuming all the NO in solution was able to react with O_2, the calculated O_2 consumed by NO was 20 μM/min and 24 μM/min in 20μM and 100 μM of NO containing buffer, respectively. Therefore, O_2 consumed by the OxOx activity was 58 μM and 57 μM, respectively, and the calculated CO_2 production was 119 μM and 114 μM, respectively. Experimentally determined CO_2 production rates, however, were less than those calculated from the O_2 consumption rate in the presence of 20 μM and 100 μM NO, respectively, suggesting that CO_2 production is partially affected by increased NO concentration. Hence as well as the consumption of O_2 by NO, NO or NO_2 produced from reactions shown in Fig 4.13 inhibited the production of CO_2 at the same time O_2 has consumed. It is also reasonable to consider the possibility that more than one reaction in Fig 4.13 takes place in solution. In addition, if NO also reacts with the formyl radial anion intermediate, then HNO would be detected. The lack of any detectable increase in the m/z 31 signal seems to rule out this possibility.

Previous work has shown that the superoxide radical is formed during the catalysis by WT OxDC [63] and the loop hinge mutation T165V. [51] Superoxide radical and the NO radical generated from MAHMA could rapidly form peroxynitrite, [101] which under acidic conditions gave peroxynitrous acid that spontaneously isomerizes to give nitrate/nitric acid. [101] Thus, a possible mechanism for NO inhibition could also be that NO interacts with superoxide radical produced during catalysis. In this case, any Mn-bound formyl radical anion destined to form a second CO_2 in the OxOx reaction would be protonated in solution to give formate. This would lead to a decreased CO_2 production rate while the consumption of O_2 remained unchanged. There is no evidence that NO directly binds with either Mn(II) or Mn(III) from the previous studies of WT OxDC, [54] suggesting that inhibition by NO is not be due to competition with O_2 as a ligand of Mn in the active site of the enzyme.

The Dioxygen Dependency of the DESN Variant and the ΔE162 variant

The DESN variant, like WT OxDC, is able to produce CO_2 in the presence of trace amounts of O_2 (Moral, unpublished data). This suggests that the DESN variant may use a similar mechanism to WT OxDC. In air-saturated buffer, the ΔE162 variant was able to produce CO_2 in the presence of 270 μM O_2, although no CO_2 production was detected at low O_2 conditions for this variant. The V_{max} of the ΔE162 variant determined from the total production of CO_2 by MIMS was slightly higher than that calculated from standard assays, and also the significant loss in activity confirms the functional importance of Glu162 in catalysis. Moreover, the CO_2 produced by the ΔE162 variant in the MIMS experiment likely arises from OxOx activity, because CO_2 production by the ΔE162 variant is very sensitive to the presence of O_2 (Fig. 4.9).

Table 4.9.
Comparison of the kinetic parameters of the DASN, DESN and ΔE162 variants at various concentrations of O_2.

	V_{max} (U/mg) <1 μM O_2	V_{max} (U/mg) 270 μM O_2	K_M(mM) <1 μM O_2	K_M(mM) 270 μM O_2
DESN	42 ± 3	60 ± 1	7 ± 1	10 ± 1
ΔE162	<0.01	0.3 ± 0.1	a	5 ± 1
DASN	<0.01	18 ± 2	a	1.5 ± 0.2

[a] not applicable

Applying MIMS to study of several OxDC variants provides valuable information about the functional role of residues in the N-terminal loop of OxDC. Firstly, the importance of the Glu162 residue in OxDC was confirmed by mutagenesis. Secondly, the DANS variant, which exhibited both OxDC and OxOx activity, also exhibited O_2 dependence, being inhibited by O_2 at high concentration, possibly noncompetitively.

The ratio of the CO_2 production and O_2 consumption demonstrates that the amount of the DASN variant performs the decarboxylase activity 11-fold higher than the oxidase activity. The experiments in the presence of NO demonstrated inhibition of on the CO_2 production. These results not only confirm the importance of the loop, but also suggest a noncompetitive inhibition of O_2 at high concentration. Incubation in high O_2 with the present of oxalate also irreversibly damages the enzyme.

4.2.4 KIE Measurements for the DASN variant

pH Profile of the DASN Variant

The pH profile of the DASN variant was determined using the ABTS-Peroxidase assay to measure H_2O_2 formation (Fig. 4.14). Measurements were recorded over a pH range of 3.5-7.0. At pH values below 3.5 the enzyme was not stable, and aggregation and precipitation of the DASN variant occurred even at low enzyme concentrations. The pH dependence of an enzyme is associated with important residues in the active site that participate in catalysis and the protonation state of the substrate. V_{max}/K_M values were determined at different pH values for the DASN variant. V_{max}/K_M decreased as the pH increased up to 7, while V_{max} had a maximal value at pH 4.2. V_{max}/K_M and pH values were fitted to equation (4.2).

$$logy = log[\frac{C}{1+\frac{K}{H}}] \tag{4.2}$$

where V_{max}/K_M is the value of y, H denotes the proton concentration and K and C are constants. The calculated pK_a was 4.6 and the slope of log V_{max}/K_M versus pH was approximately -1.

This pK_a value for the DASN variant is greater than that compared for WT OxDC by 0.4 pH units. In a previous work of WT OxDC, this observation led to the conclusion that monoprotonated oxalate is the true substrate. [61] On the other hand, one of the best-characterized oxalate oxidase, *Cs*OxOx, exhibits a pK_a = 4.6, [68] which is similar to the value reported here. An unprotonated carboxylate

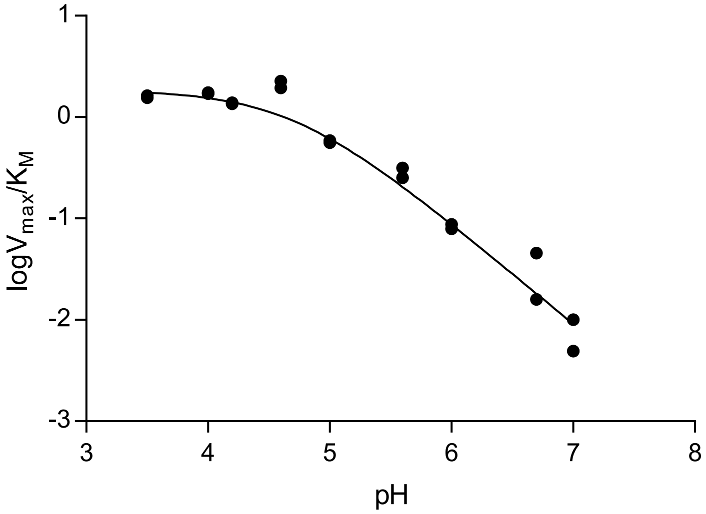

Figure 4.14. pH profile of the DASN variant measured by ABTS-Peroxidase assay.

group near the active site of *Cs*OxOx was proposed to contribute to catalysis. Thus, the simplest interpretation of the pH profile of the DASN variant of OxDC is that the monoprotonated oxalate is still the substrate, but the shift in the computed pK_a suggests that mutation of the loop region may render the enzyme to become more like an OxOx.

Heavy Atom KIEs Determination

^{13}C kinetic isotope effects for the DASN variant were measured using the internal competition method, in which the isotope effects are exhibited by V_{max}/K_M. The theory and experimental procedure have been described in Chapter 2. Reactions were performed at pH 4.2 and pH 5.7 in a similar manner to KIE studies on WT OxDC. [61] Both OxDC activity and OxOx activity were detected in the DASN variant at high oxalate concentrations in the steady-state kinetic study. An oxalate concentration of 1 mM was used in the KIEs experiments for the DASN variant, because OxOx activity is the main reaction at this oxalate concentration. An aliquot was taken from each reaction and an oxalate detection kit confirmed that oxalate used to form formate comprised only 3% of total oxalate consumption. Apparent IEs were calculated based on residual oxalate using equation (2.1)

Table 4.10.
Heavy atom kinetic isotope effects CO_2 $^{13}(V/K)$ of the DASN variant. The WT data was adapted from [61]

pH	4.2	5.7
WT [61]	1.005 ± 0.001	1.008 ± 0.001
DASN	1.0036 ± 0.0009	1.006 ± 0.001

Overall, the $^{13}(V/K)$ for CO_2 of the DASN variant was similar to that determined for WT OxDC. (Table 4.10) A normal 0.03-0.05 ^{13}C IE is expected for the C-C bond cleavage if it is the rate-limiting step. The experimental data for the DASN variant was 10-fold smaller, indicating that a slower step existed prior to C-C bond cleavage. The observed $^{13}(V/K)$ values at pH 4.2 and pH 5.7 for the DASN variant were both smaller than that of WT OxDC (normal 0.005) suggesting that steps before the decarboxylation step made more contribution limiting the reaction rate than occurs in WT OxDC. Also, the $^{13}(V/K)$ at pH 4.2 was smaller than that at pH 5.7, which was the same situation for WT OxDC. This was interpreted as the effect of the external commitment in pH 5.7 buffer.

Data Analysis

Because this KIE only reflects steps up to and including the first irreversible step, mechanism changes occurring after cleavage of the C-C bond do not affect the observed IEs. [61] The minimal mechanistic model included steps up to the decarboxylation step (Fig. 2.7), and equation (2.3) was obtained using the net rate constant method. All assumptions used in data analysis were the same as used for WT OxDC. [61] More specifically, assuming only k_3, k_4 and k_5 are isotope sensitive, expression of ^{13}C IEs on the V/K for CO_2 can be written as:

$$^{13}(V/K) = \frac{^{13}K_{eq3}{}^{13}k_5 + {}^{13}k_3(\frac{k_5}{k_4}) + \frac{k_3 k_5}{k_2 k_4}}{1 + (\frac{k_5}{k_4})(1 + \frac{k_3}{k_2})} \tag{4.3}$$

For the ^{13}C IEs on CO_2 at pH 5.7, three assumptions were made to simplify the interpretation. [61] 1), k_3/k_2 is small because the reaction rate is slow at this pH. 2), $^{13}k_5$, the IE of decarboxylation on CO_2, is 1.04, which is the average value for these reactions reported in the literature. [61] In addition, $^{13}K_{eq3}$and $^{13}k_3$ were both set to be 1 since the ^{13}C IE for removing the proton from the carboxylate group is negligible.

$$^{13}(V/K) = \frac{1.04 + (k_5/k_4)}{1 + (k_5/k_4)} = 1.006 \tag{4.4}$$

Based on these assumptions, the calculated k_5/k_4 of the DASN variant is 5.7, suggesting that the decarboxylation step is 5.7-fold faster than the step in which the putative enzyme-oxalate radical complex reverts to the Michaelis-complex. This value is close to that of WT OxDC (4).

For the ^{13}C isotope effect on CO_2 at pH 4.2, similar assumptions were made. [61] 1), k_3/k_2 is no longer negligible, because reaction was faster at this pH and the observed IEs were smaller than those at pH 5.7. 2), $^{13}k_5$, the isotope effect for decarboxylation on CO_2, is 1.04, which is the average value for such reactions. [61] 3), $^{13}K_{eq3}$ and $^{13}k_3$ were both set to be unity since the ^{13}C IE for removal of the proton from the carboxylate group is negligible. 4), k_5/k_4 is the same as the calculated value at pH 5.7, i.e. the same intermediate is produced at the different pH values.

$$^{13}(V/K) = \frac{(1.04) + (5.7)(1 + \frac{k_3}{k_2})}{1 + (5.7)(1 + \frac{k_3}{k_2})} = 1.0036 \tag{4.5}$$

Solving this equation gives $k_3/k_2 = 0.78$, which is similar to the value determined for WT OxDC of 0.75.

The $^{13}(V/K)$ value is much smaller than the intrinsic value (3%-5%) for breaking a C-C bond in a rate-limiting step, suggesting that a isotope-sensitive step exists before decarboxylation. Moreover, the almost identical k_3/k_2 for the DASN variant and WT OxDC implies the same ability for the DASN variant to stabilize the Michaelis complex. Given that K_M for the DASN variant obtained by MIMS is similar to that of WT OxDC, it is possible that k_2 and k_3 of the DASN variant are similar to the k_2 and k_3 of WT, respectively. Also, the k_5/k_4 is very close to the value of WT OxDC, suggesting that the structure of the transition state is the same as that of WT. In the previous study, [61] the transition state structures of the oxalate radical was proposed to be the resonance structure shown in Fig.4.15. This might also be the case for the reaction catalyzed by the DASN variant.

[redacted]

Figure 4.15. Structure of the transition state in the DASN-catalyzed reaction.

Thees KIEs support the hypothesis that the DASN variant and WT OxDC share the same mechanism before the first irreversible step. However, since Glu162 is absent in the DASN variant, there is no general based to deprotanate the substrate to facilitate any proton-coupled electron transfer. The KIEs results still, however, suggest a slow step prior to the decarboxylation. Given that the determined $pK_a =$ 4.6, it is possible that an alternative residue around the N-terminal active site in the DASN variant can function as a general base to deprotonate oxalate. It has been proposed that, in *Cs*OxOx, a conserved aspartate residue (Asp241) contributes to enzyme catalysis based on the pH profile of the enzyme. [68] Given the fact that the pK_{a1} for *Cs*OxOx is 4.5, which is closed to the pK_a determined for the DASN variant, Asp161 in the DASN variant of OxDC might operate as a general base in catalysis.

This would also explain that the SANS variant exhibited no increase in OxOx activity (Table 4.3).

4.2.5 Spin-trapping Experiments of the Loop Variants

The spin trapping reagent PBN was used to trap the formyl radical intermediate during catalysis by the DASN variant. The signal of the adduct radical was monitored by CW X-band EPR (Fig. 4.16). Because the reaction of PBN and the formyl radical yields a more stable radical. A standard curve was established using a series of known concentrations of TEMPO. Reactions for the DANS variant and WT OxDC were performed at room temperature in 50 mM oxalate, 50 mM citrate buffer, pH 4.0, 75 mM PBN for 4 min. Based on the TEMPO standard, 2.4 μM, 81 nM, 0.7 μM and 76 nM formyl radical were trapped during the catalysis of DASN variant, the DESN variant, the ΔE162 variant and WT OxDC, respectively.

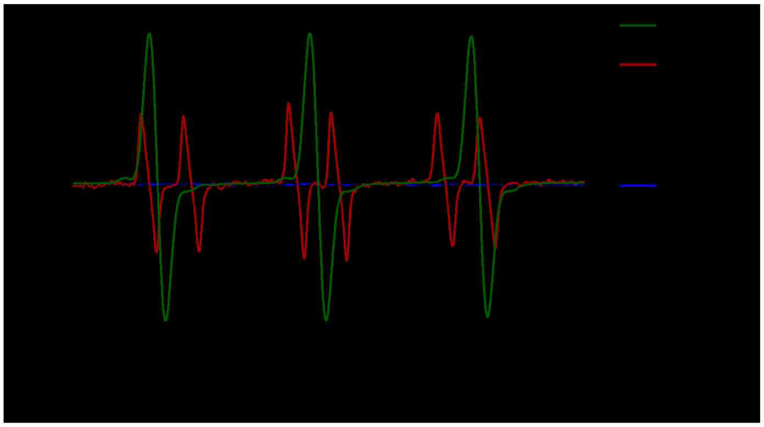

Figure 4.16. Spin-trapping experiments of the DASN, DESN and ΔE162 variants. Figure was prepared by Dr. Alexander Angerhofer and U. Twahir.

The concentration of the spin-trapped radicals were at much lower concentrations than the calculated concentration of the intermediate based on kinetic data. Comparison of the signal intensities between each loop variant reflects differences in the ability of the spin-trapping reagent to react with the intermediate. Among all three loop variants, the DASN variant exhibited a 30-fold increase of the EPR signal compared to WT OxDC, and the signal intensity of the adduct radical for the DESN variant and the ΔE162 variant were lower than for the DASN variant.

The time course of formation of the PBN-trapped adduct for the DASN variant showed an increase in signal intensity initially, but the signal started to decay after approximately 4 min (Fig. 4.17). The production of the radical adduct also exhibited a dependence on oxalate concentration. Concentrations of the radical adduct at different oxalate concentrations were calculated and fitted to Michaelis-Menten equation(Fig. 4.18).

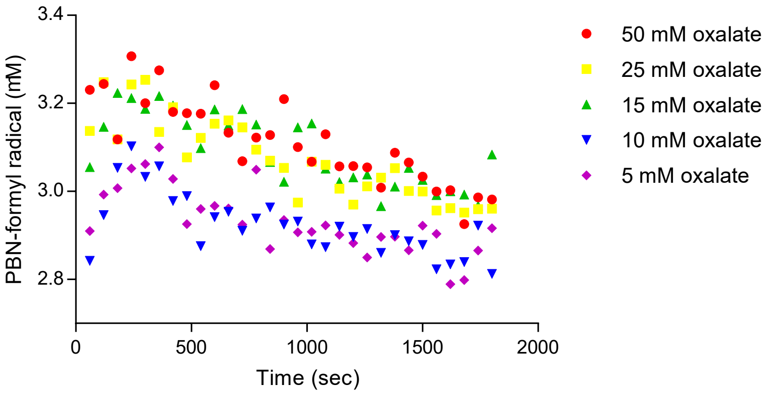

Figure 4.17. Time-course of the EPR signal of the PBN-formyl radical adduct in varying concentrations of oxalate. Data was collected by U. Twahir.

These results give $V_{max} = 1.1 \text{ x } 10^{-3}$ U/mg for the PBN-formyl radical adduct, which is approximately 5000-fold less than the V_{max} of OxOx activity determined from the production of H_2O_2. Considering that the concentration of PBN in the initial reaction mixture was 75 mM, the trapped radical therefore represents only a very small fraction. One explanation for the inefficient spin-trapping may be due to an intrinsic instability of the radical adduct, and the V_{max} calculated here is the net

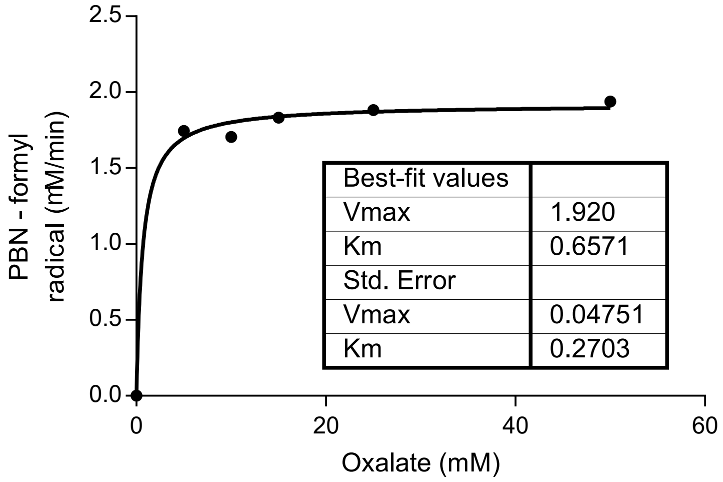

Best-fit values	
Vmax	1.920
Km	0.6571
Std. Error	
Vmax	0.04751
Km	0.2703

Figure 4.18. Calculated concentration of the PBN-foymly radical adduct was fitted to the Michaelis-Menten equation.

velocity for formation and decay of the trapped radical. A second possibility is that the amount of formyl radical trapped was very small because most of this intermediate cannot interact with PBN. In this case, it is likely that the formyl radical anion is produced in the active site of the enzyme, but PBN only can react with radicals that "leak out" of the enzyme.

The T165V variant, showed a high signal intensity in similar spin-trapping EPR experiments. [62] This was believed to be due to abnormal loop movement in the T165V variant increasing the likelihood of the spin-trap reaction, and this proposal was supported by the position of Glu162 in the X-ray crystal structure of this variant. [62] Although the possibility that the PBN adduct formation occurres with in OxDC cannot be completely ruled out, when the loop is not able to maintain an isolated environment in the active site, the intermediate has a higher chance of reacting with PBN.

Although the loop hinge residue Thr165 is still present in both the DASN and DESN variants, the signal intensity change was attributed to the effect of mutation at position 162 on the loop, suggesting that the role of Glu162 in WT OxDC is to lock the loop in the correct conformations during catalysis.

Meanwhile, the DASN variant exhibited the highest OxOx activity together with the smallest OxDC activity, while the DESN variant exhibits 60% WT OxDC activity with no significant increase in OxOx activity. It seems that the intensity of the spin-trap signal correlated with the OxOx activity of the enzyme. The basis of this observation might be that the impaired loop in the DASN variant is no longer able to keep the formyl radical inside the N-terminal metal binding site, and so the radical leaks from the active site of the DASN variant and undergoes an uncatalyzed reaction (Fig. 4.19) in solution to give H_2O_2. This leaking of the radical is prevented by the presence of Glu162, as seen for the DESN variant and WT OxDC.

[redacted]

Figure 4.19. Reaction of the uncatalyzed reaction of H_2O_2.

Assuming that the main reason for the high OxOx activity observed in the DASN variant is due to leakage of the formyl radical, one might expect competition between O_2 and PBN to react with the formyl radical in the spin-trapping experiment. The reaction in Fig. 4.17 is at diffusion rate, and PBN adduct formation is pseudo first-order when the concentration of the PBN is fixed. [102] The apparently small proportion of formyl radical anion trapped by PBN can also be explained by O_2 winning the competition with PBN.

4.2.6 X-band EPR Experiments of the Loop Variants

The CW X-band EPR experiments of the DASN, DESN, and ΔE162 variants were performed under various conditions using perpendicular and parallel mode EPR.

The DASN Variant

Perpendicular mode EPR spectra of the DASN variant were recorded in basic storage buffer at pH 8.5. As previously reported, [56] the spectrum of the perpendicular mode EPR of the DASN variant showed a typical six-line split for the hexa-coordinate Mn(II) at $g = 2$, while the Mn(II) half-field transition signal was present at $g = 4.2$ (Fig. 4.20). The parallel mode EPR spectrum of the DASN variant at pH 8.5 exhibited a sextet signal centered near 1388 G corresponding to the $\Delta M_s = \pm$ 2-transition of Mn(II) but, as expected, no Mn(III) signal was observed under these conditions (Fig. 4.21).

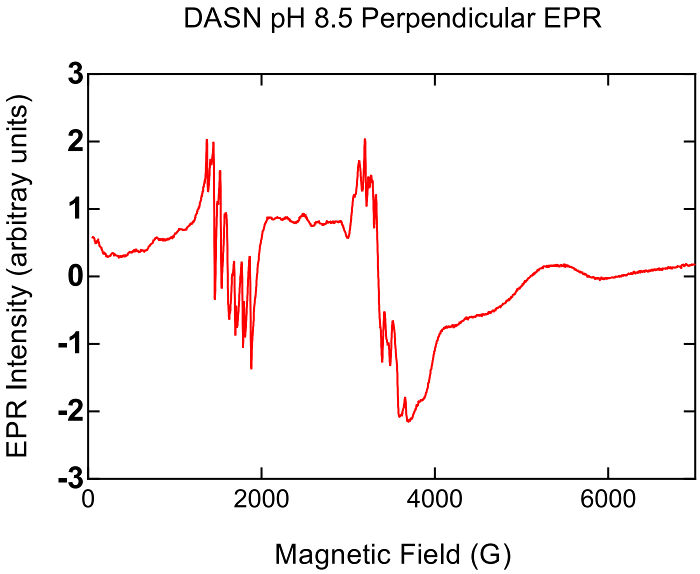

Figure 4.20. X-band perpendicular mode EPR spectrum of the DASN variant in the absence of oxalate at pH 8.5. Data was collected with U. Twahir.

EPR spectra of the DASN variant were recorded at the pH 4.0 using perpendicular and parallel modes. In perpendicular mode, the spectrum was similar to that acquired at pH 8.5, with an increase in signal intensity at $g = 2.0$ and a decrease in signal intensity at $g = 4.3$. This indicates a change in metal coordination from penta-

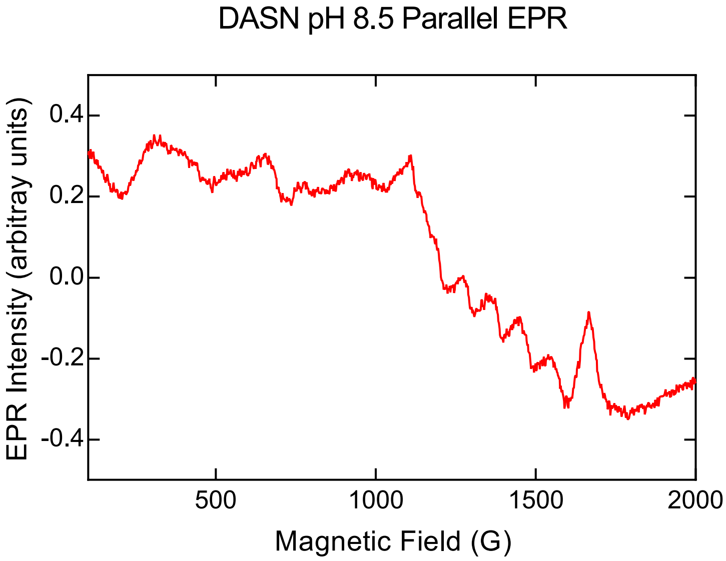

Figure 4.21. X-band parallel mode EPR spectrum of the DASN variant in the absence of oxalate at pH 8.5. Data was collected with U. Twahir.

coordinate to hexa-coordinate (Fig. 4.22). The parallel mode EPR spectrum of the DASN variant at pH 4.0 was similar to that observed for WT OxDC, but the signal intensity from the forbidden-transition of Mn(II) center was reduced. No Mn(III) signal was present in the spectrum under these conditions (Fig. 4.23).

Next, EPR spectra of the DASN variant in the presence of oxalate at pH 4.0 were recorded, and data at different time points during catalysis were collected. The perpendicular mode EPR spectrum of the DANS variant in the presence of oxalate was similar to the spectrum of the free enzyme at pH 4.0, confirming the existence of Mn(II) in the protein. (Fig 4.25) When oxalate is present, the sextet signal at g = 4.3 was low as compared to a spectrum of the enzyme-only sample at the same pH, although the signal at g = 2.0 remained. Some new features were present on each shoulder of the signal at g = 2.0. A similar broad feature centered at 2340 G and 3050 G in WT OxDC was interpreted in a previous multi-frequency EPR study [90], aarising from the two different Mn(II) sites. During catalysis, the intensity

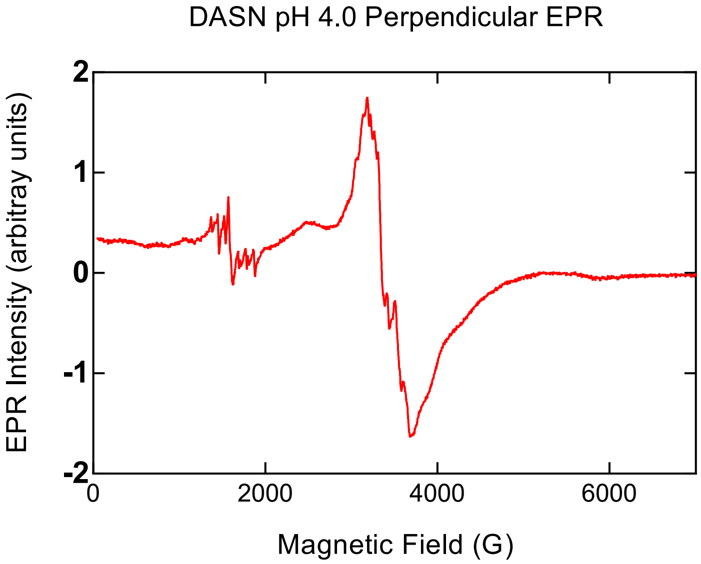

Figure 4.22. X-band perpendicular mode EPR spectrum of the DASN variant in the absence of oxalate at pH 4.0. Data was collected with U. Twahir.

of the characteristic Mn(II) signal at $g = 2.0$ increased slightly. Such signal intensity increase at $g = 2.0$ indicates more hexa-coordinate manganese. Another possibility is that oxalate binding affected the signal at $g = 2.0$. As discussed previously, the DASN variant is able to catalyze both OxDC activity and OxOx activity at high oxalate concentrations of oxalate. If the initial binding mode for these two reactions are different, then a change in coordination, as reflected in the EPR signal, would be expected.

The spectrum of the DASN variant weas acquired in the presence of oxalate at pH 4.0 under parallel mode (Fig.4.25). In addition to the forbidden-transition of Mn(II) at 1000-1500 G, a new sextet signal appeared at 500-1000 G ($g = 10$), and this signal was assigned as octahedral Mn(III). It was possible to observe formation of Mn(III) as early as 5 s. Although at this time point, the enzyme had undergone multiple turnovers, this is direct evidence that Mn(III) was formed in the presence of

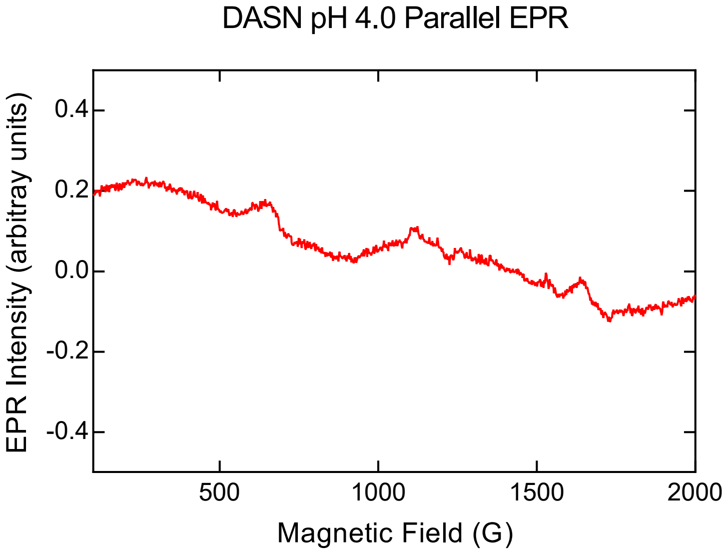

Figure 4.23. X-band parallel mode EPR spectrum of the DASN variant in the absence of oxalate at pH 4.0. Data was collected with U. Twahir.

oxalate during catalysis. After 4 min, the Mn(III) signal disappeared while the Mn(II) signal was still present, indicating of the end of reaction due to the consumption of oxalate. This was confirmed by resumption of enzyme activity following addition of more oxalate into the EPR tube after thawing the protein sample.

The DESN Variant

The perpendicular mode EPR spectrum of the DESN variant was acquired at pH 8.5 using the same sample preparation procedure as for the DASN variant discussed above (Fig. 4.26). As expected, it exhibited the same Mn(II) signal at g = 2.0 and g = 4.3, indicating that the hexa-coordinate Mn(II) is present in the purified enzyme. In the parallel mode, the forbidden-transition of Mn(II) was the only signal that was identified at pH 8.5 in the absence of oxalate, as seen in the spectrum of the DASN variant under the same conditions (Fig. 4.27).

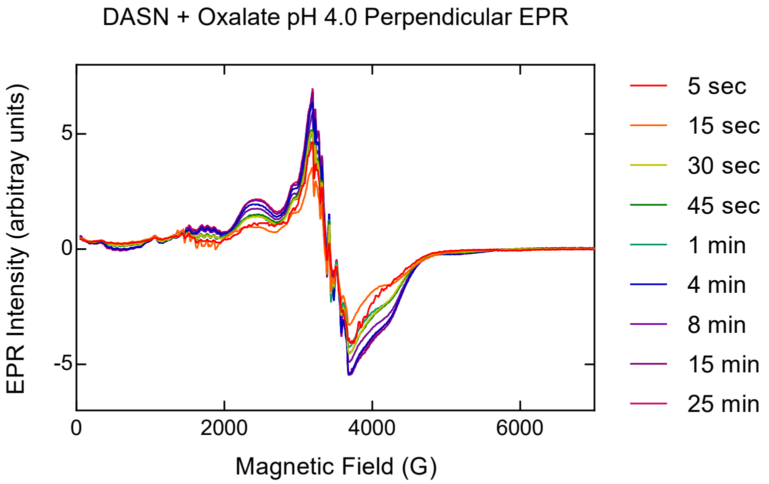

(a) Time course EPR

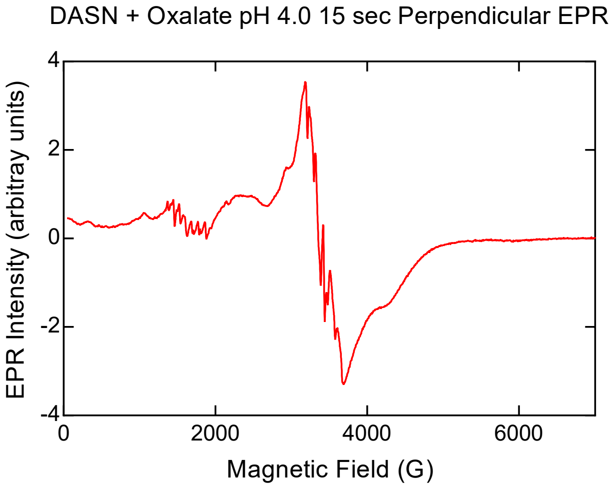

(b) EPR spectrum at 15 s

Figure 4.24. Time-course of the X-band perpendicular mode EPR spectra of the DASN variant in the presence of oxalate at pH 4.0. Data was collected with U. Twahir.

At pH 4.0, a broad signal centered at 2380 G appeared, similar to that seen for the DANS variant. (Fig.4.28) The signal at $g = 4.3$ decreased, as did the corresponding signal in the spectrum of the DASN variant. In the parallel mode EPR spectrum,

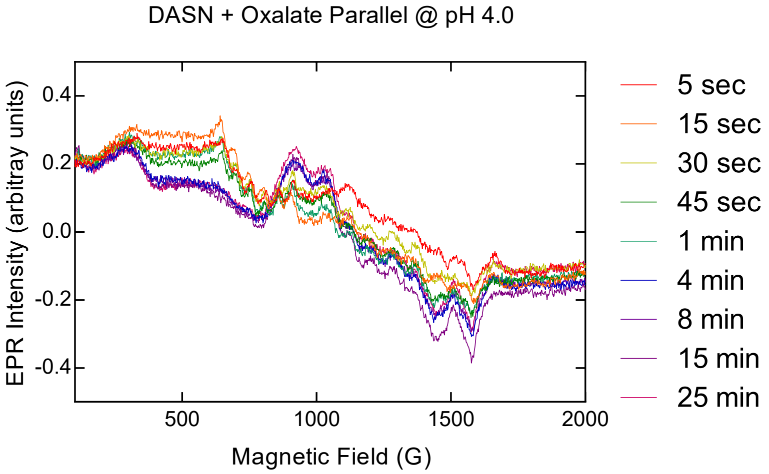

(a) Time course EPR

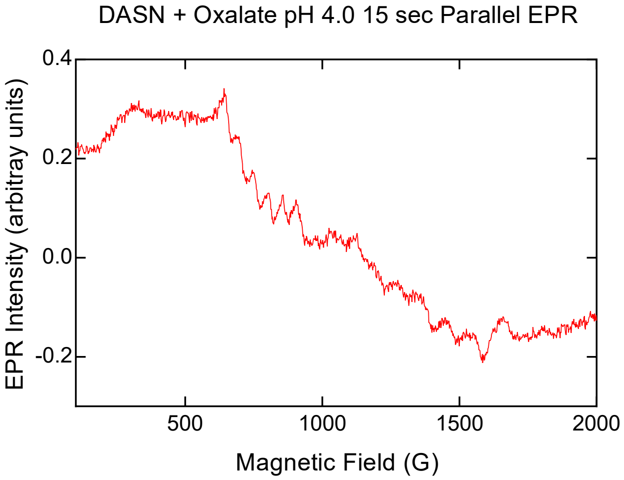

(b) EPR spectrum at 15 s

Figure 4.25. Time-course of the X-band parallel mode EPR spectra of the DASN variant in the presence of oxalate at pH 4.0. Data was collected with U. Twahir.

no Mn(III) signal was present, and even the Mn(II) forbidden-transition was barely visible. This is similar to the spectrum of WT OxDC at pH 4.2 (Fig.4.29).

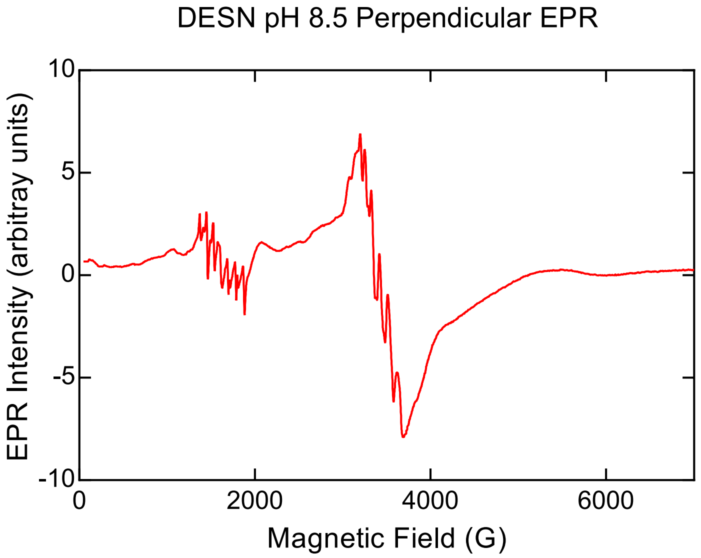

Figure 4.26. X-band perpendicular mode EPR spectrum of the DESN variant in the absence of oxalate at pH 8.5. Data was collected with U. Twahir.

A time-course experiment was performed for the DESN variant in the presence of oxalate at pH 4.0 using the perpendicular and parallel mode EPR. An increased signal at $g = 2.0$ of Mn(II) was observed in the perpendicular mode EPR spectrum (Fig. 4.30). The parallel mode spectrum of the DESN variant once again confirmed the formation of the Mn(III) species in the presence of oxalate at pH 4.0(Fig.4.31).

The ΔE162 Variant

The perpendicular mode spectrum (Fig. 4.32) and the parallel mode spectrum (Fig. 4.33) of the ΔE162 variant exhibited no significant difference from those of the DASN or DESN variants in the absence of oxalate at pH 4.0, suggesting that manganese coordination in the ΔE162 variant is similar to that of the other two loop variants at this pH value.

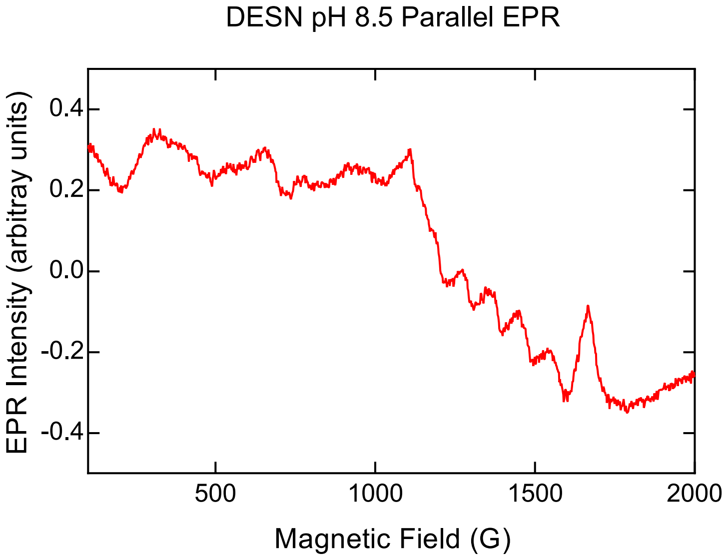

Figure 4.27. X-band parallel mode EPR spectrum of the DESN variant in the absence of oxalate at pH 8.5. Data was collected with U. T. Twahir.

Interestingly, when the time-course experiment was performed on the ΔE162 variant in the presence of oxalate at pH 4.0 (Fig. 4.34), a sharp singlet signal appeared at $g = 2.0$ after 1 min of reaction then decayed after 4 min. This signal was previously assigned to be a tyrosyl radical in the literature. [91] The parallel mode spectrum of the ΔE162 variant indicated that Mn(II) was still the dominant species in the protein (Fig. 4.35). The parallel mode spectrum of 1 min reaction showed a very weak Mn(III) signal centered at 750 G, and this signal completely vanished in subsequent time points. The loss of the Mn(III) signal in the ΔE162 variant was not due to the consumption of the oxalate over 4 min, because the ΔE162 variant exhibited low OxDC and OxOx activities.

The results of the X-band EPR study of the OxDC loop variants can be summarized as follows. First, hexa-coordinate Mn(II) is the dominant species existing in the purified OxDC loop variants, and Mn(III) is produced when the enzyme is incubated with oxalate under acidic conditions. When oxalate is depleted, the Mn(III) signal

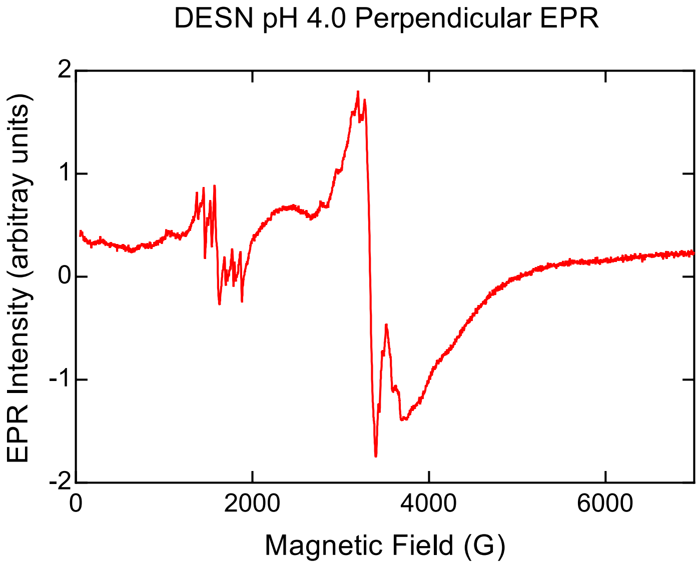

Figure 4.28. X-band perpendicular mode EPR spectrum of the DESN variant in the absence of oxalate at pH 4.0. Data was collected with U. Twahir.

was no longer detectable by parallel mode EPR. In addition, the tyrosyl radical reported literature is not involved in the catalysis, but arises from a side reaction which may lead to inactive enzyme.

4.2.7 Crystal Structure of the ΔE162 Variant

The crystal structure of the ΔE162 variant was solved through a collaboration with Dr. Karen Allen's group (Boston University). This structure is the first OxDC crystal structure that has oxalate bound to the metal in the N-terminal active site of any OxDC variant (Fig. 4.36). Although the ΔE162 variant that was crystallized as a cobalt-containing enzyme, this metal substitution should have little influence on metal coordination compared to manganese-containing enzyme, as confirmed in a previous crystal structure of a cobalt-containing OxDC variant. [99]

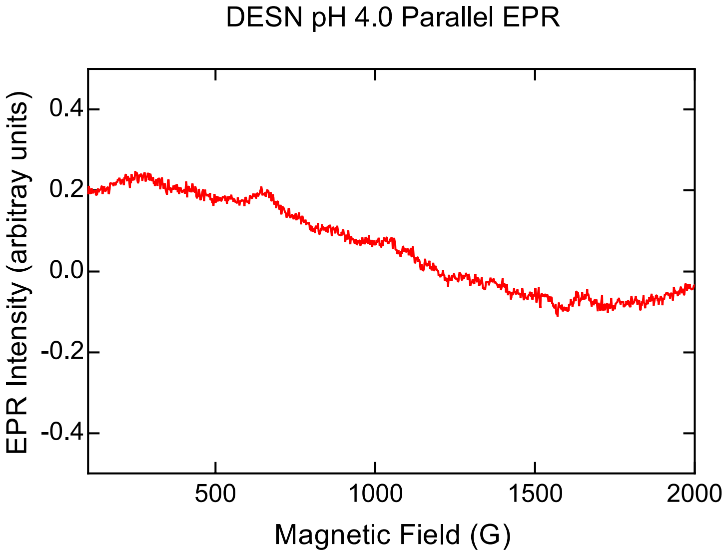

Figure 4.29. X-band parallel mode EPR spectrum of the DESN variant in the absence of oxalate at pH 4.0. Data was collected with U. Twahir.

In this ΔE162 structure, the oxygen on the carboxylate group at one end of oxalate coordinates with the metal in a mono-dentate fashion. This is consistent with the proposed mechanism based on heavy atom KIE measurements. The second oxygen on this carboxylate group forms a hydrogen bond with a water molecule that coordinates to cobalt. Presumably, this water molecule would be substituted by O_2. It was not, however, possible to identify a O_2 binding pocket around the metal in this structure (Fig. 4.38). At the other end of oxalate, Thr165 forms a hydrogen bond with the carboxylate group. Another oxygen on this group is within hydrogen bonding distance of a conserved water molecule in the cavity of the N-terminal metal binding site. Interestingly, this water molecule is also within hydrogen bonding distance to the conserved residue, Tyr200. Although the role of Tyr200 remain unclear, the structure shown here implies a hydrogen bonding network that may contribute to catalysis. Due to the deletion of Glu162, the loop in ΔE162 is shorter than that of WT OxDC. When the structure of the ΔE162 variant and WT

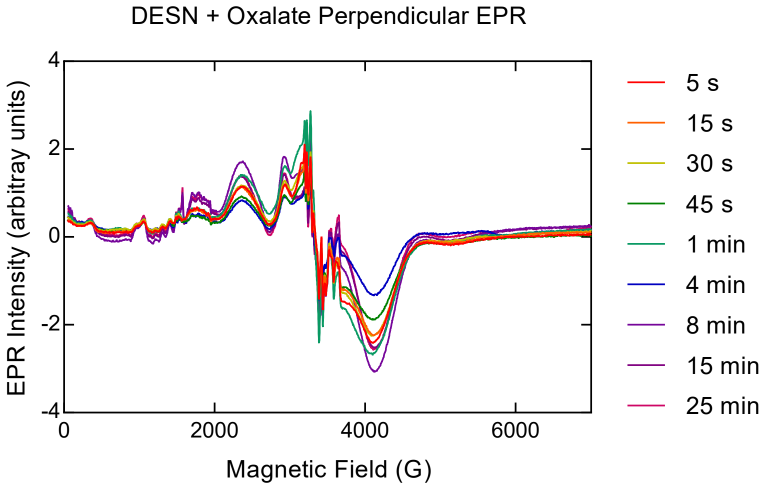

(a) Time course EPR

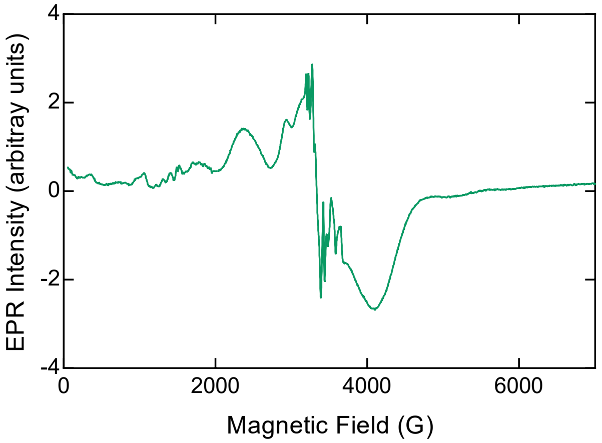

(b) EPR spectrum at 1 min

Figure 4.30. Time-course of X-band perpendicular mode EPR spectra of the DESN variant in the presence of oxalate at pH 4.0. Data was collected with U. Twahir.

OxDC with the loop in closed form(PDB 1UW8) are superimposed, a steric clash of oxalate and Glu162 in the closed conformation is observed, suggesting that this closed conformation may not represent the catalytically active form of the protein but simply results from favorable positioning of the Glu162 side chain in the absence

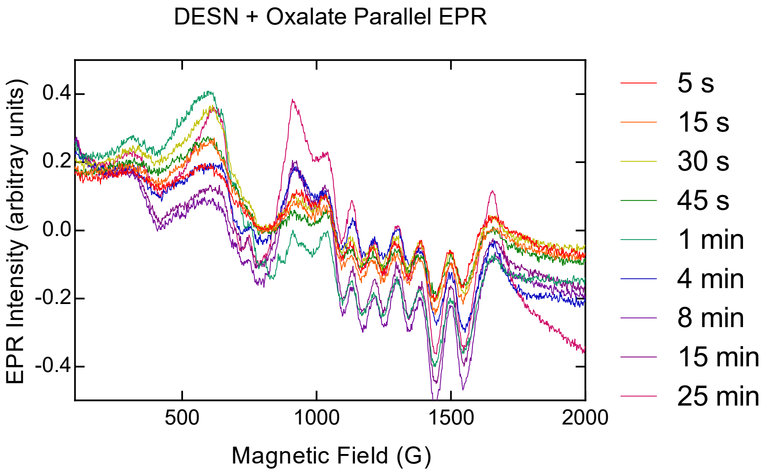

(a) Time course EPR

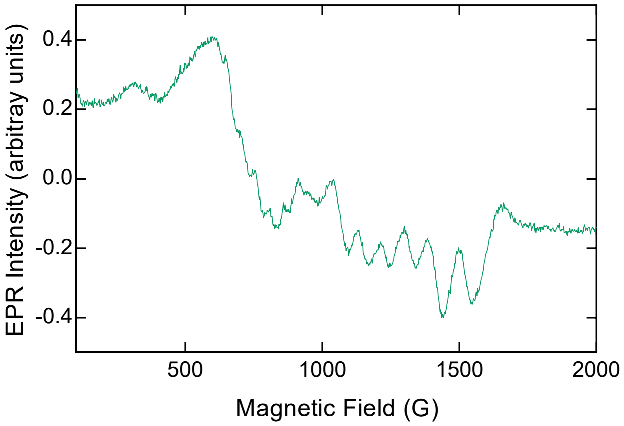

(b) EPR spectrum at 1 min

Figure 4.31. Time-course of X-band parallel mode EPR spectra of the DESN variant in the presence of oxalate at pH 4.0. Data was collected with U. Twahir.

of substrate (Fig. 4.39). The oxalate molecule is perpendicular to the side chain of Glu162, and at this orientation, the carboxylate group of Glu162 can interact with the most distant oxygen in oxalate from the metal. This is also consistent with the binding mode in the currently accepted mechanism (Chapter 1).

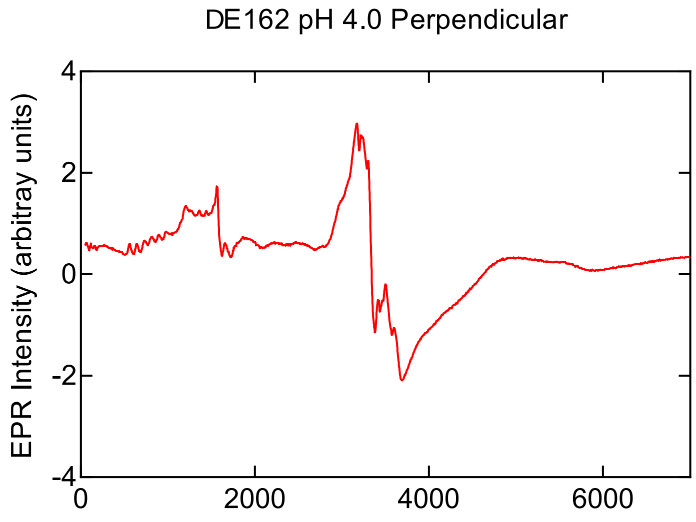

Figure 4.32. X-band perpendicular mode EPR spectrum of the ΔE162 variant in the absence of oxalate at pH 4.0. Data was collected with U. Twahir.

4.3 Conclusion

The research discussed in this chapter confirms that Glu162 is crucial for the enzyme to maintain OxDC activity, but the absence of Glu162 lower both OxDC and OxOx activities. The results of the KIE experiments of the DASN variant suggest that the initial steps in the catalytic mechanism for the loop variant and WT OxDC are identical, and this idea is also supported by the EPR evidence for the formation of Mn(III) in the presence of oxalate at catalytic active pH. The crystal structure of the ΔE162 variant with oxalate bound in the N-terminal active site indicates monodentate coordination of oxalate which confirms mechanistic models for WT OxDC.

The steps after decarboxylation result in the observed OxOx activity of the DASN variant. For a enzyme that exhibits two different activities with different K_M for the same substrate, several possibilities can explain this observation. One is that these two reactions occur in different metal binding sites of OxDC. However, the shared initial steps seems to rule out this possibility. The second possibility is that the two

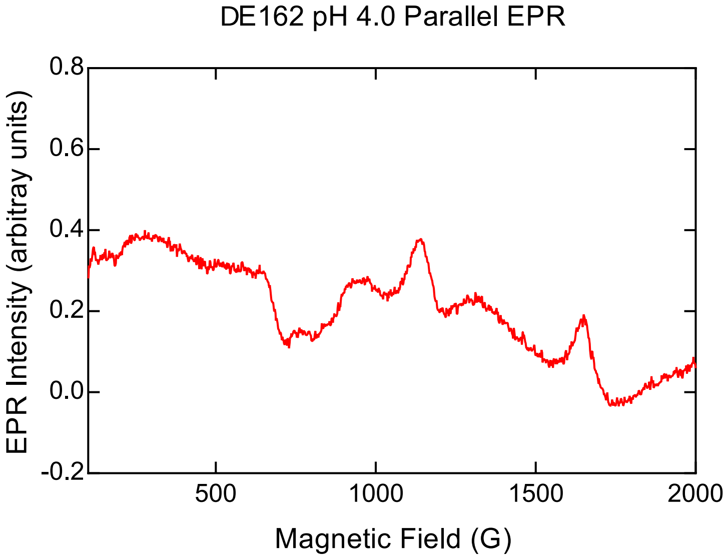

Figure 4.33. X-band parallel mode EPR spectrum of the ΔE162 variant in the absence of oxalate at pH 4.0. Data was collected with U. Twahir.

reactions share the initial steps but that the second oxidation takes place outside the active site due to the leakage of an intermediate. This in turn implyes that impaired loop function in the absence of Glu162, which fails to keep the formyl radical inside the enzyme. A mechanism involving an uncatalyzed reaction is supported by spin-trapping experiment using EPR spectroscopy, and the ratio of CO_2 production and O_2 consumption in MIMS study. If OxOx activity in the DASN variant is purely due to the uncatalyzed reaction occurring outside the enzyme, the only explanation for O_2 inhibition is that O_2 inhibits a step prior to formation of formyl radical. A third possibility is that the N-terminal site can catalyze two reactions at the same time with different efficiencies depending on the loop conformation. The fact that O_2 inhibits the DASN variant noncompetitively supports the idea that the observed OxOx activity is enzyme catalyzed reaction. If the DASN variant catalyzes the oxidation of oxalate in the same manner as the native OxOx, in which O_2 is one of the substrates in the metal binding site, it is then reasonable to expect that O_2 shows substrate inhibition at high

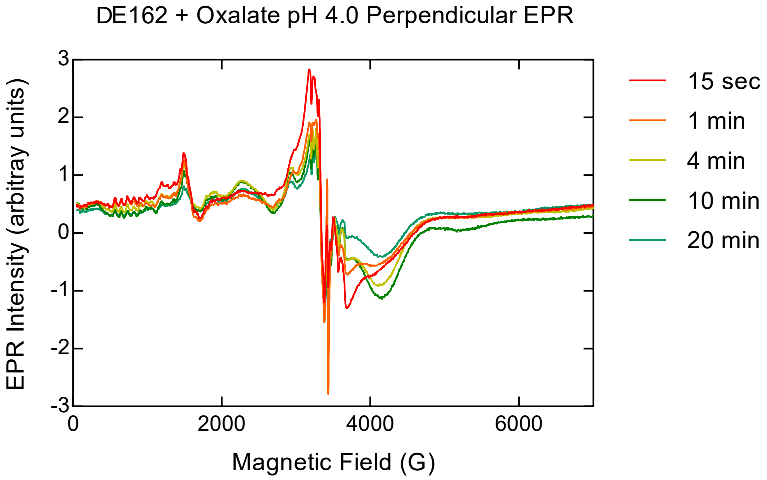

(a) Time course EPR

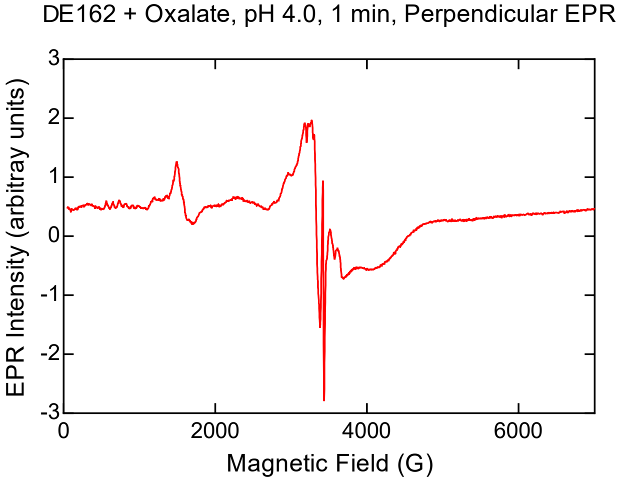

(b) EPR spectrum at 1 min

Figure 4.34. Time-course of X-band perpendicular mode EPR spectra of the DESN variant in the presence of oxalate at pH 4.0. Data was collected with U. Twahir.

concentrations. But overall, the radical-leaking mechanism is the supported by KIE measurement, spin-trapping experiment and the MIMS measurement, suggesting that this is the most likely mechanism for the DASN variant.

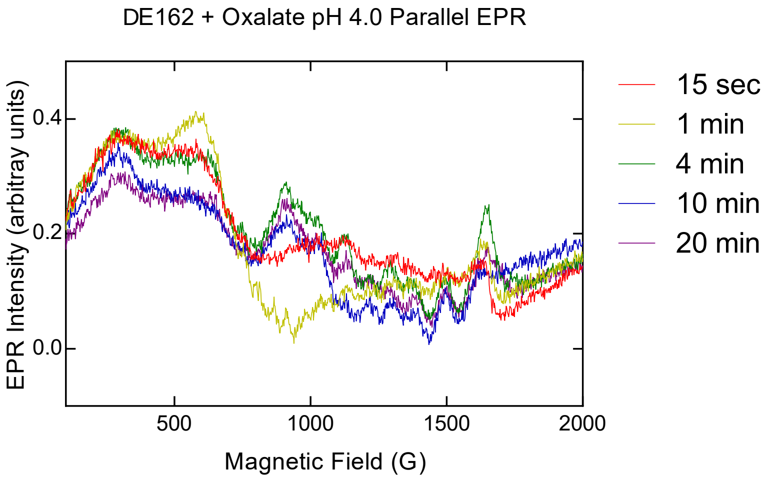

(a) Time course EPR

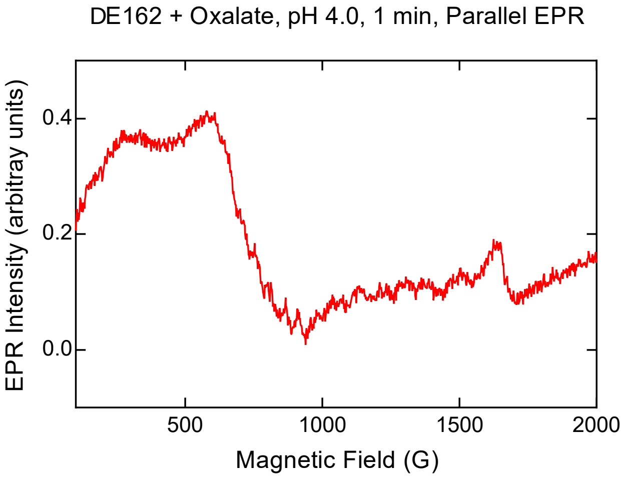

(b) EPR spectrum at 1 min

Figure 4.35. Time-course of X-band parallel mode EPR spectra of the DESN variant in the presence of oxalate at pH 4.0. Data was collected with U. Twahir.

4.4 Experimental Section

Unless stated otherwise, all chemicals and reagents were purchased from Fisher (Pittsburgh, PA) or Sigma-Aldrich (St. Louis, MO). $^{13}C_2$-oxalic acid (99%) was pur-

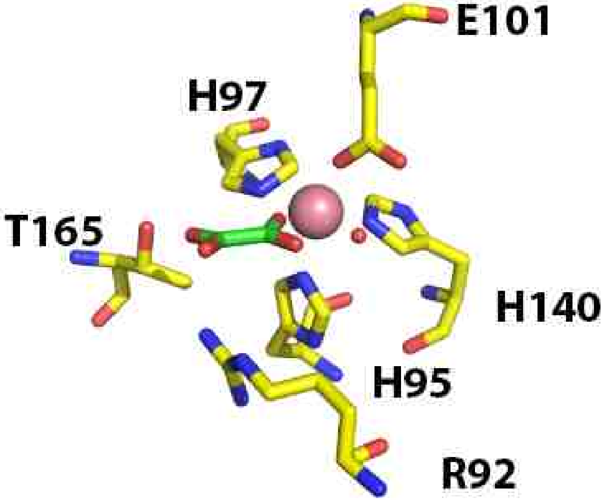

(a) oxalate bound N-temrinal metal binding site

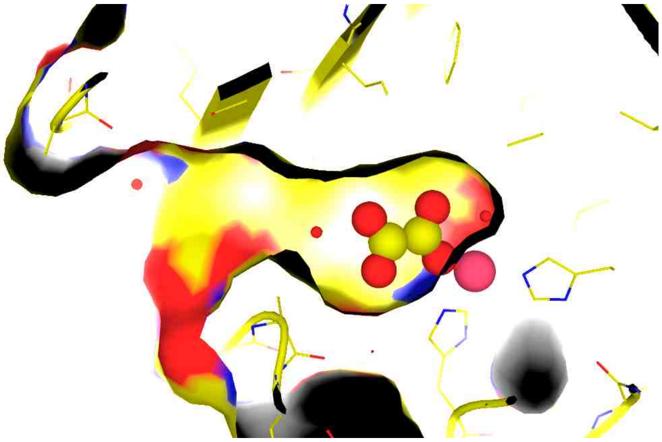

(b) N-terminal tunnel with oxalate

Figure 4.36. The crystal structure shows oxalate bound in the N-terminal metal binding site of the ΔE162 variant. Figrue(a) was prepared by L. M. Easthon.

chased from Cambridge Isotope Laboratories (Andover, MA). (Z)-1-(N-methyl-N-[6-(N-methylammoniohexyl)amino]diazen-1-ium-1,2-diolate (MAHMA NONOate) was obtained from Cayman Chemical (Ann Arbor, MI). Plasmid miniprep kit was pur-

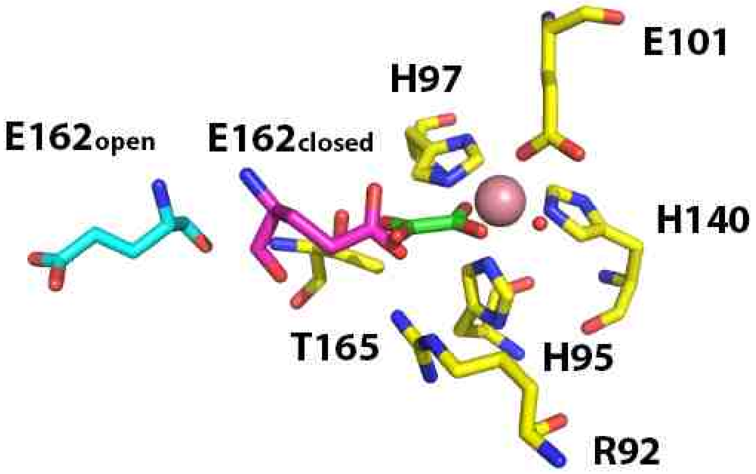

Figure 4.37. Superimpose the structure of the ΔE162 (yellow) with the open (cyan) and closed (magenta) form WT OxDC structure. Figrue(a) was prepared by L. M Easthon.

chased from Zymo Reasearch. α-phenyl N-tertiary-butyl nitrone (PBN) was obtained from Alexis Biochemicals (San Diego, CA). Oxalate assay kit for KIEs experiment was purchased from Trinity Biotech USA (Jamestown, NY). Nickel-nitrilotriacetic acid agarose (Ni-NTA) was supplied by Qiagen (Germantown, MD). DNA primers were synthesized by Integrated DNA Technologies, Inc. (Coralville, IA) and DNA sequencing was performed in the DNA Sequence Core at the University of Michigan (Ann Arbor, MI) and Interdisciplinary Center for Biotechnology Research (ICBR) at the University of Florida (Gainesville, FL). Protein concentrations were determined using the CoomassiePlus Protein Assay reagent obtained from Thermo Fisher Scientific (Waltham, MA), and BT Chelex 100 resin was purchased from Bio-Rad (Hercules, CA). ICP-MS measurements of metal content were carried out at the Center for Applied Isotope Studies at the University of Georgia (Athens, GA).

4.4.1 Site-direct Mutagenesis

DNA primers were designed and purchased from Integrated DNA Technologies, Inc. (Coraville, IA). The C-terminally His$_6$-tagged *B. subtilis* WT OxDC gene in the pET-32a vector and the gene of the DASN variant were generously provided by Dr. Stephen Bornemann (John Innes Center, Norwich, UK). The genes of all the mutations in this chapter were obtained by PCR using the QuikChange method. The gene of the DASN variant was used as the template in the PCR for generation of the DESN and DSSN variants. The WT OxDC gene was used as the template in the PCR for generation of the mutations of DENS, AENS and ΔE162 variant. The mutation of DDNS was generated using the DENS gene as template. The primers used for mutagenesis in this chapter were listed in Table 4.11. The PCR was performed using the cycle showing ing Table 4.12. The PCR products were treated with *Dpn*I (New England Bio. Labs) and transformed into *E. coli* JM109 or Nova Blue competent cell for plasmid amplification. The sequence of genes were confirmed using the DNA sequencing service of Interdisciplinary Center for Biotechnology Research (ICBR) of the University of Florida and the DNA Sequencing Core of the University of Michigan.

4.4.2 Protein Expression and Purification

The sequenced genes were transformed into *E. coli.* BL21(DE3) for overexpression using previously established methods. [46] Briefly, cell culture was heat-shocked at 42 °C for 15 min once OD$_{600}$ had reached 0.4, followed by addition of 5 mM MnCl$_2$ and 0.8 mM IPTG to induce the overexpression of protein. Cells were harvested by centrifugation and lysed by sonication. The debris was removed by centrifugation and the soluble protein in supernatant was purified using Ni-NTA affinity chromatography. The elution fractions were pooled and dialyzed against storage buffer (50 mM Tris-HCl, pH 8.5, 500 mM NaCl) to remove imidazole. Proteins were concentrated to desired concentration using Amicon Ultra 30K centrifuge device (Millipore) and treated with Chelex-100 resin (Bio-Rad) to remove the free metal in the solution.

Table 4.11.
Primers used in the mutagensis study in this chapter

Primer	Sequence
DESN Fwd	5’-CGATGGATCATTCGATGAAAGCAACACGTTCCAGC-3’
DESN Rev	5’-GCTGGAACGTGTTGCTTTCATCGAATGATCCATCG-3’
DDSN Fwd	5’-CGATGGATCATTCGATGATAGCAACACGTTCCAGC-3’
DDSN Rev	5’-GCTGGAACGTGTTGCTATCATCGAATGATCCATCG -3’
DDNS Fwd	5’-GACGATGGATCATTCGATGATAACAGCACG-3’
DDNS Rev	5’-CGTGCTGTTATCATCGAATGATCCATCGTC-3’
DENS Fwd	5’-CGATGGATCATTCGATGAAAACAGCACG-3’
DENS Rev	5’-CGTGCTGTTTTCATCGAATGATCCATCG-3’
AENS Fwd	5’-GGATCATTCGCTGAAAACAGCACGTTCC-3’
AENS Rev	5’-GGAACGTGCTGTTTTCAGCGAATGATCC-3’
ΔE162 Fwd	5-GACGATGGATCATTCTCTAACAGCACGTTCCAGC-3’
ΔE162 Rev	5-GCTGGAACGTGCTGTTAGAGAATGATCCATCGTC-3’

Protein purity was estimated from the protein band on SDS-PAGE. Protein concentrations were determined using the Bradford assay, in which bovine serum albumin was used as the standard. The metal contents of the enzymes were determined using ICP-MS.

4.4.3 FDH Assay

Reactions were initiated (100 mM citrate buffer, pH 4.0, 125 mM NaCl, 300 μM *o*-PDA and 0-80 mM oxalate) by addition of enzyme at 25 °C, and quenched after 1 min by addition of 100 mM NaOH. The amount of formate produced was determined by coupled assay, which the production of formate was quantified via the conversion

Table 4.12.

PCR condition.

Step	Temperature	Time
1	95°C	4min
2	95°C	30sec
3	55°C	1min
4	68°C	7min 30s
5	go back to step 2	20 cycles
6	72°C	10min
7	4°C	hold

of NAD^+ to NADH by formate dehydrogenase in 50 mM phosphate buffer, pH 7.8 with 1.5 mM NAD^+ and 0.5 U FDH. The amount of NADH was measured at 340 nm using UV-Vis spectroscopy after 16 h incubation at 37°C.

4.4.4 ABTS-Peroxidase Assay

Reactions were initiated (50 mM succinate buffer, pH 4.0, 125 mM NaCl, 5 mM ABTS, 25 U HRP and 0.5-50 mM oxalate) by addition of enzyme at 25 °C. H_2O_2 was quantified by the absorption at 650 nm using UV-Vis spectrometry to measure ABTS radical cation produced during the oxidation of ABTS by H_2O_2. The initial rate was determined from the slope of A_650 vs time within 1 min. Control reactions, in which oxalate, OxDC or HRP was eliminated from the reaction mixture were required, because oxalate is able to reduce the ABTS radical cation to ABTS in the presence of manganese, while as reported previously OxDC has oxalate-dependent single electron transfer dye oxidation activity. The pH profile of the DASN variant was determined using the standard peroxidase-ABTS coupled assay except that reactions were performed in phosphate-succinate buffer from pH 3.5-7.0. Measurements were determined by standard computer-based methods, and the data were analyzed to obtain the values of V/K.

4.4.5 MIMS Experiments

MIMS assay measured CO_2 production and O_2 consumption. These assays were performed using an Extrel EXM-200 quadrupole mass spectrometer with an inlet probe. Solutions containing 0-100 mM $^{13}C_2$-oxalate, 50 mM succinate buffer, pH 4.0, and 125 mM NaCl were equilibrated with air, O_2 or helium. Reactions were initiated by addition of enzyme to the reaction mixture. The ion current of the ^{13}CO2 and other neutral small molecules were measured in real-time. The standard curve is needed for converting the ion current directly obtained from the MS to molarity. Briefly, various known volumes of 10 mM K_2CO_3 were added to degassed 50 mM acetic acid, pH 2.0, in the reaction chamber and the ion current 44 and 45 was recorded. Since at this pH, the addition of ${CO_3}^{2-}$would turn into CO_2 very quickly, the relationship between the CO_2 concentration and ion current can be determined. In order to obtain the standard curve of O_2, known volumes of O_2-saturated water were added into the water. Based on the solubility of O_2 at 25°C at atmospheric pressure, the concentration of O_2 in the reaction chamber was calculable, thus the relationship between the known O_2 concentration and the ion current can be determined. The degassed solution was obtained by purging helium into the reaction buffer for 45 min at 25°C under atmospheric pressure. For the data analysis of MIMS assay, after plotting the time *verse* ion current, the initial velocity was determined from the slope of the linear part of CO_2 production signal after the initiation of the reaction. Since no O_2 would be consumed when the enzyme undergoes OxDC activity, in a similar manner, OxOx activity can be determined using the linear portion of O_2 consumption curve, which ideally all arises from OxOx activity of the enzyme. However, because of the vacuum in the inlet, some of gas could be lost during the measurement. A blank reaction was therefore performed and subtracted from all the experimental measurements to correct for the effect of the gas loss. For the NO experiments, MAHMA was dissolved in 0.01 M NaOH and added into the degassed reaction mixture at pH 4.0, where it rapidly decomposed into NO. The signal of m/z 30 indicated the amount of NO in the solution. Then a known volume of O_2 saturated water was added into the reaction mixture. Based on the solubility of the O_2 in water, the concentration of O_2 in the system can be calculated. Once the O_2 signal reached equilibrium, the protein solution was quickly injected into solution. The signals m/z 30, m/z 32 m/z 45 and m/z 31 indicated the amount of NO, O_2 $^{13}CO_2$ and HNO respectively in the solution.

4.4.6 KIEs Experiments

$^{13}(V/K)$ represents the ratio of V_{max}/K_M for the ^{12}C-containing substrate relative to the ^{13}C-containing substrate. Isotope ratio mass spectroscopic (IRMS) analysis of CO_2 by the internal competition method, was used to measure the primary ^{13}C kinetic isotope effect (IE) for the conversion catalyzed by the DASN variant. Natural abundance levels of ^{13}C were present in the carbon atoms of oxalate used in these experiments. The analyses to determine the isotopic ratios (R values) were performed on CO_2 isolated directly from the DASN-catalyzed partial conversion of oxalate. Enzymatic reactions were performed by incubation of the DASN variant with oxalate (1 mM) at 25 °C in either 50 mM 1,4-bis-(2- hydroxyethyl)piperazine, pH 4.2, or 50 mM piperazine, pH 5.7. All gases were passed over Ascarite to remove CO_2 prior to use, and the buffers were sparged with N_2. Since the presence of O_2 is required for OxOx activity but high concentrations of O_2 inhibits the DASN variant, equal volumes of O_2-saturated water (10 mL) and degassed buffer were mixed to give the final reaction mixture of approximately 680 μM O_2 concentration (20 mL total volume). Reactions were initiated by addition of enzyme, and quenched by raising the solution pH to 7.5 using either 1 N Tris-H_2SO_4 buffer, pH 7.8 (reaction set for pH 4.2), or 1 N Tris-H_2SO_4 buffer, pH 7.5 (reaction set for pH 5.7), after 2 h and 4 h, respectively.

The CO_2 that was collected. The quenched reaction mixture was filtrated through an Amicon ultrafiltration system to remove the residual enzyme in the solution, and an aliquot (50 μL) taken to determine the fraction of conversion, f. Any production of formate was determined using the FDH assay. The residual oxalate was detected using the oxalate detection kit (Trinity Inc.). In this assay, OxOx in the commercial kit converts the oxalate in samples into H_2O_2, and the coupling organic dye is oxidized by H_2O_2 producing a blue color which can be detected by UV-Vis. H_2O_2 produced from the DASN variant catalyzed reaction could interfere with the reagent in the oxalate assay from the commercial detecting kit. Therefore catalase (10 μL, 10000 U/mg) was added to the aliquots of the reaction to remove H_2O_2. This was followed by trichloroacetic acid precipitation to inactivate catalase. The residual oxalate in the aqueous phase was then determined using oxalate detection kit.

4.4.7 Spin-trapping Experiments

Spin trapping experiment was performed at room temperature using PBN as the spin trap reagent. Reactions were initiated by adding enzyme (28 μM for WT, 19 μM for DASN, 20 μM for ΔE162 and 40 μM for DESN) and 50 mM oxalate into a quartz capillary containing 50 mM citrate buffer, pH 4.0, 0.2 mM diethylene triamine pentaacetic acid (DTPA) and 75 mM PBN in quartz capillary. The concentration of trapped radical was estimated using 25 μM 2,2,6,6-tetramethyl-1-piperidinyloxy (TEMPO) as a standard. Instrumental parameters were: 9.87 GHz microwave frequency, 2 G modulation amplitude, 3512 G magnetic fields, 60 G sweep width, 81.92 ms time constant, 81.92 ms conversion time/point, and 60 dB receiver gain.

4.4.8 X-band EPR Experiments

Protein samples were stored in 50 mM Tris buffer, pH 8.5 with 500 mM NaCl. Samples were directly mixed with the same volume of glycerol for the measurement at pH 8.5. For the measurements at acidic pH, the protein samples containing 20%

glycerol were adjusted to pH 4.0 by adding 1 M citrate buffer, pH 4.0, with 5% glycerol. Samples used in perpendicular or parallel mode X-band EPR spectroscopy were fast-frozen in liquid N_2 before loading to instrument. The experiments were performed at 5 K, using a Bruker Elexsys model E580 spectrometer. In the time course experiment of EPR measurement, the reaction was initiated by addition of 0.5 M oxalate, pH 4.0 into the EPR tube at room temperature with the protein sample that had been premixed with 50% glycerol in pH 4.0 buffer. After 5 sec reaction in room temperature, the sample was quenched by rapid-frozen in liquid N_2 for 1 min. Time course perpendicular mode data and parallel mode data were collected every 15 sec-10 min for the same sample depending on the variant, and four scans were recorded for each time point. A spectrum of the buffer without enzyme was recorded as the background. Instrumental parameters were: 10 G modulation amplitude, 3550 ± 3500 G magnetic fields, 4 ms time constant, and 60 dB receiver gain. time constant, and 60 dB receiver gain.

5. CHARACTERIZATION OF THE SECOND SHELL RESIDUES IN METAL BINDING SITES OF OXDC

5.1 Introduction

The manganese ions of OxDC are coordinated with the identical residues in both metal binding sites (Fig.1.3). These residues are the first shell residues, and mutations on these residues directly affects metal loading. [55] Second shell residues are defined as the residues that interact with the metal ligands (Fig. 1.2). Although these residues do not directly coordinate manganese, they affect enzyme activity and metal properties as shown in previous kinetic and high-field EPR studies. [99] For example, Trp132 in the N-terminal domain of OxDC forms a hydrogen bond with the metal ligand, Glu101, and it is likely that the interaction between Glu101 and Trp132 contributes to OxDC activity by affecting the electron distribution on Glu101.

The W132F variant was designed to disrupt this interaction between the first shell residue Glu101 and the second shell residue ,Trp132, in the N-terminal site. [99] The high-field EPR spectrum of the W132F variant exhibited increased zfs at high pH in the absence of oxalate. Structural studies on this OxDC variant show that the mutation has no effect on either the coordination of metal or the geometry of the other residues in the active site. [99] Therefore, changes in kinetic parameters and hyperfine structure reported in the literature must result from different electronic properties of manganese in the variant compared to WT OxDC. Further studies on this mutant were undertaken to examine how the enzyme might utilize specific residues to manipulate catalysis.

In the C-terminal metal binding site, the second shell residue, Gln282, occupies the corresponding position to Trp132. The absence of tryptophane residue in the C-terminal site similar to that of Trp132 could possibly be one of the reasons why C-terminal site is not catalytically active. The Q282W variant could possibly introduce a similar hydrogen binding interaction between the tryptophan residue and the C-terminal metal gain activity in the Q282W variant.

5.2 Results and Discussion

5.2.1 Steady-state Kinetics of the W132F and Q282W Variants

The W132F and Q282W variants were expressed using standard protocols. The metal content of the two variants were similar to that of WT OxDC, indicating that mutations of the second shell residues do not affect the metal loading at either metal binding site in the protein. Standard assays and MIMS were used to determine the steady-state kinetic parameters for the W132F and Q282W variants. (Table 5.1) The W132F protein exhibited a 12-fold increase in K_M compared to WT OxDC, and a 6-fold decrease in the $k_{cat}/K_M/\text{Mn}$ value. The K_M of the Q282W variant was the same as for WT OxDC, while the $k_{cat}/K_M/\text{Mn}$ of the Q282W variant was 1.4-fold higher. According to the crystal structure of the cobalt substituted W132F variant, mutation at residue 132 has no significant effect on the location of other residues in the N-terminal metal binding site. Thus, the loss of the hydrogen bind between Glu101 and Trp132 must make a contribution to changes in the steady-state kinetic parameters of the W132F variant.

Although the N-terminal metal binding site of the Q282W variant was not affected, the slightly higher k_{cat} value of this variant could be attributed to the mutation at the C-terminal metal binding site. This observation is intriguing since only the N-terminal site is thought to be catalytically active. [46] The Q282W variant may indeed introduce a hydrogen bond between the metal ligand, Glu280, and the second shell residue 282. It remains unclear whether the increase in activity was due to the C-

Table 5.1.
Kinetic parameters of the W132F and Q282W variants measured by MIMS.

Enzymes	K_M (mM)	k_{cat}/K_M/Mn ($M^{-1}s^{-1}$)	Mn content (Mn/monomer)
WT	2 ± 0.4	10000 ± 1000	1.5
W132F	24 ± 2	1700 ± 100	1.8
Q282W	2 ± 0.2	14000 ± 2000	1.6

terminal site gaining activity or the mutation increased activity in the N-terminal active site.

5.2.2 EPR Spectroscopy of the W132F and Q282W Variants

The W132F Variant

The W132F variant was designed to interrupt the hydrogen binding between Trp 132 and Glu101, which presumably could affect the electronic environment of the manganese. Perpendicular mode and parallel mode EPR spectra for the W132F were acquired under various pH conditions in the presence or absence of oxalate.

The EPR spectrum of the W132F variant under perpendicular mode exhibited no significant differences compared to WT OxDC (Fig. 5.1). As observed in the EPR spectrum of WT OxDC, pH changes affected spectrum feature at $g = 4.3$ and the broad signal on each shoulder of the sextet signal of M_s = -1/2 $\longleftrightarrow$ +1/2 transition. The signal at $g = 4.3$ was adding indicative of a change from penta-coordinate to the hexa-coordinate geometry about the manganese ions. The broad signal appearing on the shoulder of the $g = 2.0$ signal was assigned to the C-terminal Mn site under acidic conditions as in the previous HFEPR study. [49]

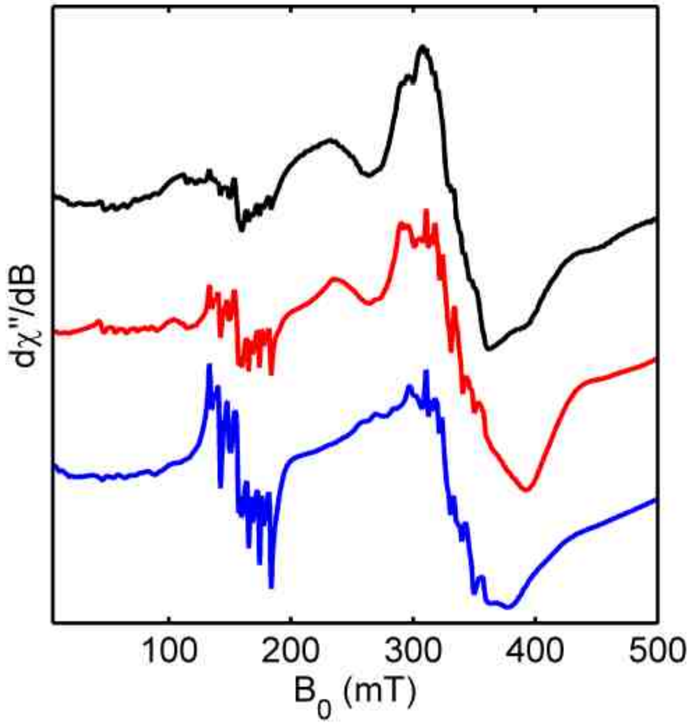

Figure 5.1. Perpendicular mode EPR spectra of W132F in the absence of oxalate at pH 8.5 (Blue), pH 5.7 (Red) and pH 4.2 (Black). Figure was prepared by Dr. J. Wilcoxen.

In the parallel mode EPR spectrum of the W132F variant, a substantial change was observed under basic condition (Fig. 5.2). Specifically, A Mn(III) signal appeared in the W132F variant at pH 8.5. These signal is the only Mn(III) signal that has been observed under basic conditions for OxDC and many of its variants. Based on the crystal structure, [99] the W132F variant does not perturb metal coordination in the C-terminal metal binding site, thus the new signal for Mn(III) is likely associated with Mn in the N-terminal domain. The signal centered at 135 mT arises from the forbidden-transition of Mn(II) and was similar to that seen in the parallel mode EPR spectrum of WT OxDC when oxalate was present under acidic conditions. When the pH of the solution was adjusted to pH 5.7 and pH 4.2, the Mn(III) signal in the W132F variant disappeared, and the intensity of the forbidden-transition was reduced. This can be explained by restoration of the hydrogen bond between Glu101 and a water molecule in the N-terminal metal binding site when the pH of the solution was lowered. Thus, the spectra of the W132F variant at low pH are similar to those of WT OxDC. This also suggests that the electron environment around the manganese of the W132F variant is similar to that of WT OxDC at the catalytically active pH in the absence of substrate.

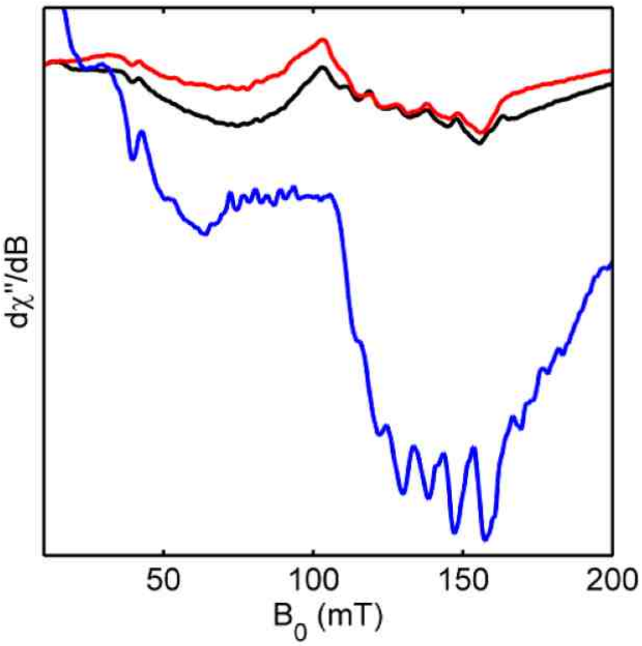

Figure 5.2. Parallel mode EPR spectra of W132F in the absence of oxalate at pH 8.5 (Blue), pH 5.7 (Red) and pH 4.2 (Black). Figure was prepared by Dr. J. Wilcoxen.

In the presence of oxalate, perpendicular mode EPR spectrum of the W132F variant exhibited no significant differences compared with the spectra of WT OxDC under the same conditions (Fig. 5.3). The Mn(II) signal again indicated a mixture of different Mn coordinations. A sharp signal at $g = 2.0$ (previously assigned as the tyrosyl radical) [91] also appeared in spectrum of the sample at pH 5.7.

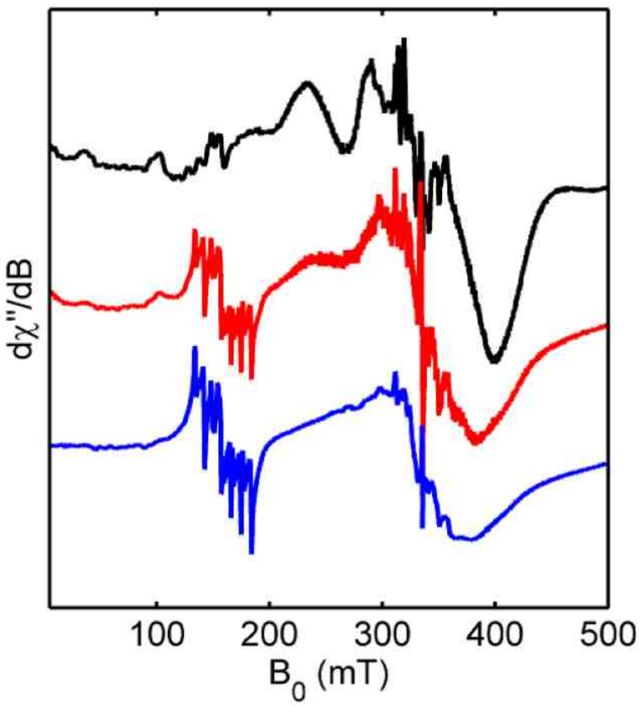

Figure 5.3. Perpendicular mode EPR spectra of W132F in the presence of oxalate at pH 8.5 (Blue), pH 5.7 (Red) and pH 4.2 (Black). Figure was prepared by Dr. J. Wilcoxen.

In previous studies, [91] the intensity of the tyrosyl radical increased in the first 10 min after the addition of oxalate to the WT enzyme, and after this time, the signal started to decay. The most likely explanation for the source of tyrosyl radical is a protein-based radical, although, mutations of several conserved tyrosines in the enzyme have failed to identify location of the tyrosyl radical and the change in signal intensity was slower than the production rate of formate. [91] There is no evidence to support the hypothesis that the tyrosyl radical is involved in catalytic mechanism.

For the W132F variant, the strongest intensity of the tyrosyl radical was observed in the presence of oxalate at pH 5.7, while a weak radical signal appeared for the oxalate-added solution at pH 8.5. The radical intensity at pH 4.2 was the smallest among the three conditions. Compared to the experimental conditions in the previous study, [91] the enzyme concentration was 37-fold higher than the sample reported in literature while the formation of the tyrosyl radical has been observed at pH 5.2 in the literature. [91] It is possible that optimal conditions for formation of tyrosyl radical are not the same as those for decarboxylase activity. Furthermore, the radical signal at pH 8.5 suggests that formation of tyrosyl radical is a side reaction that occurs independently under conditions that the enzyme cannot catalyze the decarboxylation reaction. The absence of tyrosyl radical from the pH 8.5 solution without oxalate also suggests that the presence of oxalate contributes to the formation of the tyrosyl radical,as seen previously. [91]

In parallel mode EPR, a Mn(III) signal appeared when oxalate was added to the W132F variant reaction mixture at pH 4.2, even though spectra at pH 5.7 and pH 8.5 did not show a Mn(III) signal in the presence of oxalate (Fig. 5.4), Addition of oxalate into the pH 8.5 sample eliminated the Mn(III) originally seen in the spectrum of free enzyme at this pH. Changing the pH likely affect the protonation state of residues in the metal binding site and the geometry of metal coordination, thus preventing formation of Mn(III).

The Q282W Variant

Both perpendicular mode (Fig. 5.5) and parallel mode EPR spectra(Fig. 5.6) for the Q282W variant were similar to those of WT OxDC, indicating similar metal coordination in the two proteins at all pH values. In oxalate-containing samples, the tyrosyl radical signal appeared to be more intense for the Q282W variant than for WT OxDC, although other features of these perpendicular mode spectra (Fig. 5.8) and the parallel mode spectra (Fig. 5.9) of the Q282W variant were almost identical to those seen in the spectra of WT.

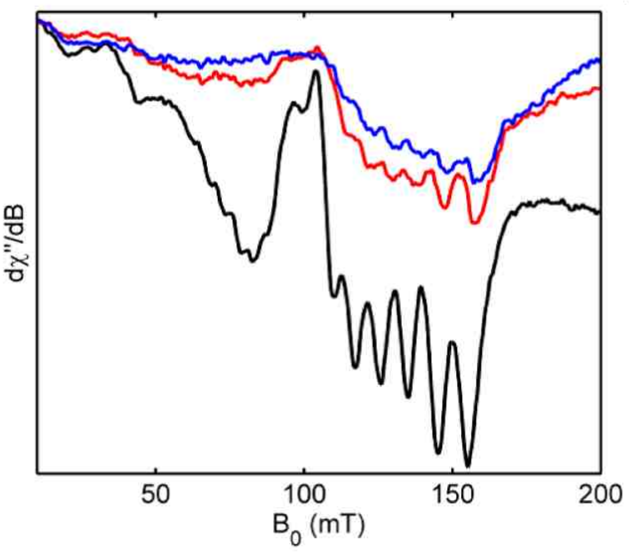

Figure 5.4. Parallel mode EPR spectra of W132F in the presence of oxalate at pH 8.5 (Blue), pH 5.7 (Red) and pH 4.2 (Black). Figure was prepared by Dr. J. Wilcoxen.

The mutation was designed to introduce a Trp-Glu hydrogen bond in the C-terminal metal binding site so as to mimic the N-terminal site. The electronic environment around the manganese ion in the C-terminus was still different when compared to the N-terminal site. Glu333 in the C-terminal metal binding site was proposed to coordinate manganese in bidentate fashion at low pH in previous high-field EPR study. [49] Therefore, multiple species differeing in manganese coordination were expected for the Q282W variant. It is possible that the increased activity seen for the Q282W variant arises from activation of the C-terminal site by the mutation. This arises questions about the identity of the general acid/base in the C-terminal site that facilitates any proton-coupled electron transfer step. Therefore, observation that the Q282W variant activates the C-terminal metal binding site still requires further investigation.

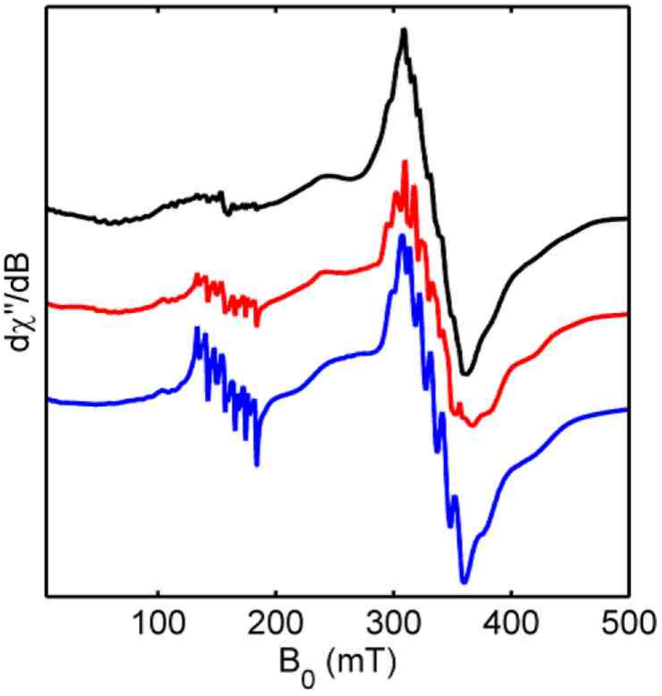

Figure 5.5. Perpendicular mode EPR spectra of the Q282W variant in the absence of oxalate at pH 8.5 (Blue), pH 5.7 (Red) and pH 4.2 (Black).Figure was prepared by Dr. J. Wilcoxen.

5.2.3 KIEs Measurements for the W132F Variant

Heavy Atom KIEs Determination

Heavy atom kinetic isotope effects were successfully utilized to probe the catalytic mechanism for WT OxDC and the DASN variant. The simplified minimal mechanism described in Chapter 2 includes the possible steps from the substrate binding up to the first irreversible step of the decarboxylation of oxalate was used to interpret KIEs determined for the W132F variant (Fig. 2.7).

Kinetic isotope effect measurements were performed on the W132F variant to determine the effect on catalysis caused by removing the hydrogen bond between Trp132 and Glu101. Primary ^{13}C and secondary ^{18}O IEs were determined at pH 4.2

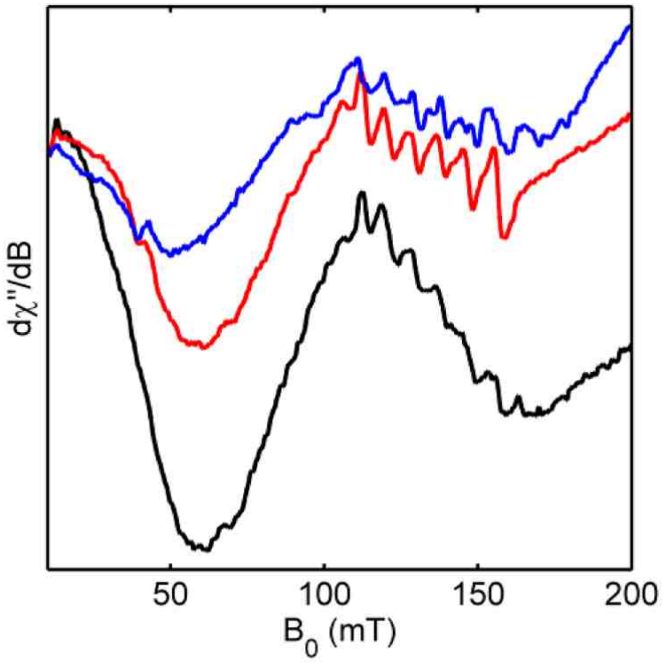

Figure 5.6. Parallel mode EPR spectra of the Q282W variant in the absence of oxalate at pH 8.5 (Blue), pH 5.7 (Red) and pH 4.2 (Black). Figure was prepared by Dr. J. Wilcoxen.

and pH 5.7 using a modified protocol to that reported for the IE experiments on WT OxDC. Oxalate with natural abundance isotopic composition was used as the substrate. $^{x}(V/K)$ values of ^{13}C and ^{18}O for formate and CO_2 were calculated using equation (4) in Chapter 2. (Table 5.2)

The decarboxylation step exhibited ^{13}C IEs of 1-1.3% on CO_2 in the W132F variant catalyzed reaction, which is 2-fold larger than that for WT OxDC (0.5-0.8%), suggesting that the oxalate radical anion intermediate has a lower forward commitment than going back to the Michaelis complex than that of WT OxDC. Previous studies on other decarboxylases gave 3-5% IEs on CO_2 when the decarboxylation was the sole rate-determining step. Thus, the decarboxylation step in the W132F variant is only partially rate-limiting. On the other hand, ^{13}C IEs (2.6-3.6 %) on

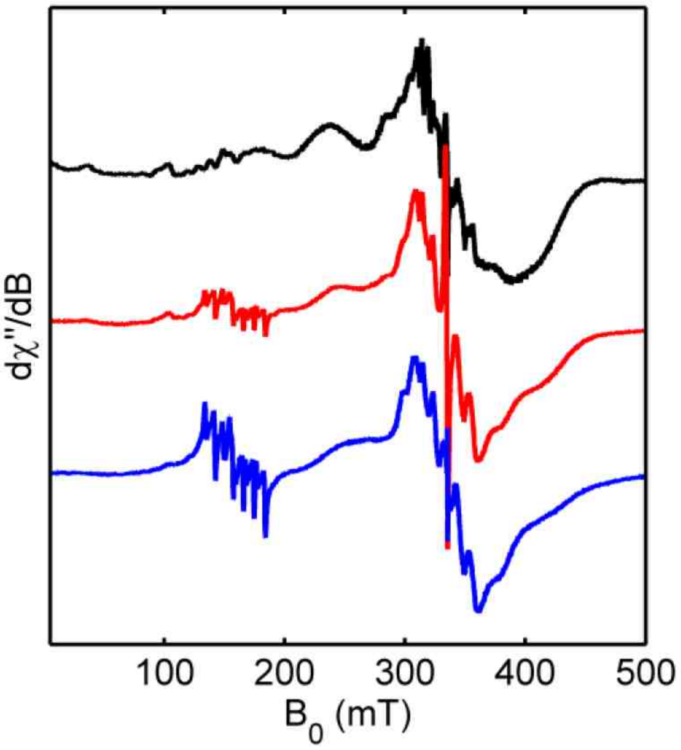

Figure 5.7. Perpendicular mode EPR spectra of the Q282W variant in the presence of oxalate at pH 8.5 (Blue), pH 5.7 (Red) and pH 4.2 (Black). Figure was prepared by Dr. J. Wilcoxen.

formate were substantial in the W132F variant being 2-fold larger than those for WT OxDC (1.5-1.9%). This suggests that both the decarboxylation step and the reversible step for the W132F variant have decreased commitments to catalysis. The reversible proton-coupled electron transfer step, however, remains more rate-limiting than decarboxylation in the W132F variant.

The ^{18}O IEs on CO_2 for the W132F variant were larger than those for WT OxDC,. which can be interpreted as the C-C bond cleavage having reduced commitment to catalysis in the variant. The inverse IE is the result of the change in single C-O bond in oxalate to doubly bonded oxygen in CO_2. The^{18}O IE on formate production by the W132F variant exhibited an increased pH-dependence (1.4 *v.s.* 1.0) suggesting a

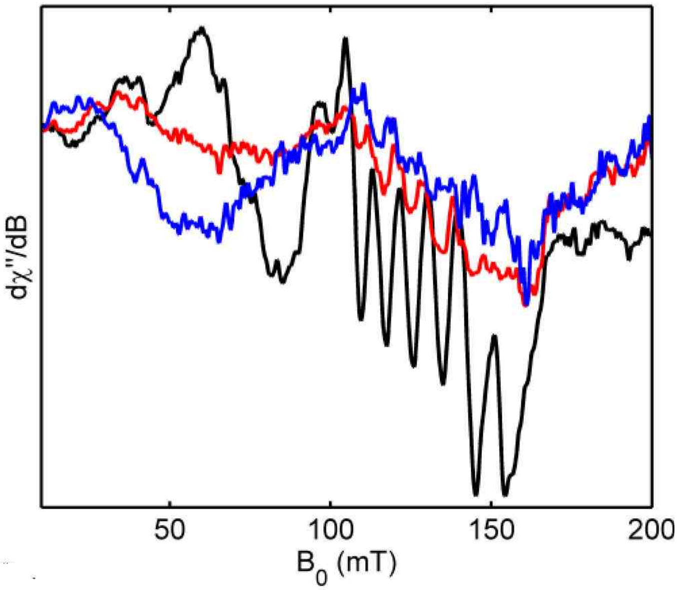

Figure 5.8. Parallel mode EPR spectra of the Q282W variant in the presence of oxalate at pH 8.5 (Blue), pH 5.7 (Red) and pH 4.2 (Black). Figure was prepared by Dr. J. Wilcoxen.

Table 5.2.
Heavy atom kinetic isotope effects on the OxDC reaction catalyzed by WT OxDC and the W132F variant

		$^{13}(V/K)$		$^{18}(V/K)$	
Enzyme	pH	CO_2	HCO_2^-	CO_2	HCO_2^-
WT	4.2	1.005 ± 0.001	1.015 ± 0.001	0.998 ± 0.002	1.011 ± 0.002
W132F	4.2	1.008 ± 0.001	1.024 ± 0.001	0.993 ± 0.001	1.009 ± 0.001
WT	5.7	1.008 ± 0.001	1.019 ± 0.001	0.993 ± 0.002	1.010 ± 0.001
W132F	5.7	1.013 ± 0.001	1.036 ± 0.001	0.989 ± 0.002	1.014 ± 0.002

change in external commitment at different pH values. In order to exclude oxygen exchange from solvent (water) to substrate, product, or intermediate, a control experiment with 2% H^{18}_2O was performed under the same conditions at pH 4.2. The observed KIEs were the same as those in the sample that contained unlabled H_2O, indicating that no exchange of oxygen occurred during the measurement during sample preparation.

Data Analysis

Using the same analysis method [61] that was reported for WT OxDC. The observed IEs observed for the formation of CO_2 and formate were interpreted using equation (2.5) (Chapter 2). More specifically, assuming only k_3, k_4 and k_5 were the isotope sensitive steps, the equation for IEs on V/K for CO_2 and formate can be expressed in following equations:

$$^{13}(V/K) = \frac{^{13}K_{eq3}{}^{13}k_5 + {}^{13}k_3(\frac{k_5}{k_4}) + \frac{k_3k_5}{k_2k_4}}{1 + (\frac{k_5}{k_4})(1 + \frac{k_3}{k_2})} \tag{5.1}$$

$$^{18}(V/K) = \frac{^{18}K_{eq3}{}^{18}k_5 + {}^{18}k_3(\frac{k_5}{k_4}) + \frac{k_3k_5}{k_2k_4}}{1 + (\frac{k_5}{k_4})(1 + \frac{k_3}{k_2})} \tag{5.2}$$

Based on current ideas that 1) the unprotonated carboxyl group in monoprotonated oxalate binds to manganese and 2) the proton on the protonated carboxyl group is removed in step prior to the decarboxylation step, three assumptions can be made as in the previous study [61] for interpreting the ^{13}C IEs on CO_2 at pH 5.7: (i) k_3/k_2 is small, (ii) the decarboxylation IE on the CO_2 $^{13}k_5$ is 1.04 which is a average value for decarboxylation reaction and (iii) $^{18}K_{eq3}$ and $^{13}k_3$ are both unity. Therefore:

$$^{13}(V/K) = \frac{1.04 + (k_5/k_4)}{1 + (k_5/k_4)} = 1.013 \tag{5.3}$$

$k_5/k_4 = 2.08$ can be obtained from equation 5.3. For ^{13}C IEs on formate at pH 5.7, three assumptions were again made as [61] in order to estimate the $^{13}K_{eq3}$: (i)

$k_5 = 1.03$ is normal as in other decarboxylation reactions, (ii) k_3/k_2 is small and (iii) ${}^{13}k_3$ is the average of ${}^{13}K_{eq3}$ and unity. Therefore,

$$^{13}(V/K) = \frac{(1.03)^{13}K_{eq3} + (2.08)\frac{^{13}K_{eq3}+1}{2}}{1 + 2.08} = 1.036 \tag{5.4}$$

The value of ${}^{13}K_{eq3}$ was calculated as 1.04. The ^{13}C fractionation factor of oxalate relative to CO_2 has been reported to be 0.9838. When ${}^{13}K_{eq3}$ was divided by 0.9838, the corresponding C-O bond order was 0.9, as calculated using equation (2.4) and (2.5) (Chapter 2).

Protonation of the carboxyl group affects the ^{18}O IEs. Since the pH profile of WT OxDC indicated that monoprotonated oxalate was the substrate [61], the equilibrium ^{18}O IEs for protonation of one end of the oxalate was taken into consideration.

At pH 5.7, at which almost all oxalate exists as the dianion, oxalate needs to be protonated before binding. This would lead to a 2% enrichment of the ^{18}O at the carboxyl group that becomes protonated, resulting in the ^{18}(V/K) at this end of carboxyl group requiring correction by 0.98. Although oxalate itself is a symmetrical molecule, after binding with the manganese, isotope substitution is either be at the carboxyl group that binds to manganese or becomes protonated.

At pH 5.7, for the ^{18}O IE on CO_2, based on the minimal mechanism, five assumptions were made: [61] (i) ${}^{18}(V/K)$ needs to be multiplied by a factor of 0.98, (ii) k_3/k_2 is small, (iii) the estimated ${}^{18}K_{eq5}$ =0.967, which is based on fractionation factor calculations, (iv) the decarboxylation IE on CO_2 is midway between ${}^{18}K_{eq5}$ and unity, and (v) ${}^{18}K_{eq3}$ =1.02 due to the effect of removing a proton in the first step. Therefore:

$$^{18}(V/K) = \frac{0.98[(1.02)(\frac{0.9835+1}{2}) +^{18} k_3(2.077)]}{1 + 2.077} = 0.989 \tag{5.5}$$

This equation gives ${}^{18}k_3 = 1.01$. At pH 5.7, for the ^{18}O IE on formate, three assumptions were made: (i) k_3/k_2 is small, (ii) the decarboxylation IEs on formate is midway between ${}^{18}K_{eq3}$ and unit, and (iii) ${}^{18}k_5$=1.003, because the formate radical loses a bending mode. Therefore:

$$^{18}V/K = \frac{(1.003)(^{18}K_{eq3} + (2.08)^{\frac{^{18}K_{eq3}+1}{2}})}{1 + 2.08} = 1.014 \tag{5.6}$$

Solving this equation gives $^{18}K_{eq3} = 1.02$.

At pH 4.2, for ^{13}C IEs on CO_2, four assumptions were made: [61] (i) k_3/k_2 is not negligible, (ii) the decarboxylation IE $^{13}k_5$ is 1.04, (iii) k_5/k_4 is the same as that at pH 5.7, and (iv) $^{13}K_{eq3}$ and $^{13}k_3$ are both unity. Therefore:

$$^{13}(V/K) = \frac{(1.04) + (2.077)(1 + \frac{k_3}{k_2})}{(1 + (2.077)(1 + \frac{k_3}{k_2})} = 1.01 \tag{5.7}$$

Solving this equation gives $k_3/k_2 = 0.44$.

At pH 4.2, for the ^{18}O IE on CO_2, five assumptions were made: [61] (i) k_3/k_2 is not negligible, (ii) the decarboxylation IE on CO_2 is midway between $^{18}K_{eq3}$ and unity (0.9835), (iii) k_5/k_4 and $^{18}K_{eq3}$ are the same as those at pH 5.7, (iv) $^{18}K_{eq3} = 1.02$, and (v) the correction factor for deprotonation from monoprotonated oxalate is 0.99 since only 50% of the oxalate is in the mono-protonated form at this pH. Therefore:

$$^{18}(V/K) = \frac{0.99[(1.02)(\frac{0.967+1}{2}) + (1.012)(2.077) + (2.077)\frac{k_3}{k_2}]}{(1 + 2.077)(1 + \frac{k_3}{k_2})} = 0.993 \tag{5.8}$$

This equation gives $k_3/k_2 = 3.01$.

The calculated $^{13}(V/K)$ on formate was 1.027 which was close to the experimental value of 1.026 at pH 4.2 when using the calculated $^{13}k_3$, k_3/k_2, k_5/k_4, and $^{13}K_{eq3}$ values in equation (5.1), thereby validating the model.

Using this quantitative analysis as the partition ratio k_5/k_4 calculated for the W132F variant was 2, which is 2-fold less than that of WT OxDC. This suggests that in the W132F variant, either the decarboxylation step, k_5, proceeds with a slower rate or the radical anion intermediate reverts to the Michaelis complex, k_4, with a faster rate.

^{13}C and ^{18}O fractionation factors were calculated from $^{13}K_{eq3}$ and $^{18}K_{eq3}$ values. Based on the previously reported data, [61] the relationship between the fractionation factor and the bond order was determined to be linear. Equations (2.4) and (2.5) were used to calculate the C-O bond order in the transition state for decarboxylation. These values were calculated to be 0.9 and 1.1 using the data obtained from ^{13}C and ^{18}O, respectively. The average bond order, 1.0, is lower than that in WT (1.15), indicating that the resonance structure I for the oxalate radical anion is, surprisingly, essentially 100%, in which a positive charge is located on the carbon that becomes into formate (Fig. 5.11). A more polarized C-O bond in the Mn bound carbonyl group therefore exists for W132F decarboxylation compared to WT.

[redacted]

Figure 5.9. The resonance structure of the transition state in the W132F-catalyzed reaction

Assuming that k_5/k_4 stays the same at different pH conditions, as in the WT OxDC IEs analysis, k_3/k_2 calculated from ^{13}C IE is 0.44, which is 2-fold less than that of WT. This suggests that the substrate dissociates more often from the enzyme than it proceeds to form the intermediate oxalate radical species.

Mechanistic Interpretation of the W132F variant

The increased IEs (Table 5.2) of the W132F variant provides evidence that the chemical steps in the W132F-catalyzed reaction are more rate-limiting compared to those of WT OxDC. The ^{13}C IEs measured for the bond breaking C-C cleavage giving a CO_2 range from 0.8-1.3 %. The more inverse ^{18}O IEs on forming CO_2 confirmed this result. The modification in the electronic structure of the metal caused by removing the Trp132-Glu101 hydrogen bond resulted in substantial ^{13}C IEs of 2.4-3.6 % on the putative proton-coupled electron transfer step.

The proposed transition state structure of oxalate anion in the W132F variant is very polarized, with a full positive charge being located on the carbon of the oxalate anion radical becomes formate. Arg92 might possible stabilize this positive charge during catalysis, with polarization of the C-O bond facilitating decarboxylation. In an IE study of R92K OxDC, [48] a 2-fold lower partition ratio k_5/k_4 was consistent with a less polarized oxalate radical anion, giving rise to a decrease in the decarboxylation rate. However, for the W132F variant, this rate, k_5, should be fast due to the positive charge on the carbon. The rate of the anion radical intermediate reverting to the Michaelis complex, k_4, must therefore increase substantially. The transition-state for decarboxylation with a polarized intermediate should be earlier on the reaction coordinate than that for WT, giving a larger IE.

The partition ratio k_3/k_2 was also lowered to 0.44 compared to WT (0.75) , suggesting that substrate dissociates from enzyme more often than goes forward. Perhaps binding for oxalate is less favored due to the lack of hydrogen bonding between Trp132 and Glu101 resulting in an increased k_2. The value of $^{18}k_3$ is smaller than for WT enzyme (1.0159) suggesting the transition state for protein transfer is earlier in the W132F variant.

According to the KIEs study of the W132F variant, both proton-coupled electron transfer and decarboxylation steps become more rate-limiting for this mutant with formation of the putative oxalate radical anion being more rate-limiting compared to decarboxylation.

5.3 Conclusion

Mutations of second shell residues, W132F and Q282W, manipulate activity by altering interaction with manganese in the enzyme. Loss of the hydrogen bond between Glu101 and Trp132, W132F not only changed the oxidation state of the manganese in the resting enzyme at pH 8.5, but also affected the steady-state kinetics under acidic condition. The functional role of Trp132 in catalysis of OxDC may be to alter the electronic environment of the N-terminal manganese through an interaction with the metal ligand Glu101, thereby stabilizing the oxalate radical intermediate and encouraging decarboxylation step. In addition, the increased activity in the C-terminal mutation Q282W suggests that enzyme activity can be affected by the electronic environment of the manganese ion in the C-terminal domain. However, X-band EPR study was unable to differentiate which active site of the Q282W variant gains activity. Although the C-terminal metal binding site might be activated by the newly-introduced tryptophan. The absence of a functional loop segment in the C-terminal site precludes the possible catalysis in the C-terminal site. It is possible that the presence of Glu333 may act as an acid/base to facilitate proton-coupled electron transfer in the C-terminal metal binding site. Since the C-terminal site is less solvent accessible and the cavity of the C-terminal metal binding site is too small to bind with oxalate (based on the crystal structure of WT OxDC) [44], mutation in the C-terminal site likely increases activity in the N-terminal site, perhaps, by long-distance electron transfer. This is consistent with a hypothesis that was proposed based on HFEPR studies. [49]

5.4 Experimental Section

5.4.1 Protein Expression and Purification

C-terminal His$_6$-tagged *Bs*OxDC W132F in the pET32a vector was transformed into *E. Coli* BL21(DE3). The cells were grown at 37 °C until the OD$_{600}$ had reached 0.5. Heat-hock with continuous shaking was performed at 42 °C for 15 min, following by addition of 0.8 mM IPTG and 4 mM MnCl$_2$. Supernatant of the protein lysate was loaded on Nickel-NTA affinity column and eluted by 250 mM imidazole in 50 mM phosphate buffer, pH 8.5. The fractions containing 44 kDa protein were pooled and dialyzed against 500 mM NaCl, 50 mM Tris-HCl, pH 8.5 to remove imidazole.

The protein solution was treated with 5% (w/v) Chelex 100-X resin for 2 hr at 4 °C and concentrated by Amicon Ultra centrigutation filter device (30K) to desired concentration. Metal content was confirmed by ICP-MS which was performed at the University of Georgia, Chemical Analysis Center.

5.4.2 Steady-state Kinetic Assay

Reactions were initiated (100 mM citrate buffer, pH 4.0, 125 mM NaCl, 300 μM *o*-PDA and 0-200 mM oxalate) by addition of enzyme at 25 °C, and quenched after 1 min by addition of 100 mM NaOH. The amount of formate produced was determined by coupled assay, which the production of formate was quantified via the conversion of NAD^+ to NADH by formate dehydrogenase in 50 mM phosphate buffer, pH 7.8 with 1.5 mM NAD^+ and 0.5 U FDH. The amount of NADH was measured at 340 nm using UV-Vis spectroscopy after 16 h incubation at 37°C.

5.4.3 EPR Experiments

Samples used for EPR analysis were incubated with Chelex resin for 2hrs on ice to remove free metal ions before being concentrated to approx. 590 mM using an Amicon Ultra-15 Centrifugal Filter Unit (30K) from Millipore (Billerica, MA). Protein concentrations were determined using the Bradford assay (Pierce, Rockford, IL). EPR measurements of the enzyme samples were performed in poly-buffer (100 mM sodium citrate, 50 mM Bis-Tris and 25 mM Tris-HCl, containing 250 mM KCl and 30% glycerol) in samples adjusted to pH 8.5, pH 5.7 and pH 4.2. For oxalate-containing samples, 200 mM potassium oxalate was added at each solution pH, and the resulting solutions mixed in the EPR tube at room temperature to initiate the reaction. After 15 s, each sample was fast-frozen in an acetone/dry ice slush and stored in liq. N2. The final concentration of oxalate in each sample was 100 mM.

Samples for X-band (9.4 GHz) EPR spectroscopy were measured at the CalEPR center at the University of California, Davis. Continuous wave (CW) spectra were collected using a Brker Instruments EleXsys-II E500 CW EPR spectrometer (Brker, Billerica, MA) equipped with an Oxford Instruments ESR900 liquid helium cryostat and Oxford Instruments ITC503 temperature and gas-flow controller. Samples were measured under non-saturating slow-passage conditions using a Super-High Q resonator (ER 4122SHQE) or Dual Mode resonator (ER 4116DM), specific parameters for microwave frequencies, modulation amplitude and temperature are included in figure legends.

5.4.4 KIEs Experiments

The internal competition method was used in measuring the primary ^{13}C and secondary ^{18}O IEs for the enzymatic reaction of W132F OxDC. Natural abundance heavy isotope atom content oxalate was used as substrate. Partial isotope discriminating and total conversion reactions were both performed at pH 4.2 and pH 5.7. Reaction mixtures, which contained either 0.5 mM *o*-phenylenediamine and 100 mM 1.4-bis(2-hydroxyethyl)piperazine, pH 4.2 or piperazine, pH 5.7, were sparged with N2 for 1 hr to remove adventitious CO_2 in solution. 40 mM potassium oxalate, sparged with oxygen for 1 hr, was then added to initiated the reaction. Reactions were quenched by adding 500 mM Tris-HCl pH 7.5 after 37 min - 3 h to obtain different fractionS of reactions for partial reactions. For total conversion reactions, enzyme was incubated with reaction mix at 22 °C for 14 h. CO_2 produced during the reactions were collected and purified through a vacuum line and measured on an isotope ratio mass spectrometer (IRMS). Quenched reactions were filtered with an Amicon filtration device to remove the enzyme. An aliquot was taken for each sample to determine the fraction of reaction, f, using the oxalate detection kit (Trinity) and FDH assay to quantify the residue oxalate and formed formate, respectively. A column with Bio-Rad AG-1 resin was used to separate formate and oxalate in the reaction solution by eluting with by deionized water followed by dilute H_2SO_4, pH 2.7. Fractions that contained oxalate or formate were pooled, HEPES (pH 7.0) was added to formate, and the pH of both solutions was adjusted to neutral using 0.1 N NaOH. Neutralized oxalate and formate solutions were reduced in volume under vacuum and then sparged N_2 for 30 min before completely drying out overnight at 70 °C in a sand bath under high vacuum. I_2 (0.25 - 0.4 g) containing DMSO (2 ml) was injected into dried oxalate or formate samples and reacted for 45 min on the vacuum line with continuous stirring. The ratios of heavier and lighter isotope of C and O in CO_2 produced by oxidized oxalate or formate were measured by IRMS. In order to rule out solvent incorporation during the enzyme reaction, 2% of H^{18}_2O was added as part of the H_2O and the reaction performed using the same procedure as the pH 4.2 partially-run reactions.

6. DESIGN AND CHARACTERIZATION OF THE CLEAVABLE OXDC VARIANT

6.1 Introduction

OxDC is a bicupin metalloprotein, which has two similar manganese binding sites in one monomer. The presence of two metal centers not only complicates the assignment of signals in the EPR spectra, but also increases difficulties in kinetically characterizing the functional role of a residue in one site when less than two Mn(II) ions bind to a monomer; i.e. all metal analysis are actually an average over both sites. Although single-site mutagenesis introduces changes in only one site, such local changes might affect the other metal binding site for structural and electronic reasons. [55] It seems likely that both sites are important, and that they interact with each other. Due to these technical issues, the role of C-terminal metal binding site remains poorly defined. Assuming that both sites are important, but only the N-terminal site is catalytically active, the presence of manganese in the N-terminal site is essential. However, purified OxDC and its site-specific variants are often loaded with less then two manganese ions per monomer, [55] [46] raising questions about metal distribution.

6.1.1 Functional Importance of the C-terminal Domain of OxDC

Substantial evidence suggests that the N-terminal metal binding site is the active site in OxDC, but the possibility that the C-terminal site is also catalytically active cannot be ruled out. Even if the C-terminal domain cannot perform catalysis, if any, have other functional roles. In previous attempts to investigate the functional role of conserved residues in the C-terminal domain, several interesting findings suggested that it played a structural role. [45] For example, mutation of the C-terminal metal binding site in the E333D variant significantly reduced enzymatic activity by affecting metal loading in both binding sites. [45] Conversely, the Q282W variant shows a 40% increase in activity with the introduction of tryptophan residue to mimic the N-terminal metal binding site.

6.1.2 Metal Distribution in OxDC

There are two metal binding sites in each monomer of OxDC, and each site contains one manganese according to the crystal structure. However, the heterologus expression of WT OxDC often leads to a manganese content of about 1.4-1.8 atoms/monomer, indicating that only 70-90% of the metal binding sites are occupied by manganese. Other transition metals, such as Zn, Cu and Fe, can be loaded in the protein, but the content of those metals is very small. The 10-30% of empty metal binding sites raise an interesting question about the metal distribution in OxDC when the manganese content is lower than 2 atoms/monomer. Given that the metal content obtained from the ICP-MS analysis is an average number, different allocations of the 1.4-1.8 atoms of manganese in the two metal binding sites in WT can be proposed. One possibility is with sub-stoichiometric occupation of the second site. Another possibility is that some enzyme molecules are fully loaded with manganese, with the remainder having both metal binding sites empty. Assuming that only the N-terminal site is catalytically active, the extent of metal loading and its distribution between the two sites should have a considerable impact on enzyme activity. The allocation of manganese between the sites in the protein with low metal content is even more important. For the ΔE162 variant, the average metal content is 1.3 Mn/monomer. There is no way to determine whether the N-terminal metal binding sites are fully occupied and 33% of the C-terminal sites are occupied, or the C-terminal metal binding site is fully occupied and partial N-terminal sites are empty, or 65% of enzyme is fully occupied by manganese and the rest is catalytically inactive.

6.1.3 Single Domain OxDC

If the two metal binding domain could be studied separately, the functional role of C-terminal site and the allocation of the manganese might be addressed.

In efforts to obtain single domain mutants of OxDC, genes encoding the N-terminal domain and C-terminal domain of OxDC have been expressed separately in *E. coli* (Moomaw, unpublished data). Although single domain OxDC variants could be overexpressed under the same conditions as the full length enzyme, the expression host was unable to load the correct metal into the protein. Thus, the single domain protein obtained by this method contained zinc. Refolding of the apo enzyme was unsuccessful due to precipitation. A new strategy for obtaining correctly folded, high yield, manganese containing single domain OxDC variant was therefore explored.

This alternative approach to obtain a single domain OxDC variant involved expression of the full length protein with a proteinase recognition site inserted between the N-terminal and C-terminal domains. This full length OxDC variant was expected to fold correctly with Mn(II) in both metal binding sites during expression. This cleavable OxDC could then be treated with the appropriate proteinase, releasing the two separate Mn-containing domains. This method would not only provide a new opportunity to study the protein domains individually, but also create a new platform for the examination of the role of the conserved residues in OxDC with or without the presence of the other domain.

This chapter outlines the method of construction, expression and purification of a cleavable OxDC variant, and optimal condition for the cleavage reaction.

6.2 Results and Discussion

Enterokinase, thrombin and Tobacco Etch Virus endopeptidase (TEV) are three common proteinases that can specifically cleave sequences in target protein. The optimal pH values for cleavage by commercially available enterokinase (Novagen), thrombin (Novagen) and TEV (Promega) are pH 7.4, pH 8.4, and pH 7, respectively. Since the calculated pI for OxDC is 6.1, the pH for optimal cleavage conditions should be higher than pH 6.1. Given that OxDC is stable when stored in pH 8.5, proteinase with a pH optimum close to this value would be most suitable.

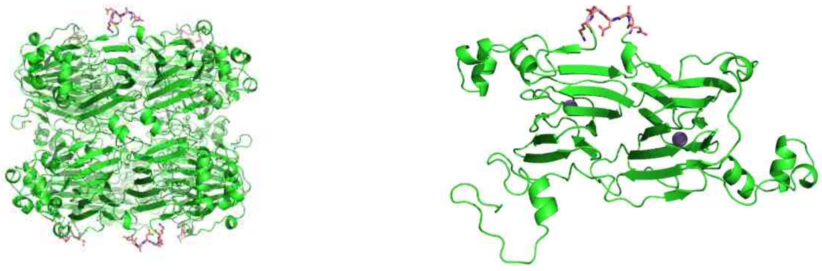

(a) Model of hexamer (b) Model of monomer

Figure 6.1. Homology model for the enterokinase cleavable OxDC. Enterokinase recognition site DDDDK was inserted between of Gln233 and Glu234.

N-terminal and the C-terminal cupin domains are connected by a flexible loop. The proteinase cleavage site was therefore inserted into this loop region. To minimize disruption of the structure of the WT OxDC, two locations were chosen for the insertion. In the first construct, the cleavage site was between Gln233 and Glu234 (Fig. 6.1), which lies in the middle of the two domains. Direct insertion of the recognition site peptide sequence made the recognition site more accessible to the proteinase, and this region already contained several glutamate residues, which are similar to aspartate in the enterokinase recognition sequence (DDDDK). The DDDDK segment was therefore introduced between Gln233 nd Glu234. A second location was chosen at one end of the region connecting the N-terminal and C-terminal domains (Fig. 6.2). Since this site is at the corner of the N-terminal cupin, replacement of the original residues in the WT OxDC by the new proteinase recognition sequence was expected to have less effect on the hexameric structure of the protein. In fact, the proline and glycine in the native peptide sequence are also present in the specific recognition sequence of thrombin. The peptide segment LVPRGS was therefore designed to replace residues 216-221 (EGPNGE).

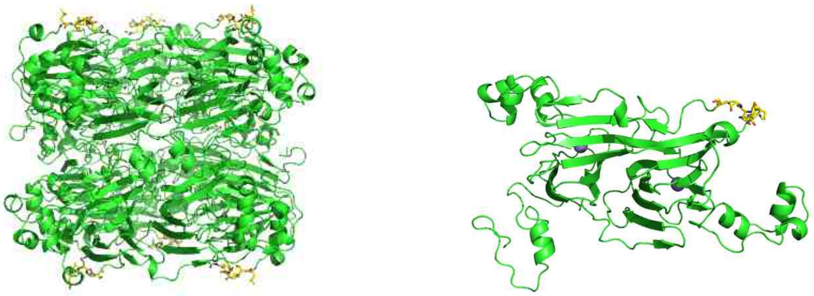

(a) Model of hexamer

(b) Model of monomer.

Figure 6.2. Homologus model for the thrombin cleavable OxDC. The residue 216-221 were replaced by the thrombin recognize site LVPRGS.

6.2.1 Enterokinase Cleavable OxDC

OxDC containing an enterokinase recognition site was overexpressed in BL21(DE3), and the manganese content of the protein was 0.8 Mn/monomer. After treatment with enterokinase, multiple bands were observed on the SDS-PAGE (Fig. 6.3), which indicated that the digestion by enterokinase was not specific for the inserted DDDDK segment despite the absence of any similar sequence in WT OxDC.

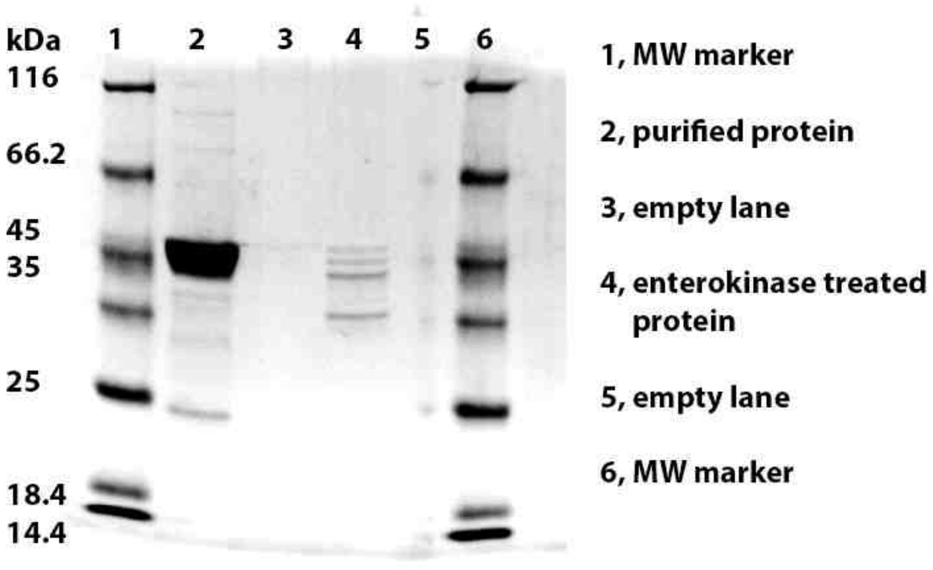

Figure 6.3. SDS-PAGE shows the non-specific cleavage by enterokinase.

6.2.2 Thrombin Cleavable OxDC

Protein Expression and Steady-state Kinetic Parameters

Thrombin, which is a 33.5 kDa serine proteinase, specifically recognizes the peptide sequence LVPRGS and cleaves the peptide bond between Arg and Gly. A thrombin cleavable OxDC was expressed in BL21(DE3), and the metal incorporation of the purified, recombinant protein was 1.2 Mn/monomer and 0.2 Zn/monomer. Steady-state kinetic parameters were determined using the standard FDH assay (Fig. 6.4) and showed a 2.4-fold increase in K_M and a similar k_{cat} value compared to that of unmodified WT OxDC (Table 6.1).

Cleavage Reaction

The thrombin cleavage reaction was performed at pH 8.4, which is the optimal pH for digestion, and SDS-PAGE was used to analyze the fragments arising from the

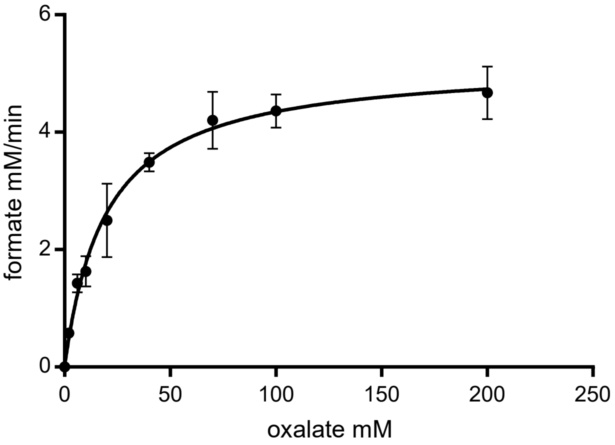

Figure 6.4. Michaelis-Menten curve of the thrombin site inserted clevable OxDC

Table 6.1.
Kinetic parameters of thrombin cleavable OxDC measured by FDH assay.

	K_M	k_{cat}	k_{cat}/K_M/Mn	Mn content
	(mM)	(s^{-1})	($M^{-1}s^{-1}$)	(Mn/monomer)
WT	8 ± 1	60 ± 2	5670 ± 840	1.4
Cleavable OxDC	19 ± 2	52 ± 4	2300 ± 360	1.2

cleavage. The molecular weight of the thrombin cleavable OxDC is 44.4 kDa, and the two truncated fragments are 24.8 kDa and 19.7 kDa for the N-terminal and C-terminal domains, respectively. Incubation of the cleavable OxDC with the thrombin resulted in the appearance of two new bands on the gel of approximately 26 kDa and 20 kDa in size. The molecular weight of these bands were 24.8 kDa and 19.7 kDa, respectively, was confirmed by LC-MS. Incubation of the cleavable OxDC with thrombin at different ratios and temperatures (16 °C, 22 °C and 37 °C) for 5 h 18 h 24 h and 30 h, confirmed the cleavage to be thrombin dependent with an optimal reaction temperature of 37 °C (Fig. 6.5).

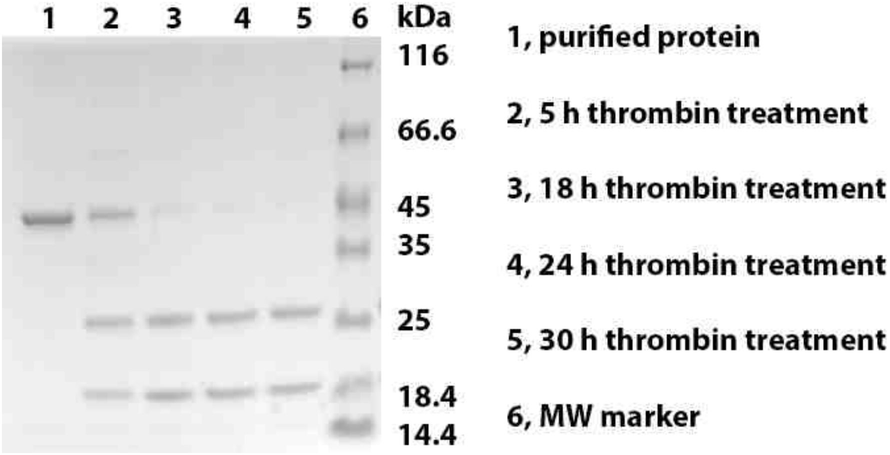

Figure 6.5. SDS-PAGE shows the specific cleavage by thrombin over different time points.

Table 6.2.
Kinetic parameters of thrombin cleavable OxDC before and after cleavage reaction measured by FDH assay.

	K_M	k_{cat}	$k_{cat}/K_M/\mathrm{Mn}$
	(mM)	(s^{-1})	($\mathrm{M}^{-1}\mathrm{s}^{-1}$)
Cleavable OxDC	19 ± 2	52 ± 4	2300 ± 360
Cleavable OxDC after incubation at 37 °C	23 ± 2	58 ± 3	2050 ± 240
Cleavable OxDC after cleavage reaction	30 ± 3	8 ± 2	220 ± 60

After treatment with thrombin, the cleavable OxDC retained only 10% of the $k_{cat}/K_M/\mathrm{Mn}$ compared to the untreated sample. This drop in activity has not due to incubation of the protein at 37 °C for 30 h in control experiments. (Table 6.2.)

Separation of Two Domains in the Cleavable OxDC

Separation of the two domains in thrombin cleavable OxDC, however, proved to be difficult. The thrombin cleavable OxDC is a C-terminal His_{x6}-tagged protein. After digestion with thrombin, efforts to separate the His-tagged C-terminal domain and the N-terminal domain using Ni-NTA affinity chromatography were undertaken. Thrombin was removed using a benzamidine sepharose column, which specifically recognizes and binds serine proteinases such as thrombin. However, interactions between the N-terminal and C-terminal domains lead to formation of aggregates, which retained a strong affinity for the Ni-NTA affinity column due to the His-tag at the C-terminal domain. Therefore, Ni affinity chromatography was not successful in separating two domains of the thrombin cleaved OxDC. Size exclusion chromatography confirmed the existence of the aggregates. The addition of 8 M urea to the Ni-NTA column to denature the protein enabled separation of the N-terminal and C-terminal domains by elution with different concentrations of imidazole.

The crystal structure of WT OxDC shows that the interaction between the N-terminal and C-terminal domains might be attributed to two possible sources: (i) the hydrophobic interaction between the β-sheets in the two cupin domains and (ii) hydrogen bonding between loop regions of adjacent cupins. It was not possible, however, to disrupt the interaction by the addition of detergent, such as 0.2% of Triton-X 100, or a high concentration of salt, such as 1M NaCl. This observation is intriguing and indicative of the complexity of the interactions between the domains of OxDC. It is interesting that native OxOx forms a homohexamer in the crystal structure [44] even though individual OxDC domains form a tightly-bound hetero-oligomeric structure in solution. Comparing residues at the interface of the two cupin domains in *Bs*OxDC with residues in the cupin domain of barley OxOx, more hydrophobic residues are present on the surface of the β-sheets in the two cupins of OxDC. OxOx has mostly hydrophilic residues located between the interfaces of the adjacent monomers.

According to SDS-PAGE analysis of the digested thrombin-cleavable OxDC, no band for the full-length protein was detected. This suggests that the enzyme activity of the hetero-oligomeric OxDC domains does not come from residual undigested full-length protein. If the active sites of OxDC can function independently , it would be expected there would be no effect from cleaving the enzyme with thrombin. However, the 10-fold decrease in activity supports the idea that an interaction between the two OxDC domains is important for maintaining enzymatic activity. The observed activity likely arises from domains positioned in the same orientation in the cleaved variant as native OxDC.

6.3 Conclusion

Successful expression of a thrombin cleavable OxDC variant was achieved by reengineering OxDC to include a proteinase recognition site between the N-terminal and C-terminal domains. This permitted expression of Mn-containing single domains without refolding. The reduced enzymatic activity observed after cleavage suggests that an interaction between the N-terminal and C-terminal domains is important for maintaining activity. Although the two domains were not successfully separated, thrombin cleavable OxDC still could be used as a platform for studying the interaction between the N-terminal and C-terminal domaind of OxDC.

6.4 Experimental Section

6.4.1 Cleavage Site Insertion

The primers that were used to construct the enterokinase cleavable OxDC (EC) and thrombin cleavable OxDC (TC) are listed in Table 6.3:

PCR conditions were similar to those described in Chapter 4, except with 10 additional reaction cycles. The PCR products were digested by *Dpn*I to remove template plasmid and were transformed into *E. coli* Nova Blue competent cells for

Table 6.3.

Primers for construct cleavable OxDC

Primer	Sequence
EC Fwd	5’-/5phos/CGACAAGGAGCCGATCGAATCTGAGGG -3’
EC Rev	5’-/5phos/TCGTCGTCTTGTTCAAGAAGGCGGTAA G - 3’
TC Fwd	5’-/5phos/GATGATATTGTGCTGGTGCCGCGTGGTTCTGTGCCTTATCCATTTACTTA -3’
TC Rev	5’-/5phos/TAAGTAAATGGATAAGGCACAGAACCACGCGGCACCAGCACAATATCATC -3’

amplification. The sequence of the DNA was confirmed at the DNA Sequencing Core facility at the University of Michigan.

6.4.2 Protein Expression and Purification

The sequenced genes were transformed into *E. coli.* BL21(DE3) for overexpression using previously established methods. [46] Briefly, the cell culture was heat-shocked at 42 °C for 15 min once OD_{600} had reached 0.4, followed by addition of 5 mM $MnCl_2$ and 0.8 mM IPTG to induce the overexpression of protein. Cells were harvested by centrifugation and lysed by sonication. The debris was removed by centrifugation and the soluble protein in supernatant was purified using Ni-NTA affinity chromatography. The elution fractions were pooled and dialyzed against storage buffer (50 mM Tris-HCl, pH 8.5, 500 mM NaCl) to remove imidazole. Proteins were concentrated to desired concentration using Amicon Ultra 30K centrifuge device (Millipore) and treated with Chelex-100 resin (Bio-Rad) to remove the free metal in the solution. Protein purity was estimated from the protein band on SDS-PAGE. Protein concentrations were determined using the Bradford assay, in which bovine serum albumin was used as the standard. The metal contents of the enzymes were determined using ICP-MS.

6.4.3 FDH Assay

Reactions were initiated (100 mM citrate buffer, pH 4.0, 125 mM NaCl, 300 μM *o*-PDA and 0-80 mM oxalate) by addition of enzyme at 25 °C, and quenched after 1 min by addition of 100 mM NaOH. The amount of formate produced was determined by coupled assay, which the production of formate was quantified via the conversion of NAD^+ to NADH by formate dehydrogenase in 50 mM phosphate buffer, pH 7.8 with 1.5 mM NAD^+ and 0.5 U FDH. The amount of NADH was measured at 340 nm using UV-Vis spectroscopy after 16 h incubation at 37°C.

6.4.4 Cleavage Experiments

Thrombin stock solution was prepared by dissolving 1 mg bovine thrombin (MP Biomedicals Biovine Thrombin High purity grade, Cat. 154163) in 2402 μL dilution buffer (50 mM sodium citrate, pH 6.5, 200 mM sodium chloride, 0.1% polyethylene glycol 8000 and 50% glycerol) and stored at -80 °C. The cleavage reaction was performed in a solution containing following components: 300 μL thrombin cleavable OxDC (9 mg/ml, in 50 mM Tris-HCl, pH 8.5, 500 mM NaCl), 1200 μL thrombin stock solution, 1500 μL cleavage buffer (200 mM Tris-Cl, pH 8.5, 1.5 M NaCl and 25 mM $CaCl_2$) and 12 mL deionized water. The reaction mixture was incubated at 37 °C for 24 h. The attempts to separate the two domains were designed as shown in Fig. 6.6 and Fig. 6.7. The buffers used in the separation experiments are listed in Table 6.3. In separation 1 (Fig. 6.6), the cleavage reaction mixture was loaded on to the Benzamidine Sepharose column. The flow-through from this column was loaded onto the Ni-NTA column that had been equilibrated with the wash buffer. The flow-through of the Ni-NTA column was collected and the protein that remained bound to the column was eluted with the elution buffer. Finally, the components in each step were analyzed by SDS-PAGE. In separation 2 (Fig. 6.7), after the cleavage reaction mixture was loaded onto the Ni-NTA column, the column was washed by 8 M urea and the flow-through was collected. Next the column was washed with the 3 volumes of washing buffer, followed by elution buffer to elute the protein remaining on the column after the urea urea. The eluted protein was analyzed by SDS-PAGE.

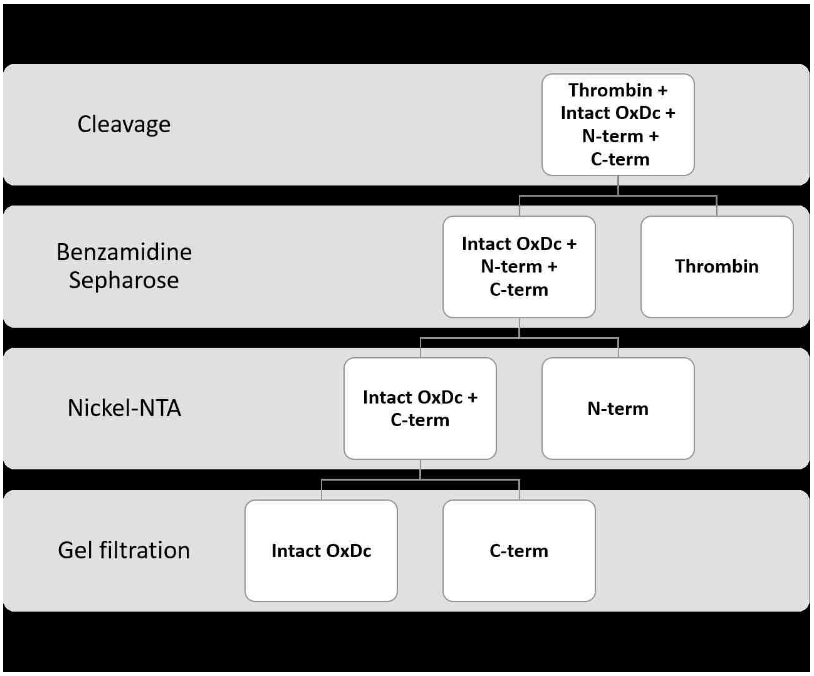

Figure 6.6. Separation strategy 1.

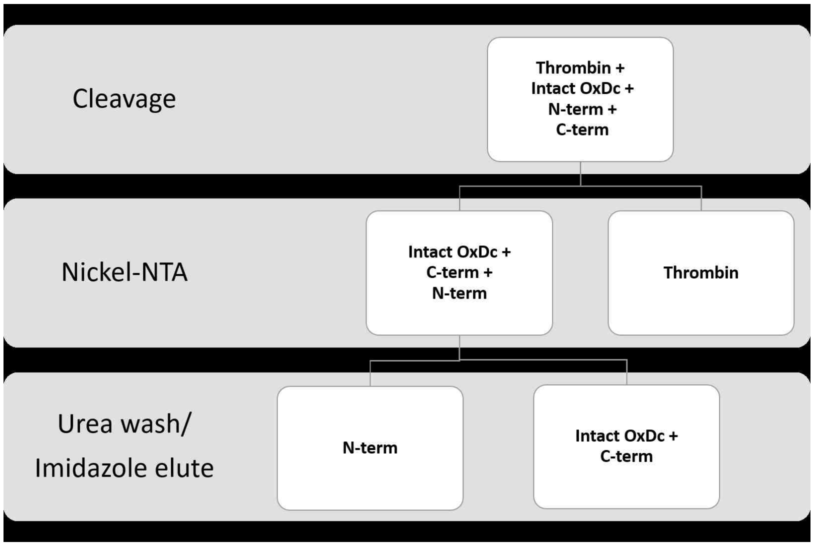

Figure 6.7. Separation strategy 2.

Table 6.4.
Buffers used in the separation experiments

Buffer	Component
Washing buffer	50 mM KPi, pH 8.5, 500 mM NaCl, 20 mM Imidazole
Urea washing buffer	8 M urea, 50 mM KPi, pH 8.5, 500 mM NaCl, 20 mM Imidazole
Elution buffer	50 mM KPi, pH 8.5, 500 mM NaCl, 250 mM Imidazole

7. FUTURE DIRECTIONS

My findings have demonstrated the production of Mn(III) during the enzymatic catalytic cycle, which lays the ground work for further characterization of the redox change between Mn(II) and Mn(III). The formation of Mn(III) in the presence of oxalate also raises questions about the species responsible for oxidation of the Mn(II) in the active site of the enzyme, which may be mediated by O_2. In order to understand the role of the C-terminal of OxDC better, it will be necessary to determine which of the manganese ions (or both) in the two metal binding sites is oxidized during turnover.

7.1 Further Investigation on the Mn(III) Center Using High-field EPR (HFEPR) and Magnetic Circular Dichroism (MCD)

EPR experiments have provided clear evidence for the production of Mn(III) in the enzyme when oxalate is present under acidic conditions. However, X-band EPR is limited in providing detailed information about the electronic environment of the metal center and Mn/ligands interactions. High-field EPR would be ideal for uncovering more information about the metal center while the Mn(III) is being produced, because it is possible to differentiate between the two metal centers by determining the hyperfine coupling parameters of the metal at each site. HFEPR has been successfully applied to WT OxDC and the information obtained experimentally is consistent with that obtained by calculations. [99] However, controlling the reaction duration in the sample preparation would be difficult for this set of experiments. The time between the addition of oxalate and the freeze-quench must be less than 1 ms. If the reaction time is too short, insufficient Mn(III) will be formed and so the Mn(III) concentration will be too low to obtain good spectral data. If the reaction time is >1 ms, the reaction mixture will contmaking any interpretation more difficult.

Instead of HFEPR, magnetic circular dichroism (MCD) along with the density-function theory (DFT) calculations is an alternative way to characterize the metal centers in OxDC. MCD is a powerful method for investigating the excited and ground states of paramagnetic systems, [103] and has not yet been applied to studies of OxDC. MCD utilizes an external magnetic field to induce optical activity, permitting the observation of Zeeman splitting of the sample in the ground and excited states as well as field-induced transitions between states defined by the ligand environment. [103] More specifically, for the OxDC system, it is likely that the signal for octahedral Mn(III) obtained from the d-d transition and the signal for charge transfer between ligand and Mn(II) will be present. The spectrum of the protein is expected to be different when the protein is in the resting and catalytically active states. The technical issues for using MCD are similar to those in HFEPR, although, sample preparation for MCD is more complicated than for EPR due to the higher glycerol content required for the measurement. This not only extends the dead time for sample mixing after oxalate addition, but also slows down the release of the CO_2.

7.2 Anaerobic Experiments

The existence of Mn(III) in purified W132F variant in the resting state has been confirmed by parallel mode X-band EPR spectroscopy, even though Mn(III) is present in the WT enzyme only during catalytic turnover. The mechanism of Mn(III) formation is unclear, yet the evidence suggests that participation of O_2 in catalysis is important Some anaerobic experiments have been carried out on OxDC, but these are insufficient to explain the role of O_2 in catalysis. In the earlier work, dithionite and glucose oxidase were used to remove dissolved O_2 from solution, but failed to remove tightly bound O_2 from the enzyme. [43] However, it might be argued that the 1%

OxOx activity in OxDC could potentially use up all of the O_2 that is tightly bound in the enzyme (presumably on the metal) in the presence of oxalate. Therefore, for anaerobic sample preparations, a certain amount of oxalate can be added to the solution, together with excess glucose oxidase and catalase to facilitate the consumption of the trace amount of tightly bound oxygen in the enzyme. Using this method of preparing anaerobic samples, the EPR and MCD spectra may reveal the role of O_2 and the mechanism of Mn(III) formation during catalysis.

7.3 Redox Titration to Manipulate the Oxidation State of Manganese

The observation of Mn(III) also raises the question of the oxidation state of the metal in initial steps of the reaction. Titration of sodium periodate with purified Mn(II)-containing OxDC should allow variants containing Mn(III) and Mn(IV) to be obtained. Similar redox titration experiments have been performed for barley OxOx revealing the importance of higher oxidation states of manganese, such as Mn(III), for catalysis. Moreover, addition of ascorbate or NH_2OH will reduce manganese ions in the enzyme to the Mn(II) oxidation state. [71] Kinetic parameters for redox-titration treated OxDC and its variants could be obtained using MIMS, and EPR measurements also can be made. If the resulting solution contains a mixture of redox species, the EPR spectra could potentially be complicated, but the change in the signal when the enzyme is incubated under different conditions should provide information about the oxidation state of the manganese prior to catalysis. The redox potential should also be measured for these samples.

7.4 Separate Two Domains in Cleavable OxDC

The inability to separate the domains in the cleavable OxDC indicates that the interaction between the two domains of OxDC is very tight and functionally important. Separation of the two domains is still an interesting direction for further studies. The approach used in the experiments described was to insert the proteinase recognition site in between the two domains and cleave after purification. Although the X-ray crystal structure of OxDC shows a hexameric oligomer, size exclusion chromatograph confirmed that aggregates of WT OxDC oligomers readily formed after purification. Disruption of the protein-protein interaction will require a systematic screening of different conditions. Additives, such as proline and arginine, can be added into solution to reduce the interaction between two domains. [104] Various concentrations of urea should also be screened for their effect in disentangling the loop regions behavior manner to release the single domains from the aggregates. These additives might be added during purification to maximally reduce the aggregation. Another direction will be to mutate surface residues so as to disrupt interaction between the two domains. This will involve the identification of conserved inter-domain residues as candidates for mutation. The interface residues that break salt bridge and hydrophobic interactions should be ideal targets for mutagenesis. Deletion of the first 44 amino acids in the protein may also reduce the interaction between the two domains, but the influence of this deletion to the enzyme activity should to be verified.

REFERENCES

REFERENCES

[1] A. Hodgkinson and P. Zarembski, "Oxalic acid metabolism in man: A review," *Calcified Tissue Research*, vol. 2, no. 1, pp. 115–132, 1968.

[2] E. Kohman, "Oxalic acid in foods and its behavior and fate in the diet three figures," *The Journal of Nutrition*, vol. 18, no. 3, pp. 233–246, 1939.

[3] W. Chai, M. Liebman, S. Kynast-Gales, and L. Massey, "Oxalate absorption and endogenous oxalate synthesis from ascorbate in calcium oxalate stone formers and non-stone formers," *American journal of kidney diseases*, vol. 44, no. 6, pp. 1060–1069, 2004.

[4] L. K. Massey, M. Liebman, and S. A. Kynast-Gales, "Ascorbate increases human oxaluria and kidney stone risk," *The Journal of nutrition*, vol. 135, no. 7, pp. 1673–1677, 2005.

[5] Y. Ogawa, T. Miyazato, and T. Hatano, "Oxalate and urinary stones," *World journal of surgery*, vol. 24, no. 10, pp. 1154–1159, 2000.

[6] L. F. James, "Oxalate toxicosis," *Clinical Toxicology*, vol. 5, no. 2, pp. 231–243, 1972.

[7] P. Zarembski and A. Hodgkinson, "Plasma oxalic acid and calcium levels in oxalate poisoning," *Journal of clinical pathology*, vol. 20, no. 3, pp. 283–285, 1967.

[8] R. Siener, D. Ebert, C. Nicolay, and A. Hesse, "Dietary risk factors for hyperoxaluria in calcium oxalate stone formers," *Kidney international*, vol. 63, no. 3, pp. 1037–1043, 2003.

[9] M. Hatch, R. W. Freel, and N. Vaziri, "Intestinal excretion of oxalate in chronic renal failure." *Journal of the American Society of Nephrology*, vol. 5, no. 6, pp. 1339–1343, 1994.

[10] R. P. Holmes and D. G. Assimos, "The impact of dietary oxalate on kidney stone formation," *Urological research*, vol. 32, no. 5, pp. 311–316, 2004.

[11] C. D. Scales, A. C. Smith, J. M. Hanley, C. S. Saigal, U. D. in America Project *et al.*, "Prevalence of kidney stones in the united states," *European urology*, vol. 62, no. 1, pp. 160–165, 2012.

[12] O. Ivanovski and T. B. Drüeke, "A new era in the treatment of calcium oxalate stones&quest," *Kidney international*, vol. 83, no. 6, pp. 998–1000, 2013.

[13] P. A. Donaldson, T. Anderson, B. G. Lane, A. L. Davidson, and D. H. Simmonds, “Soybean plants expressing an active oligomeric oxalate oxidase from the wheat gf-2.8 (germin) gene are resistant to the oxalate-secreting pathogen sclerotina sclerotiorum,” *Physiological and Molecular Plant Pathology*, vol. 59, no. 6, pp. 297–307, 2001.

[14] M. Mäkelä, S. Galkin, A. Hatakka, and T. Lundell, “Production of organic acids and oxalate decarboxylase in lignin-degrading white rot fungi,” *Enzyme and Microbial Technology*, vol. 30, no. 4, pp. 542–549, 2002.

[15] E. Emiliani and P. Bekes, “Enzymatic oxalate decarboxylation in aspergillus niger,” *Archives of Biochemistry and Biophysics*, vol. 105, no. 3, pp. 488–493, 1964.

[16] A. L. Baetz and M. J. Allison, “Purification and characterization of oxalyl-coenzyme a decarboxylase from oxalobacter formigenes.” *Journal of bacteriology*, vol. 171, no. 5, pp. 2605–2608, 1989.

[17] D. Svedružić, S. Jónsson, C. G. Toyota, L. A. Reinhardt, S. Ricagno, Y. Lindqvist, and N. G. Richards, “The enzymes of oxalate metabolism: unexpected structures and mechanisms,” *Archives of biochemistry and biophysics*, vol. 433, no. 1, pp. 176–192, 2005.

[18] P. Cassland, A. Sjöde, S. Winestrand, L. J. Jönsson, and N.-O. Nilvebrant, “Evaluation of oxalate decarboxylase and oxalate oxidase for industrial applications,” *Applied biochemistry and biotechnology*, vol. 161, no. 1-8, pp. 255–263, 2010.

[19] C. Campieri, M. Campieri, V. Bertuzzi, E. Swennen, D. Matteuzzi, S. Stefoni, F. Pirovano, C. Centi, S. Ulisse, G. Famularo *et al.*, “Reduction of oxaluria after an oral course of lactic acid bacteria at high concentration,” *Kidney international*, vol. 60, no. 3, pp. 1097–1105, 2001.

[20] A. Sjöde, S. Winestrand, N.-O. Nilvebrant, and L. J. Jönsson, “Enzyme-based control of oxalic acid in the pulp and paper industry,” *Enzyme and microbial technology*, vol. 43, no. 2, pp. 78–83, 2008.

[21] N.-O. Nilvebrant, A. Reimann, F. De Sousa, P. Cassland, S. Larsson, F. Hong, and L. J. Jönsson, “Enzymatic degradation of oxalic acid for prevention of scaling,” *Progress in Biotechnology*, vol. 21, pp. 231–238, 2002.

[22] B. Dumas, G. Freyssinet, and K. E. Pallett, “Tissue-specific expression of germin-like oxalate oxidase during development and fungal infection of barley seedlings,” *Plant Physiology*, vol. 107, no. 4, pp. 1091–1096, 1995.

[23] M. Kesarwani, M. Azam, K. Natarajan, A. Mehta, and A. Datta, “Oxalate decarboxylase from collybia velutipes molecular cloning and its overexpression to confer resistance to fungal infection in transgenic tobacco and tomato,” *Journal of Biological Chemistry*, vol. 275, no. 10, pp. 7230–7238, 2000.

[24] R. Wolfenden, C. A. Lewis Jr, and Y. Yuan, “Kinetic challenges facing oxalate, malonate, acetoacetate, and oxaloacetate decarboxylases,” *Journal of the American Chemical Society*, vol. 133, no. 15, pp. 5683–5685, 2011.

[25] R. W. Molt Jr, A. M. Lecher, T. Clark, R. J. Bartlett, and N. G. Richards, "Facile csp2–csp2 bond cleavage in oxalic acid-derived radicals," *Journal of the American Chemical Society*, vol. 137, no. 9, pp. 3248–3252, 2015.

[26] J. A. Micales, "Localization and induction of oxalate decarboxylase in the brown-rot wood decay fungus postia placenta," *International biodeterioration & biodegradation*, vol. 39, no. 2, pp. 125–132, 1997.

[27] M. R. Mäkelä, K. Hildén, A. Hatakka, and T. K. Lundell, "Oxalate decarboxylase of the white-rot fungus dichomitus squalens demonstrates a novel enzyme primary structure and non-induced expression on wood and in liquid cultures," *Microbiology*, vol. 155, no. 8, pp. 2726–2738, 2009.

[28] Z.-X. Jin, C. Wang, W. Chen, X. Chen, and X. Li, "Induction of oxalate decarboxylase by oxalate in a newly isolated pandoraea sp. oxj-11 and its ability to protect against sclerotinia sclerotiorum infection," *Canadian journal of microbiology*, vol. 53, no. 12, pp. 1316–1322, 2007.

[29] C. X. Zhu and F. Hong, "Induction of an oxalate decarboxylase in the filamentous fungus trametes versicolor by addition of inorganic acids," *Applied biochemistry and biotechnology*, vol. 160, no. 2, pp. 655–664, 2010.

[30] A. Tanner and S. Bornemann, "Bacillus subtilis yvrk is an acid-induced oxalate decarboxylase," *Journal of bacteriology*, vol. 182, no. 18, pp. 5271–5273, 2000.

[31] S. R. MacLellan, J. D. Helmann, and H. Antelmann, "The yvri alternative σ factor is essential for acid stress induction of oxalate decarboxylase in bacillus subtilis," *Journal of bacteriology*, vol. 191, no. 3, pp. 931–939, 2009.

[32] S. R. MacLellan, T. Wecke, and J. D. Helmann, "A previously unidentified σ factor and two accessory proteins regulate oxalate decarboxylase expression in bacillus subtilis," *Molecular microbiology*, vol. 69, no. 4, pp. 954–967, 2008.

[33] R. Uberto and E. W. Moomaw, "Protein similarity networks reveal relationships among sequence, structure, and function within the cupin superfamily," *PloS one*, vol. 8, no. 9, 2013.

[34] M. M. Whittaker and J. W. Whittaker, "Characterization of recombinant barley oxalate oxidase expressed by pichia pastoris," *JBIC Journal of Biological Inorganic Chemistry*, vol. 7, no. 1-2, pp. 136–145, 2002.

[35] C. Aguilar, U. Urzúa, C. Koenig, and R. Vicuña, "Oxalate oxidase from ceriporiopsis subvermispora: biochemical and cytochemical studies," *Archives of biochemistry and biophysics*, vol. 366, no. 2, pp. 275–282, 1999.

[36] Z. Zhang, D. B. Collinge, and H. Thordal-Christensen, "Germin-like oxalate oxidase, a h2o2-producing enzyme, accumulates in barley attacked by the powdery mildew fungus," *The Plant Journal*, vol. 8, no. 1, pp. 139–145, 1995.

[37] C. Davoine, E. Le Deunff, N. Ledger, J.-C. Avice, J.-P. Billard, B. Dumas, and C. Huault, "Specific and constitutive expression of oxalate oxidase during the ageing of leaf sheaths of ryegrass stubble," *Plant, Cell & Environment*, vol. 24, no. 10, pp. 1033–1043, 2001.

[38] B. Dumas, A. Sailland, J. Cheviet, G. Freyssinet, and K. Pallett, “Identification of barley oxalate oxidase as a germin-like protein.” *Comptes rendus de l’Académie des sciences. Série III, Sciences de la vie*, vol. 316, no. 8, pp. 793–798, 1993.

[39] G. Delisle, M. Champoux, and M. Houde, “Characterization of oxalate oxidase and cell death in al-sensitive and tolerant wheat roots,” *Plant and Cell Physiology*, vol. 42, no. 3, pp. 324–333, 2001.

[40] M. Vuletić and V. H.-T. Šukalović, “Characterization of cell wall oxalate oxidase from maize roots,” *Plant Science*, vol. 157, no. 2, pp. 257–263, 2000.

[41] H. Liang, C. A. Maynard, R. D. Allen, and W. A. Powell, “Increased septoria musiva resistance in transgenic hybrid poplar leaves expressing a wheat oxalate oxidase gene,” *Plant molecular biology*, vol. 45, no. 6, pp. 619–629, 2001.

[42] F. Zhou, Z. Zhang, P. L. Gregersen, J. D. Mikkelsen, E. de Neergaard, D. B. Collinge, and H. Thordal-Christensen, “Molecular characterization of the oxalate oxidase involved in the response of barley to the powdery mildew fungus,” *Plant Physiology*, vol. 117, no. 1, pp. 33–41, 1998.

[43] A. Tanner, L. Bowater, S. A. Fairhurst, and S. Bornemann, “Oxalate decarboxylase requires manganese and dioxygen for activity overexpression and characterization of bacillus subtilis yvrk and yoan,” *Journal of Biological Chemistry*, vol. 276, no. 47, pp. 43 627–43 634, 2001.

[44] R. Anand, P. C. Dorrestein, C. Kinsland, T. P. Begley, and S. E. Ealick, “Structure of oxalate decarboxylase from bacillus subtilis at 1.75 å resolution,” *Biochemistry*, vol. 41, no. 24, pp. 7659–7669, 2002.

[45] V. J. Just, C. E. Stevenson, L. Bowater, A. Tanner, D. M. Lawson, and S. Bornemann, “A closed conformation of bacillus subtilis oxalate decarboxylase oxdc provides evidence for the true identity of the active site,” *Journal of Biological Chemistry*, vol. 279, no. 19, pp. 19 867–19 874, 2004.

[46] V. Just, M. Burrell, L. Bowater, I. McRobbie, C. Stevenson, D. Lawson, and S. Bornemann, “The identity of the active site of oxalate decarboxylase and the importance of the stability of active-site lid conformations1,” *Biochem. J*, vol. 407, pp. 397–406, 2007.

[47] T. Karmakar, G. Periyasamy, and S. Balasubramanian, “Co2 migration pathways in oxalate decarboxylase and clues about its active site,” *The Journal of Physical Chemistry B*, vol. 117, no. 41, pp. 12 451–12 460, 2013.

[48] D. Svedružić, Y. Liu, L. A. Reinhardt, E. Wroclawska, W. W. Cleland, and N. G. Richards, “Investigating the roles of putative active site residues in the oxalate decarboxylase from bacillus subtilis,” *Archives of biochemistry and biophysics*, vol. 464, no. 1, pp. 36–47, 2007.

[49] L. C. Tabares, J. Gatjens, C. Hureau, M. R. Burrell, L. Bowater, V. L. Pecoraro, S. Bornemann, and S. Un, “ph-dependent structures of the manganese binding sites in oxalate decarboxylase as revealed by high-field electron paramagnetic resonance,” *The Journal of Physical Chemistry B*, vol. 113, no. 26, pp. 9016–9025, 2009.

[50] E. Emiliani and B. Riera, “Enzymatic oxalate decarboxylation in aspergillus niger: Ii. hydrogen peroxide formation and other characteristics of the oxalate decarboxylase,” *Biochimica et Biophysica Acta (BBA)-Enzymology*, vol. 167, no. 2, pp. 414–421, 1968.

[51] B. T. Saylor, L. A. Reinhardt, Z. Lu, M. S. Shukla, L. Nguyen, W. W. Cleland, A. Angerhofer, K. N. Allen, and N. G. Richards, “A structural element that facilitates proton-coupled electron transfer in oxalate decarboxylase,” *Biochemistry*, vol. 51, no. 13, pp. 2911–2920, 2012.

[52] A.-F. Miller, “Redox tuning over almost 1 v in a structurally conserved active site: lessons from fe-containing superoxide dismutase,” *Accounts of chemical research*, vol. 41, no. 4, pp. 501–510, 2008.

[53] M. K. Coggins, X. Sun, Y. Kwak, E. I. Solomon, E. Rybak-Akimova, and J. A. Kovacs, “Characterization of metastable intermediates formed in the reaction between a mn (ii) complex and dioxygen, including a crystallographic structure of a binuclear mn (iii)–peroxo species,” *Journal of the American Chemical Society*, vol. 135, no. 15, pp. 5631–5640, 2013.

[54] E. Mario, G. Nigel *et al.*, “Nitric oxide reversibly inhibits bacillus subtilis oxalate decarboxylase,” *Chemical Communications*, vol. 47, no. 11, pp. 3111–3113, 2011.

[55] E. W. Moomaw, A. Angerhofer, P. Moussatche, A. Ozarowski, I. García-Rubio, and N. G. Richards, “Metal dependence of oxalate decarboxylase activity,” *Biochemistry*, vol. 48, no. 26, pp. 6116–6125, 2009.

[56] M. R. Burrell, V. J. Just, L. Bowater, S. A. Fairhurst, L. Requena, D. M. Lawson, and S. Bornemann, “Oxalate decarboxylase and oxalate oxidase activities can be interchanged with a specificity switch of up to 282 000 by mutating an active site lid,” *Biochemistry*, vol. 46, no. 43, pp. 12 327–12 336, 2007.

[57] D. J. Vinyard, G. M. Ananyev, and G. Charles Dismukes, “Photosystem ii: the reaction center of oxygenic photosynthesis*,” *Annual review of biochemistry*, vol. 82, pp. 577–606, 2013.

[58] Y. Sheng, E. B. Gralla, M. Schumacher, D. Cascio, D. E. Cabelli, and J. S. Valentine, “Six-coordinate manganese (3+) in catalysis by yeast manganese superoxide dismutase,” *Proceedings of the National Academy of Sciences*, vol. 109, no. 36, pp. 14 314–14 319, 2012.

[59] T. Igarashi, Y. Kono, and K. Tanaka, “Molecular cloning of manganese catalase from lactobacillus plantarum,” *Journal of Biological Chemistry*, vol. 271, no. 47, pp. 29 521–29 524, 1996.

[60] P. Bonnarme and T. W. Jeffries, “Mn (ii) regulation of lignin peroxidases and manganese-dependent peroxidases from lignin-degrading white rot fungi,” *Applied and Environmental Microbiology*, vol. 56, no. 1, pp. 210–217, 1990.

[61] L. A. Reinhardt, D. Svedruzic, C. H. Chang, W. W. Cleland, and N. G. Richards, “Heavy atom isotope effects on the reaction catalyzed by the oxalate decarboxylase from bacillus s ubtilis,” *Journal of the American Chemical Society*, vol. 125, no. 5, pp. 1244–1252, 2003.

[62] W. Imaram, B. T. Saylor, C. P. Centonze, N. G. Richards, and A. Angerhofer, "Epr spin trapping of an oxalate-derived free radical in the oxalate decarboxylase reaction," *Free Radical Biology and Medicine*, vol. 50, no. 8, pp. 1009–1015, 2011.

[63] U. T. Twahir, C. N. Stedwell, C. T. Lee, N. G. Richards, N. C. Polfer, and A. Angerhofer, "Observation of superoxide production during catalysis of bacillus subtilis oxalate decarboxylase at ph 4," *Free Radical Biology and Medicine*, vol. 80, pp. 59–66, 2015.

[64] E.-J. Woo, J. M. Dunwell, P. W. Goodenough, A. C. Marvier, and R. W. Pickersgill, "Germin is a manganese containing homohexamer with oxalate oxidase and superoxide dismutase activities," *Nature Structural & Molecular Biology*, vol. 7, no. 11, pp. 1036–1040, 2000.

[65] P. Cassland, S. Larsson, N.-O. Nilvebrant, and L. J. Jönsson, "Heterologous expression of barley and wheat oxalate oxidase in an e. coli trxb gor double mutant," *Journal of biotechnology*, vol. 109, no. 1, pp. 53–62, 2004.

[66] K. Y. Chee, P. L. Tan, and K. Nadarajah, "Characterisation of the barley oxalate oxidase gene and generation of rice transformant," *Biotechnology*, vol. 11, no. 5, p. 263, 2012.

[67] P. Moussatche, A. Angerhofer, W. Imaram, E. Hoffer, K. Uberto, C. Brooks, C. Bruce, D. Sledge, N. G. Richards, and E. W. Moomaw, "Characterization of ceriporiopsis subvermispora bicupin oxalate oxidase expressed in pichia pastoris," *Archives of biochemistry and biophysics*, vol. 509, no. 1, pp. 100–107, 2011.

[68] E. W. Moomaw, E. Hoffer, P. Moussatche, J. C. Salerno, M. Grant, B. Immelman, R. Uberto, A. Ozarowski, and A. Angerhofer, "Kinetic and spectroscopic studies of bicupin oxalate oxidase and putative active site mutants," *PloS one*, vol. 8, no. 3, 2013.

[69] M. R. Escutia, L. Bowater, A. Edwards, A. R. Bottrill, M. R. Burrell, R. Polanco, R. Vicuna, and S. Bornemann, "Cloning and sequencing of two ceriporiopsis subvermispora bicupin oxalate oxidase allelic isoforms: implications for the reaction specificity of oxalate oxidases and decarboxylases," *Applied and environmental microbiology*, vol. 71, no. 7, pp. 3608–3616, 2005.

[70] O. Opaleye, R.-S. Rose, M. M. Whittaker, E.-J. Woo, J. W. Whittaker, and R. W. Pickersgill, "Structural and spectroscopic studies shed light on the mechanism of oxalate oxidase," *Journal of Biological Chemistry*, vol. 281, no. 10, pp. 6428–6433, 2006.

[71] M. M. Whittaker, H.-Y. Pan, E. T. Yukl, and J. W. Whittaker, "Burst kinetics and redox transformations of the active site manganese ion in oxalate oxidase implications for the catalytic mechanism," *Journal of Biological Chemistry*, vol. 282, no. 10, pp. 7011–7023, 2007.

[72] L. Requena and S. Bornemann, "Barley (hordeum vulgare) oxalate oxidase is a manganese-containing enzyme," *Biochem. J*, vol. 343, pp. 185–190, 1999.

[73] P. Magro, P. Marciano, and P. Di Lenna, “Enzymatic oxalate decarboxylation in isolates of sclerotinia sclerotiorum,” *FEMS microbiology letters*, vol. 49, no. 1, pp. 49–52, 1988.

[74] P. J. Collins, A. D. Dobson, and J. A. Field, “Reduction of the 2, 2-azinobis (3-ethylbenzthiazoline-6-sulfonate) cation radical by physiological organic acids in the absence and presence of manganese,” *Applied and environmental microbiology*, vol. 64, no. 6, pp. 2026–2031, 1998.

[75] G. Hoch and B. Kok, “A mass spectrometer inlet system for sampling gases dissolved in liquid phases,” *Archives of biochemistry and biophysics*, vol. 101, no. 1, pp. 160–170, 1963.

[76] N. Itada and R. E. Forster, “Carbonic anhydrase activity in intact red blood cells measured with 18o exchange.” *Journal of Biological Chemistry*, vol. 252, no. 11, pp. 3881–3890, 1977.

[77] M. E. Moral, C. Tu, N. G. Richards, and D. N. Silverman, “Membrane inlet for mass spectrometric measurement of catalysis by enzymatic decarboxylases,” *Analytical biochemistry*, vol. 418, no. 1, pp. 73–77, 2011.

[78] E. W. Moomaw, R. Uberto, and C. Tu, “Membrane inlet mass spectrometry reveals that ceriporiopsis subvermispora bicupin oxalate oxidase is inhibited by nitric oxide,” *Biochemical and biophysical research communications*, vol. 450, no. 1, pp. 750–754, 2014.

[79] L. K. Keefer, R. W. Nims, K. M. Davies, and D. A. Wink, “nonoates(1-substituted diazen-1-ium-1, 2-diolates) as nitric oxide donors: convenient nitric oxide dosage forms,” *Methods in enzymology*, vol. 268, pp. 281–293, 1996.

[80] W. Cleland, “Use of isotope effects to determine enzyme mechanisms,” *Journal of Labelled Compounds and Radiopharmaceuticals*, vol. 50, no. 11-12, pp. 1006–1015, 2007.

[81] ——, “The use of isotope effects to determine enzyme mechanisms,” *Archives of biochemistry and biophysics*, vol. 433, no. 1, pp. 2–12, 2005.

[82] W. W. Cleland, “The use of isotope effects to determine enzyme mechanisms,” *Journal of Biological Chemistry*, vol. 278, no. 52, pp. 51 975–51 984, 2003.

[83] D. B. Northrop, “Uses of isotope effects in the study of enzymes,” *Methods*, vol. 24, no. 2, pp. 117–124, 2001.

[84] P. F. Cook, *Enzyme mechanism from isotope effects.* Crc Press, 1991.

[85] D. B. Northrop, “The expression of isotope effects on enzyme-catalyzed reactions,” *Annual review of biochemistry*, vol. 50, no. 1, pp. 103–131, 1981.

[86] W. Cleland, “Partition analysis and concept of net rate constants as tools in enzyme kinetics,” *Biochemistry*, vol. 14, no. 14, pp. 3220–3224, 1975.

[87] A. Abragam and B. Bleaney, *Electron paramagnetic resonance of transition ions.* Oxford University Press, 2012.

[88] J. A. Weil and J. R. Bolton, *Electron paramagnetic resonance: elementary theory and practical applications.* John Wiley & Sons, 2007.

[89] S. S. Eaton and G. R. Eaton, *Electron paramagnetic resonance spectroscopy.* Wiley Online Library, 2002.

[90] A. Angerhofer, E. W. Moomaw, I. García-Rubio, A. Ozarowski, J. Krzystek, R. T. Weber, and N. G. Richards, "Multifrequency epr studies on the mn (ii) centers of oxalate decarboxylase," *The Journal of Physical Chemistry B*, vol. 111, no. 19, pp. 5043–5046, 2007.

[91] C. H. Chang, D. Svedružić, A. Ozarowski, L. Walker, G. Yeagle, R. D. Britt, A. Angerhofer, and N. G. Richards, "Epr spectroscopic characterization of the manganese center and a free radical in the oxalate decarboxylase reaction identification of a tyrosyl radical during turnover," *Journal of Biological Chemistry*, vol. 279, no. 51, pp. 52 840–52 849, 2004.

[92] M. R. Burrell, "Insights into reaction specificity and catalysis in bacillus subtilis oxalate decarboxylase," Ph.D. dissertation, University of East Anglia, 2006.

[93] S. Stoll and A. Schweiger, "Easyspin, a comprehensive software package for spectral simulation and analysis in epr," *Journal of Magnetic Resonance*, vol. 178, no. 1, pp. 42–55, 2006.

[94] C. Duboc, D. Ganyushin, K. Sivalingam, M.-N. Collomb, and F. Neese, "Systematic theoretical study of the zero-field splitting in coordination complexes of mn (iii). density functional theory versus multireference wave function approaches," *The Journal of Physical Chemistry A*, vol. 114, no. 39, pp. 10 750–10 758, 2010.

[95] R. L. Shook, W. A. Gunderson, J. Greaves, J. W. Ziller, M. P. Hendrich, and A. Borovik, "A monomeric mniii- peroxo complex derived directly from dioxygen," *Journal of the American Chemical Society*, vol. 130, no. 28, pp. 8888–8889, 2008.

[96] A. K. Whiting, Y. R. Boldt, M. P. Hendrich, L. P. Wackett, and L. Que, "Manganese (ii)-dependent extradiol-cleaving catechol dioxygenase from arthrobacter globiformis cm-2," *Biochemistry*, vol. 35, no. 1, pp. 160–170, 1996.

[97] J. P. Emerson, E. G. Kovaleva, E. R. Farquhar, J. D. Lipscomb, and L. Que, "Swapping metals in fe-and mn-dependent dioxygenases: Evidence for oxygen activation without a change in metal redox state," *Proceedings of the National Academy of Sciences*, vol. 105, no. 21, pp. 7347–7352, 2008.

[98] M. Srnec, F. Aquilante, U. Ryde, and L. Rulisek, "Reaction mechanism of manganese superoxide dismutase studied by combined quantum and molecular mechanical calculations and multiconfigurational methods," *The Journal of Physical Chemistry B*, vol. 113, no. 17, pp. 6074–6086, 2009.

[99] P. Campomanes, W. F. Kellett, L. M. Easthon, A. Ozarowski, K. N. Allen, A. Angerhofer, U. Rothlisberger, and N. G. Richards, "Assigning the epr fine structure parameters of the mn (ii) centers in bacillus subtilis oxalate decarboxylase by site-directed mutagenesis and dft/mm calculations," *Journal of the American Chemical Society*, vol. 136, no. 6, pp. 2313–2323, 2014.

[100] M. M. Bradford, "A rapid and sensitive method for the quantitation of microgram quantities of protein utilizing the principle of protein-dye binding," *Analytical biochemistry*, vol. 72, no. 1, pp. 248–254, 1976.

[101] W. H. Koppenol, P. L. Bounds, T. Nauser, R. Kissner, and H. Rüegger, "Peroxynitrous acid: controversy and consensus surrounding an enigmatic oxidant," *Dalton Transactions*, vol. 41, no. 45, pp. 13 779–13 787, 2012.

[102] S. Pou, C. L. Ramos, T. Gladwell, E. Renks, M. Centra, D. Young, M. S. Cohen, and G. M. Rosen, "A kinetic approach to the selection of a sensitive spin trapping system for the detection of hydroxyl radical," *Analytical biochemistry*, vol. 217, no. 1, pp. 76–83, 1994.

[103] P. Stephens, "Magnetic circular dichroism," *Annual Review of Physical Chemistry*, vol. 25, no. 1, pp. 201–232, 1974.

[104] U. Das, G. Hariprasad, A. S. Ethayathulla, P. Manral, T. K. Das, S. Pasha, A. Mann, M. Ganguli, A. K. Verma, R. Bhat *et al.*, "Inhibition of protein aggregation: supramolecular assemblies of arginine hold the key," *PloS one*, vol. 2, no. 11, pp. No–PP, 2007.

APPENDIX

```
P15290 GER2_WHEAT        1    ------------------------------------------------------------    0
O34714 OXDC_BACSU        1    ------------------------------------------------------------    0
P45850 OXO1_HORVU        1    ------------------------------------------------------------    0
A8FB72 A8FB72_BACP2      1    ------------------------------------------------------------    0
Q5WJS8 Q5WJS8_BACSK      1    ------------------------------------------------------------    0
Q65EW1 Q65EW1_BACLD      1    ------------------------------------------------------------    0
M2QJL8 M2QJL8_CERS8      1    MNEKILSAFCVILFSLSVAARPTENGP----QIVIANNAGTYLPVLRGSGTKSSSAADAT   56
M2QDP8 M2QDP8_CERS8      1    MNEKLVSVFCAILVAISVSARPTGNDVFYLPRAVAVSSAGASSPASLSSGTESSSAAEPT   60


P15290 GER2_WHEAT        1    ------------------------------------------------------------    0
O34714 OXDC_BACSU        1    -----------------MKKQNDIPQPIRGDK-GATVKIPRNIERDRQNPDMLVPPETDH   42
P45850 OXO1_HORVU        1    ------------------------------------------------------------    0
A8FB72 A8FB72_BACP2      1    ----------------MSEKQNGVPQPIRGEK-GATVKIPRNLERDRQNPDMLTPPETDH   43
Q5WJS8 Q5WJS8_BACSK      1    ----MKR-GDN---VKPLKGNPNIPQPIRADGAGGVDRGPRNLMRDLQNPNILVPPETDR   52
Q65EW1 Q65EW1_BACLD      1    -----------------MEKNKQIPQPIRGEK-GAETKIPHNVERDRQNPDMLVPPETDH   42
M2QJL8 M2QJL8_CERS8      57   QTVPFASDDPNPRLWDIDTKNLTKVTPERGQL-GAKILGPDNLPIDLQNADTLAPPTTDS  115
M2QDP8 M2QDP8_CERS8      61   ETVPFASDDPNPRLWNIDTQDLSVVAPERGPL-GAKIIGPDNLPLDIQNADTLAPPTTDS  119


P15290 GER2_WHEAT        1    ------------------------------------------------------------    0
O34714 OXDC_BACSU        43   GTVSNMKFSFSDTHNRLEKGGYAREVTVRELPISENLASVNMRLKPGAIRELHWHKEAEW  102
P45850 OXO1_HORVU        1    ------------------------------------------------------------    0
A8FB72 A8FB72_BACP2      44   GTVPNMKYSFSDTHNRLEKGGYAREVTVRELPISKSLASVNMRLKPGAIRELHWHKEAEW  103
Q5WJS8 Q5WJS8_BACSK      53   GLIPNLRFSFSDAHMQLNHGGWSREITQRDLPIATTLAGVNMSLTPGGVRELHWHKQAEW  112
Q65EW1 Q65EW1_BACLD      43   GTVPNMKFSFSDVHNRLEKGGYAREVTVRELPISDKLASVNMRLKPGAIRELHWHKEAEW  102
M2QJL8 M2QJL8_CERS8      116  GSIPNPKWPFALSHNTLYSGGWVRIQNDEVMPIAKAMAGVNMRLEAGAIRELHWHNTPEW  175
M2QDP8 M2QDP8_CERS8      120  GSIPNAKWPFALSHNTLYTGGWVRIQNNEVLPIAKAMAGVNMRLEAGTIRELHWHNTPEW  179


P15290 GER2_WHEAT        1    ------------------------------------------------------------    0
O34714 OXDC_BACSU        103  AYMIYGSARVTIVDEKGRSFIDDVGEGDLWYFPSGLPHSIQAL---EEGAEFLLVFDDGS  159
P45850 OXO1_HORVU        1    ------------------------------------------------------------    0
A8FB72 A8FB72_BACP2      104  AYMIYGEARITSVDAEGRNFTEDVTEGDLWYFPSGLPHSIQAL---EPGAEFLLVFDDGS  160
Q5WJS8 Q5WJS8_BACSK      113  SYMLLGHARITAVDQNGRNFIADVGPGDLWYFPPGIPHSIQGL---DDGCEFLLVFDDGM  169
Q65EW1 Q65EW1_BACLD      103  AYMLYGKARITSVDQDGRNFIEDVKEGDLWYFPSGLPHSIQAL---EDGCEFLLVFDDGS  159
M2QJL8 M2QJL8_CERS8      176  AYILKGTTQITAVDQNGRNYLANVGPGDLWYFPEGMPHSLQGTDANNEGSEFLLIFPDGT  235
M2QDP8 M2QDP8_CERS8      180  AYILKGTTQITAVDENGKNYLANVGPGDLWYFPEGMPHSLQGTNASDEGSEFLLIFPDGT  239


P15290 GER2_WHEAT        1    -------------MGYSKTLVAGLFAMLLLAPAVL---------ATDPDPLQDFCVADLD   38
O34714 OXDC_BACSU        160  FSENSTFQLTDWLAHTPKEVIAANFGVTKEEISNLPGKEKYIFENQLPGSLKDDIVEGPN  219
P45850 OXO1_HORVU        1    ---------------------------------------------SDPDPLQDFCVADLD   15
A8FB72 A8FB72_BACP2      161  FSENSTFQVTDWLAHTPEEVVLQNFGMTKEQFEKLPEKEKYIFQKGIPGSLECDKVKTGQ  220
Q5WJS8 Q5WJS8_BACSK      170  FSDLSTLSLSDWMAHTPKDVLSANFGVPESVFATIPTEQVYIYQDEVPGPLQSQQINSPY  229
Q65EW1 Q65EW1_BACLD      160  FSENSTFQVTDWLAHTPDEVIAANFGISKDVVASLPVEEKYIFQEAIPGCLEKDKVESPN  219
M2QJL8 M2QJL8_CERS8      236  FDSSNQFMITDWLAHTPKDVIAKNFGVDISEFDRLPSHDLYIFPGVA-PPLDAKAPEDPQ  294
M2QDP8 M2QDP8_CERS8      240  FDASNQFMITDWLAHTPKDVIAKNFGVDISEFDRLPSHDLYIFPGVA-PPLDATAPEDPQ  298
                                                                                *.

P15290 GER2_WHEAT        39   GKAVSVNGHTCKPMSEAGDDFLFSSKLAKAGNTSTPNGSAVTELDVAEWPGTNTLGVSMN   98
O34714 OXDC_BACSU        220  G--------------E--VPYPFTYRLLEQEPIES-EGGKVYIADSTNFKVSKTIA--SA  260
P45850 OXO1_HORVU        16   GKAVSVNGHTCKPMSEAGDDFLFSSKLTKAGNTSTPNGSAVTELDVAEWPGTNTLGVSMN   75
A8FB72 A8FB72_BACP2      221  G--------------E--VPNSFKYELLKQEPITS-SGGQVWIADSTNFKASKTIA--SA  261
Q5WJS8 Q5WJS8_BACSK      230  G--------------A--VPQTFKHELLKQPPLVT-PGGSVRIVDSRNFPVSKTIA--AA  270
Q65EW1 Q65EW1_BACLD      220  G--------------T--VPLSFSYNLLEQEPIIS-IGGKVWIADSTNFKASKTIA--SA  260
M2QJL8 M2QJL8_CERS8      295  G--------------T--IPLPYSFEFSKVKPTQY-AGGTVKIADTRTFPIAKTIS--VA  335
M2QDP8 M2QDP8_CERS8      299  G--------------T--IPLPYSFEFSKVVPTQY-AGGTVKIADTRTFPISKTIS--VA  339
                              *                     :. .: :        *. *   *   :  ::*:.

P15290 GER2_WHEAT        99   RVDFAPGGTNPPHIHPRATEIGIVMKGELLVGILGSLDSGNKLYSRVVRAGETFLIPRGL  158
O34714 OXDC_BACSU        261  LVTVEPGAMRELHWHPNTHEWQYYISGKARMTVFASDGHA---RTFNYQAGDVGYVPFAM  317
P45850 OXO1_HORVU        76   RVDFAPGGTNPPHIHPRATEIGMVMKGELLVGILGSLDSGNKLYSRVVRAGETFVIPRGL  135
A8FB72 A8FB72_BACP2      262  LVKVDPGAIRELHWHPNTDEWQYFISGKARMTVFASDGHA---RTFNYQAGDVGYVPFAM  318
Q5WJS8 Q5WJS8_BACSK      271  LVEVEPGAMREMHWHPNNDEWQYYLTGQARMTVFTGNGVA---RTFDYRAGDVGYVPFAT  327
Q65EW1 Q65EW1_BACLD      261  LVEVEPGGIRELHWHPNTDEWQYYISGQAKMTVFAADGHA---RTFNYQAGDVGYVPFAM  317
M2QJL8 M2QJL8_CERS8      336  EVTVEPGAMRELHWHPTEDEWTFFIEGQARVTIFAGQSNA---QTYDYQGGDIAYIPTAW  392
M2QDP8 M2QDP8_CERS8      340  EITVEPGAMRELHWHPTEDEWTFFIEGQARVTLFAGESNA---QTYDYQGGDIAYIPTAY  396
                               : . **. .  * **   *    : *:  : :: .   .    :   :.*:   :* .

P15290 GER2_WHEAT        159  MHFQFNVGKTEASMVVSFNSQNPGIVFVPLTLFGSNPPIPTPVLTKALRVEARVVELLKS  218
O34714 OXDC_BACSU        318  GHYVENIGDEPLVFLEIFKDDHYADVS--LNQW--LAMLPETFVQAHLDLGKDFTDVLSK  373
P45850 OXO1_HORVU        136  MHFQFNVGKTEAYMVVSFNSQNPGIVFVPLTLFGSDPPIPTPVLTKALRVEAGVVELLKS  195

A8FB72 A8FB72_BACP2      319  GHYVENTGDEPLYFLEIFKSDHYADIS--LNQW--LAVTPKQLILDHLDQGEEFLKLLDT  374
Q5WJS8 Q5WJS8_BACSK      328  GHYIQNTGNESVWFLEMFKSDRFEDVS--LNQW--LALTPTELVQHNIHVDSKFTNKLRK  383
Q65EW1 Q65EW1_BACLD      318  GHYVQNTGDEPLRFLEIFKDDHYADVS--LNQW--LALVPEELVRQHLDVGSEFTKMLSK  373
M2QJL8 M2QJL8_CERS8      393  GHYVENSGNTTLRFLEIFNSPLFEDVS--LAQW--IANTPPAIVKATLQLSDEVINTLNK  448
M2QDP8 M2QDP8_CERS8      397  GHYVENSGNTTLRFLEIFNSPLFQDVS--LTQW--LANTPRAIVKATLQLSDNVIDSLNK  452
                               *:  * *.    ::  *:.     :   *  :      *  .:   :     . . * .

P15290 GER2_WHEAT        219  KFAA--GF-----                                                224
O34714 OXDC_BACSU        374  EKHPVVKKKCSK-                                                385
P45850 OXO1_HORVU        196  KFAG--GS-----                                                201
A8FB72 A8FB72_BACP2      375  EKHPVIAAPKKED                                                387
Q5WJS8 Q5WJS8_BACSK      384  EKWPVVKYPTI--                                                394
Q65EW1 Q65EW1_BACLD      374  EKHPVVKFDKK--                                                384
M2QJL8 M2QJL8_CERS8      449  SKAFVVG------                                                455
M2QDP8 M2QDP8_CERS8      453  SKAFVVASD----                                                461
```

VITA

VITA

Wen Zhu was born in Shanxi, China. She then moved with her parents to Dalian, Liaoning. She earned her Bachelors degree in Chemistry from Southwest University (SWU), Chongqing. While in SWU, she was award National Scholarship and Outstanding Student Leadership of Chongqing. She entered the doctoral program of chemistry at the University of Florida and worked as a Teaching and Research Assistant in the Department of Chemistry. After two years study in Florida, she transfered to Purdue University at 2012 to follow her graduate advisor who had accepted the position as the Chair of the Department of Chemistry and Chemical Biology at Indiana University-Purdue University Indianapolis. Currently, she is in the Student Development Funding Committee of IUPUI, and also works as a volunteer in the Indianapolis Zoo.